Alternative Electrochemical Salt Waste Forms, Summary of FY/CY2011 Results

Fuel Cycle Research & Development

Prepared for
U.S. Department of Energy
B.J. Riley, J.S. McCloy, J.V. Crum,
C.P. Rodriguez, C.F. Windisch Jr.,
W.C. Lepry, J. Matyas,
M.P. Westman, B.T. Rieck, J.B. Lang,
and D.A. Pierce
Pacific Northwest National Laboratory

December 30, 2011
FCRD-SWF-2012-000028
PNNL-21016

SUMMARY

The Fuel Cycle Research and Development Program, sponsored by the U.S. Department of Energy Office of Nuclear Energy, is currently investigating alternative waste forms for wastes generated from the reprocessing of nuclear fuel. One such waste results from an electrochemical separations process, called the "Echem" process, in molten KCl-LiCl salt as a spent salt containing alkali, alkaline earth, lanthanide halides and a small quantities of actinide halides where the primary anion is chloride with small quantities of iodide. Pacific Northwest National Laboratory (PNNL) is investigating two candidate waste forms for the Echem spent-salt, high-halide minerals (i.e., sodalite and cancrinite) and tellurite (TeO_2)-based glasses. Both of these candidates showed promise in FY2009 and FY2010 with a simplified nonradioactive simulant of the Echem waste. Further testing was performed on these waste forms in the fiscal (FY) and calendar (CY) year of 2011 to investigate the possibility of their use in a sustainable fuel cycle. This report summarizes the results of FY/CY2011 efforts.

The chemical durability results for the tellurite glasses in FY2010 revealed a wide variety of waste form performance in these materials. The most promising glass studied was a lead-tellurite glass formulation with the Echem salt simulant. This glass showed very good chemical durability with a normalized release for sodium of 0.478 g/m^2 following a seven-day leaching test. With this in mind, the following studies were undertaken in FY/CY2011 to further investigate and optimize this type of glass as a potential waste form:

1) *Expanded study on lead-tellurite glasses*. The lead-tellurite glass system was further investigated in FY/CY2011 to determine the waste-loading limits and assess the tellurium-oxygen bonding structure as a function of waste loading with Raman spectroscopy and X-ray diffraction. Te-O bonding in tellurite glasses is quite complex; at least eight different structures have been presented in the literature and typically include α-TeO_4, β-TeO_4, TeO_{3+1}, and TeO_3 structures (the α/β notation denotes the way that the TeO_4 species bond to one another, and the number after the "O" denotes the number of oxygens bonded to the central Te atom in that species). We also investigated some of the other waste-form related properties of the lead-tellurite glasses, such as the thermal diffusivity, glass transition temperature, crystallization temperature, melting temperature, and mass loss as a function of temperature. The structural investigation revealed that the medium-range order in the glass decreased and the tellurite network was depolymerized as the waste fraction was increased. It was apparent that glass-network breaking was predominantly caused by the additions of the waste cations and that the presence of chloride may have actually caused some repolymerization of the network by scavenging alkali and preventing it from acting as a network modifier. At the highest waste loadings, the glass became phase-separated, resulting in a Te-rich phase and a Pb-alkali-chloride-rich phase, and some chloride-containing crystals were formed.

2) *Investigated the glass network structure of P-series glasses from FY2010 with Raman spectroscopy ("P" here does not denote phosphorus)*. Here, we studied the glass structure of the P-series glasses (TeO_2 with various other oxide additions such as ZnO, PbO, P_2O_5, Al_2O_3, B_2O_3, and WO_3); the study provided a preliminary understanding of the various Te-O structural configurations in the literature and how to identify them with Raman spectroscopy. The goal was to attempt to correlate a particular Te-O structure with a glass that had high chemical durability and reverse-engineer a glass with very high chemical durability by targeting the preferred structure with changes in composition. This has proved unsuccessful on a large scale, but we did observe some unique frequency bands in the Raman spectra for the lead-tellurite glasses that might be a first step toward better understanding the link between the glass structure and the chemical durability.

3) *Investigated the structural effects of various components in the tellurite glasses*. For this study, we used Raman spectroscopy to look at the structure of simplified glasses in which various components had been removed and added to provide different combinations of the anions and

cations. This study provided some very useful information regarding the effects of Cl and alkali on the tellurite glass network.

4) *Investigated tellurite crystals as a surrogate for tellurite glass*. We found a previous study where a large set of tellurite crystals were fabricated and the Te-O structures determined with nuclear magnetic resonance (NMR). Single-phase tellurite crystals have a single type of tellurium-oxygen structure, in contrast with tellurite glasses that have a mixed set of most of the different types of structures. The goal was to make a series of tellurite crystals from each category and assess the chemical durability of each. In FY2011, we made a series of crystals, some of which were highly phase-pure (>95%). We intend to verify their structure (with NMR and/or Raman spectroscopy) and perform chemical durability tests on them to look for a correlation between the structure and the chemical durability.

For the second candidate waste form, the solution-derived sodalite, we looked at optimizing a few of the variables in the process. These variables included the following:

1) *Investigated alternative silica sources*. We fabricated sodalites with an organic source of silica, tetraethyl orthosilicate (TEOS), in place of the colloidal silica. The goal with this substitution was to assess the differences in reaction rates for sodalite formation among the silica sources as well as the differences in sodalite concentration. The change in silica sources resulted in a noticeable improvement from 23.8 mass% sodalite in the S5A specimen with colloidal silica to 95.7 mass% sodalite in the S5C specimen with TEOS.

2) *Investigated alternative 4-coordinated network formers*. We performed the solution-based process with an organic species of Ge^{4+}, germanium (IV) ethoxide, in place of the TEOS to see whether we could fabricate a germanium-based sodalite. The germanium sodalite was targeted because it would provide the following: a reduced firing temperature, an increased sodalite concentration because of the reduced chloride volatility (due to lower firing temperature), and an increased fired-pellet density, which would improve volumetric waste loading. The high porosity in the initially fired pellets was a deterrent to pursuing this route any further, though we did demonstrate a high germania-based sodalite concentration (82 mass%) in the as-made gel. These results plus the cost of germanium (IV) ethoxide led us to abandon this pursuit.

3) *Investigated alternative sintering aids*. We fabricated a series of six alternative sintering aids (glass binders) with different viscosities in order to attempt to consolidate the solution-derived powders at a lower temperature, retaining the sodalite structure and preventing chloride volatility. These sintering aids included four sodium borosilicate formulations, a sodium aluminophosphate formulation, and a lead-tellurite glass formulation (TPb_0). Each of these glasses was added to a separate batch, as a powder; the gel was dried, specimens from the batches were pressed into pellets, fired at different temperatures, and the phases quantified. The sodium borosilicate glasses dramatically improve the densification, (up to 96% of theoretical density for sodalite), of the fired pellets at much-reduced temperatures of ~750°C, where rather large amounts of sodalite were still produced (70.6 mass%). We will continue to improve the process in CY2012.

CONTENTS

FIGURES

TABLES

ABBREVIATIONS

α	thermal diffusivity
δ_{iso}	isotropic chemical shift
$\tilde{\nu}$	wavenumbers (cm^{-1}), shift frequency for Raman spectroscopy
ρ_B	density of the bulk material (e.g., glass)
ρ_{salt}	density of the salt waste
ρ_S	storage density
ASTM	American Society for Testing and Materials, now ASTM International, Inc.
Cat.	cation
CS	colloidal silica
CY	calendar year
DOE	U.S. Department of Energy
DSC	differential scanning calorimetry
DTA	differential thermal analysis
Echem	electrochemical separations process
EDS	energy dispersive spectroscopy
FP	fission products
FTIR	Fourier transform infrared spectroscopy
FY	fiscal year
Ge-EtO	germanium(IV) ethoxide, $Ge(OC_2H_5)_4$
HFE	high-frequency envelope
HT	heat-treatment
ICSD	International Crystal Structure Database
K_{gl}	glass formation constant
LFE	low-frequency envelope
Ln	lanthanides (or rare-earths)
m	mass ratio
M	mole ratio
M	metal
N/A	not applicable
NBO	non-bridging oxygen
NBS	sodium borosilicate
NL_i	normalized release of element i (from the PCT) in g/m^2
NMR	nuclear magnetic resonance
PCT	Product Consistency Test
PDF	Powder Diffraction File

PNNL	Pacific Northwest National Laboratory
QU	quenched
RDF	radial distribution function
RT	room temperature
SA	sintering aid
SEM	scanning electron microscope, scanning electron microscopy
SG	space group
tbp	trigonal bypyramidal (TeO_4)
T_c	crystallization temperature
T_g	glass transition temperature
T_L	liquidus temperature
T_M	melting temperature
TEOS	tetraethyl orthosilicate, $Si(OC_2H_5)_4$
tp	trigonal pyramidal (TeO_3)
$TPb_{\#}$	lead tellurite glass where "#" denotes the mass% of added XCl_{20}
T_x	temperature of the crystallization onset
XCl_{20}	mixed chloride electrochemical waste stream with 20% FP
XCl_y	alternative form of XCl_{20} (see Appendix A)
XRD	X-ray diffraction, X-ray diffractometer

1 INTRODUCTION

An increased reliance on nuclear power is a likely solution to meet the clean-energy demands of the future (Vienna, 2010). The U.S. Department of Energy's (DOE's) Office of Nuclear Energy Fuel Cycle Research and Development (FCRD) Program is currently in the process of identifying the most efficient pathway for nuclear power production, which will likely involve a series of steps in which the fuel will be reprocessed and the reusable fuel recycled to recover fuel value. The waste from reprocessing will be immobilized in one of several different waste forms. A brief overview of the various types of proposed reprocessing steps and waste streams is presented in our previous work (Riley et al., 2010). One of the separations methods being considered is an electrochemical process. In this method, the fuel is dissolved in molten ionic salts or a LiCl-KCl eutectic, and the resulting "spent salt" will need to be immobilized in a viable waste form. This spent salt is commonly referred to the "Echem salt" and consists primarily of an alkali chloride salt with minor amounts of alkaline earth, transition metal, lanthanide, and actinide chlorides plus a very small fraction of iodide.

The currently assumed waste form for immobilizing this salt waste is a glass-bonded sodalite, nominally $Na_4Al_3(SiO_4)_3Cl$ (Ebert, 2005; Bateman et al., 2007). This baseline waste form is fabricated by mixing zeolite 4A with the salt waste. The salt is occluded in the zeolite at about 500ºC; then the salt containing zeolite is mixed with borosilicate glass in a 3:1 mass ratio. The mixture is transferred to a mold and consolidated at ~915°C with only slight pressure (a steel plate resting on top). The loading of waste in the zeolite is given by the target reaction:

$$Na_{12}(AlSiO_4)_{12} + 4\ NaCl \rightarrow 2\ Na_8(AlSiO_4)_6Cl_2 \quad (1)$$

(zeolite 4A) (halite) (sodalite)

After the 3:1 blending with borosilicate glass, the loading of fission-product-loaded salt in the final waste form is roughly 7.5 mass%.

The FCRD program has been supporting the development of alternative waste forms for the Echem salt waste since 2009. Part of that work has been at Pacific Northwest National Laboratory (PNNL), where we are developing a rare type of glass called a tellurite glass and high-halide minerals made with a solution-based process (Crum et al., 2009; Riley et al., 2010).

Tellurite glass has many attractive properties for a waste form, including high halide solubility over a wide range of different and mixed halides, high density (improving volumetric waste loading capacity), and good glass formation with chlorides and many other additives (Yakhkind and Chebotarev, 1980; Vogel et al., 1974). One of the primary drawbacks with these glasses is that they cost more to make than a traditional borosilicate-based glass waste form. Another drawback to these glasses is that since they have not previously been developed for waste form applications, many of the relevant engineering properties are unknown. In our earlier work, we discussed scoping tests for candidate waste form selection and the evaluation of a series of different tellurite glass systems for chemical durability, solubility of the salt waste, and glass properties (Riley et al., 2010). A few of the formulations showed good chemical durability and high waste loading capacity. The work presented here is a continuation of that work along with some additional fabrication and characterization data.

The primary high-halide mineral that we have worked with is sodalite. When the sintering aid (glass binder) was added to the sodalite during the solution-based process, even specimens with small additions, i.e., 2–5 mass%, showed a marked decreases in the porosity of the waste form after it was pressed into pellets and sintered. The sodalite structure was identified as one of the naturally occurring structures that contain the waste components, i.e., alkalis and halides. These minerals have been under research for the past several years for incorporating the Echem salt components for the baseline waste form (Ebert, 2005; Bateman et al., 2007). However, we identified the solution-based process as a potential improvement to the preparation of the sodalites. The liquid-synthesis method was identified because it allows for a near-room temperature aqueous processing route, reducing energy costs. It also allows for complete containment of the waste in a solution versus processing the salt as a powder that can become airborne.

The sodalite powders that were formed upon drying were small (~1–5 μm) and thus needed to be sintered together to form a viable waste form. However, this firing process only yielded pellets that were ~70% dense compared to the theoretical density of sodalite, 2.27×10^3 kg/m^3. Therefore, a sintering aid was added to further densify the pellets. Even small additions (2 mass%) of a high-viscosity glass, NBS-1, dramatically increased the density of the pellets to >90% of theoretical density (Vienna et al., 1998).

In FY2010, we assessed the chemical durability of these different waste forms with the Product Consistency Test (PCT) and some of the waste forms we made for each family of materials showed promise (*Standard Test Methods for Determining Chemical Durability of Nuclear, Hazardous, and Mixed Waste Glasses and Multiphase Glass Ceramics: The Product Consistency Test (PCT)* ASTM C 1285-08, 2002). Since both of these waste forms showed good performance in the PCT, they were both candidates for further consideration.

The chemical durability results for the tellurite glasses in FY2010 revealed a wide variety of waste form performance in these materials. The most promising glass studied was a lead-tellurite glass with the Echem salt simulant. This glass showed very good chemical durability: the normalized release for sodium was 0.478 g/m^2 and comparable to borosilicate glasses (Ebert and Wolf, 1999). With this in mind, the following studies were undertaken in FY/CY2011 to further investigate and optimize these glasses as a potential waste form:

1) *Expanded study on lead-tellurite glasses*. The lead-tellurite glass system was further investigated in FY/CY2011 to determine the waste-loading limits and assess the tellurium-oxygen bonding structure as a function of waste loading with Raman spectroscopy and X-ray diffraction. Te-O bonding in tellurite glasses is quite complex; at least eight different structures have been presented in the literature and typically include α-TeO_4 (or α-TeO_2), β-TeO_4 (or β-TeO_2), TeO_{3+1}, and TeO_3 structures (the α/β notation denotes the way that the TeO_4 species bond to one another, and the number after the "O" denotes the number of oxygens bonded to the central Te atom in that species). We also investigated some of the other waste-form related properties of the lead-tellurite glasses such as the thermal diffusivity, glass transition temperature, crystallization temperature, melting temperature, and mass loss as a function of temperature. The structural investigation revealed that the medium-range order in the glass decreased and the tellurite network was depolymerized as the waste fraction was increased. It was apparent that glass-network breaking was predominantly caused by the additions of the waste cations and that the presence of chloride may have actually caused some repolymerization of the network by scavenging alkali and preventing it from acting as a network modifier. At the highest waste loadings the glass became phase-separated, resulting in a Te-rich phase and a Pb-alkali-chloride-rich phase, and some chloride-containing crystals are formed.

2) *Investigated the glass network structure of P-series glasses from FY2010 with Raman spectroscopy*. Our study of the glass structure of the P-series glasses provided a preliminary understanding of the various Te-O structural configurations in the literature and how to identify them with Raman spectroscopy. The goal was to correlate a particular Te-O structure with a glass possessing high chemical durability and reverse-engineer a glass with very high chemical durability by targeting the preferred structure with changes in composition. This has proved unsuccessful on a large scale but we did observe some unique frequency bands in the Raman spectra for the lead-tellurite glasses that might be a first step toward better understanding the link between the glass structure and the chemical durability.

3) *Investigated the structural effects of various components in the tellurite glasses*. For this study, we looked at the structure of simplified glasses with Raman spectroscopy in which various components were removed and added to provide different combinations of the anions and cations. This study provided some very useful information.

4) *Investigated tellurite crystals as a surrogate for tellurite glass*. In addition to the tellurite glasses, we also looked at some tellurite crystals. The goal of this study was to look at the chemical durability of tellurite compounds that contained only one structural configuration of Te-O. This idea was proposed based on results presented by Sakida et al. (Sakida et al., 1999a). Sakida et al. prepared 21 tellurite

crystals, characterized them with ^{125}Te nuclear magnetic resonance (NMR), and then categorized them based on the structural configuration of the Te present in the crystals (see Figure 1.1). Each of these crystals fell into a particular category defined as TeO_3, TeO_{3+1}, or TeO_4, where TeO_4 structural units were divided into α-TeO_4 and β-TeO_4. Single-phase tellurite crystals have a single type of tellurium-oxygen structure in contrast with tellurite glasses that have a mixed set of most of the different types of structures. The goal was to make a series of tellurite crystals from each category and assess the chemical durability of each. In FY2011, we made a series of crystals, some of which were highly phase pure (>95%). We intend to verify their structure (with NMR and/or Raman spectroscopy) and perform chemical durability tests on them to look for a correlation between the structure and the chemical durability. We wanted to achieve melting so that the chunks could be ground and sieved and a particular size fraction could be retained for chemical durability tests. We had difficulty melting all of the mixtures that we attempted.

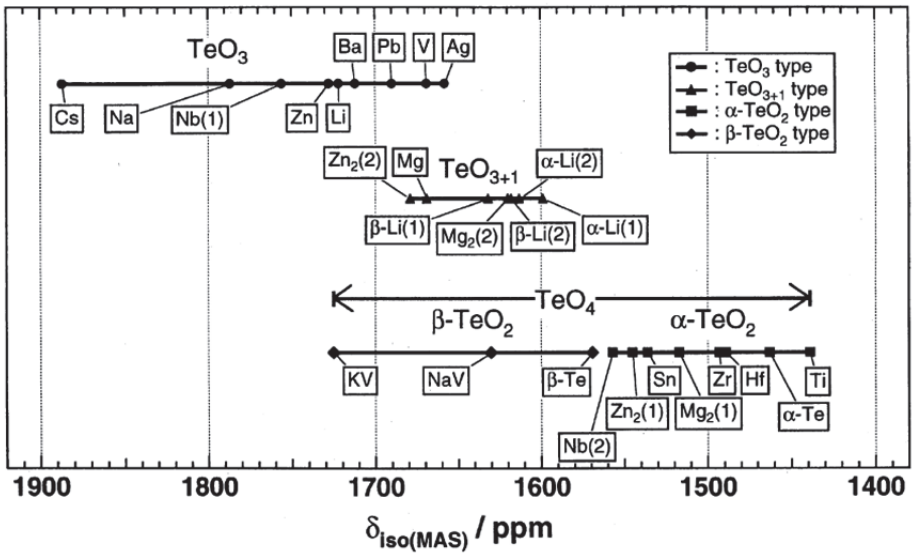

Figure 1.1. Ranges of isotropic chemical shifts (δ_{iso}) for tellurium sites with different structural units determined with ^{125}Te magic angle spinning (MAS) NMR at 9.4 T (Sakida et al., 1999a).

For the second candidate waste form, the high-halide minerals, we looked at optimizing a few of the variables in the solution-based process as well as some post-process adjustments to the heat-treatments. These variable studies included the following:

1) *Investigated alternative silica sources*. We fabricated solution-derived sodalites with an organic source of silica, tetraethyl orthosilicate (TEOS), in place of the colloidal silica (CS) (see Figure 1.2a). The goal of this substitution was to assess the differences in reaction rate for sodalite formation between the silica sources as well as the differences in sodalite concentration. The change in silica sources resulted in a noticeable improvement, from 23.8 mass% sodalite in the S5A sample with CS to 95.7 mass% sodalite in the S5C sample with TEOS.

2) *Investigated alternative 4-coordinated network formers*. We performed a solution-based process with an organic species of Ge^{4+}, germanium (IV) ethoxide, in place of the TEOS to see whether we could fabricate a germanium-based sodalite (see Figure 1.2b). The germanium sodalite was targeted because it would provide the following: a reduced firing temperature, an increased sodalite concentration because of the reduced chloride volatility (due to lower firing temperature), and an increased fired-pellet density, improving volumetric waste loading. The high porosity in the initially fired pellets was a deterrent to pursuing this route any further, though we did demonstrate a high germania-based sodalite concentration (82 mass%) in the as-made gel. These results plus the cost of germanium (IV) ethoxide, led us to abandon this pursuit.

3) *Investigated alternative sintering aids*. We had success in FY2010 with the NBS-1 glass, but due to the high viscosity of this glass, the temperatures required for pellet densification were rather high (850°C) and that led to chloride volatility, evidenced by a decrease in the sodalite concentration (Vienna et al., 1998). In FY/CY2011, we fabricated a series of six alternative sintering aids with different viscosities in order to attempt to consolidate the powders at a lower temperature, retaining the sodalite structure and preventing chloride volatility. These sintering aids included four sodium borosilicate formulations, a sodium aluminophosphate formulation, and a lead-tellurite glass formulation (TPb_0). Each of these glasses was added to a separate batch as a powder; the gel was dried, specimens from the batch were pressed into pellets, fired at different temperatures, and the phases quantified. The sodium borosilicate glasses dramatically improved the densification, (up to 96% of theoretical density for sodalite), of the fired pellets at much-reduced temperatures of ~750°C, where rather large amounts of sodalite were still produced (70.6 mass%). We will continue to improve the process in CY2012.

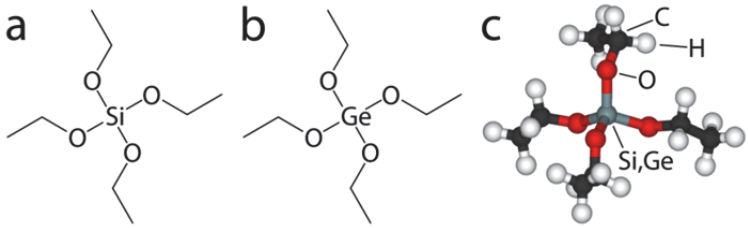

Figure 1.2. (a) Hydrocarbon stick figure of TEOS, (b) hydrocarbon stick figure of germanium(IV) ethoxide, and (c) a three-dimensional view of these structures. *Note: for (a) and (b), the atom located at each bend and terminal is a C atom where each C has four total bonds achieved with hydrogen atoms in areas where oxygen is not present.*

2 EXPANDED BACKGROUND AND APPROACH

The simulated (nonradioactive) waste composition used in this study is the 20 mass% fission-products (FP) waste stream (Yoo, 2009) as presented in Table 2.1. The 20 mass% FP Echem waste stream is designated in this report as $X\text{Cl}_{20}$ and was discussed in more detail in our previous publications (Crum et al., 2009; Riley et al., 2010).

Table 2.1. Calculated composition of spent electrochemical salt with 20 mass% FP ($X\text{Cl}_{20}$) (Yoo, 2009).

Element	Mole Fraction	Mass Fraction
Y	0.0007	0.0020
La	0.0029	0.0127
Ce	0.0045	0.0195
Pr	0.0022	0.0095
Nd	0.0067	0.0301
Pm	0.0003	0.0011
Sm	0.0020	0.0092
Eu	0.0002	0.0011
Gd	0.0002	0.0011
Tb	0.0000	0.0001
Li	0.2219	0.0477
K	0.1603	0.1942
Na	0.0630	0.0449
Rb	0.0006	0.0017
Cs	0.0081	0.0332
Sr	0.0013	0.0036
Ba	0.0030	0.0129
Cl	0.5212	0.5725
Total	1.0000	1.0000
Simplified	**Mole Fraction**	**Mass fraction**
Alkali	0.4539	0.3217
Alkaline Earth	0.0044	0.0166
Lanthanide	0.0198	0.0863
Halide	0.5219	0.5754

2.1 High-Halide Minerals: Background

It is not as easy to incorporate radionuclides into a ceramic waste form as it is to incorporate them into a glass—a very forgiving host network. The incorporation of waste radionuclides in a ceramic waste form is limited to two options, in which (1) a radionuclide is actually incorporated into the structure of the ceramic material at a specific atomic position in the periodic structure or (2) a radionuclide is captured by the non-radioactive phase (Ewing et al., 1995). In order for option (1) to be possible, the radionuclide properties must be suitable for incorporation into the ceramic crystal structure imposed by the coordination polyhedra, which include specific size, charge, and bonding constraints. Clearly, the requirements on a target ceramic waste would have to include the ability to accommodate a variety of atomic substitutions of varying sizes and charges to allow for charge balance in the structure. Considering option (2), a common approach has been to immobilize individual grains of radioactive phases in a ceramic phase such as TiO_2 or Al_2O_3 that have high chemical durability.

To start this study, a literature survey was conducted to identify naturally occurring minerals that are high in halides and/or alkali oxides (see Table 2.2) (Crum et al., 2009). When comparing the candidate minerals listed in Table 2.2, pyrosmalite-(Mn) (formerly manganpyrosmalite) and brokenhillite both contain significant concentrations of Cl; however, the lack of alkali compromises their ability to be good candidates for the spent salt. Wadalite (sodalite group) is a closer compositional match to the spent salt,

but again the lack of alkali in this mineral means it is not the most ideal candidate for immobilizing the cation fraction of the waste. According to the list in Table 2.2, the best candidate materials for both the Cl^- and the alkali are sodalite and cancrinite (quadridavyne).

Another commonly studied ceramic material for waste form applications is the apatite structure, or $M_5(YO_4)_3X$, where "M" can be any number of atoms, i.e., M^{1+}, M^{2+} or M^{3+}; "Y" (not yttrium) is P, Si, V, or Os; and "X" is F, Cl, I, OH, or O (Park et al., 2002; Dong et al., 2002). This suggests a wide range of compositional flexibility in which M could be anything from alkalis (M^{1+}) to alkaline earths (M^{2+}) to lanthanides (M^{3+}), all of which are components of the waste, although the alkaline earths are the most commonly found cations to occupy these sites in naturally occurring apatites.

Typical apatites found in nuclear waste solids are lanthanide (Ln) silicate isomorphs of the natural apatite that have a composition of $Ca_{4-x}Ln_{6+x}(SiO_4)_6(PO_4)_yO_2$ where the actinides can readily substitute for the Lns. Also, iodide is expected to be present in small fractions in the waste stream and could also be incorporated into an iodoapatite structure. Apatites have a few drawbacks. One is the low waste loading by mass (see Table 2.2). Another is their ability to become amorphous after radioactive decay that induces microcracking from volume expansion, e.g., α-decay of Cm from Ln component (Weber et al., 1979). A detailed presentation of these radiation-induced changes can be found elsewhere (Ewing et al., 1995).

Table 2.2. Naturally occurring minerals investigated as potential waste forms (*Mineralogy Database*, 2011). The theoretical waste loading limits (in mass%) for each mineral type based on Cl or alkali (on Na basis) are listed in parentheses and are adjusted based on the fraction of the alkali in the waste versus the fraction coming from the reactants (e.g., $NaAlO_2$).

Mineral Name	Mineral Group	Chemical Formula	Cl	Alkali
Pyrosmalite-(Mn)	Pyrosmalite	$(Mn,Fe^{2+})_8Si_6O_{15}(OH,Cl)_{10}$	29.30 (51)	0.00 (0)
Wadalite	Sodalite	$Ca_6Al_5Si_2O_{16}Cl_3$	13.40 (23)	0.00 (0)
Brokenhillite	Pyrosmalite	$(Mn,Fe)_{32}(Si_{24}O_{60})OH_{29}Cl_{11}$	9.06 (16)	0.00 (0)
Quadridavyne	Cancrinite	$(Na,K)_6Ca_2Al_6Si_6O_{24}Cl_4$	13.20 (23)	12.84 (27)
Chorapatite	Apatite	$(Na,Ca)_5(PO_4)_3Cl$	8.14 (14)	26.41 (16)
Sodalite	Sodalite	$Na_8Al_6Si_6O_{24}Cl_2$	7.32 (13)	18.98 (15)

The FY2009 scoping studies showed that sodalite can be easily synthesized with a solution-based process (Crum et al., 2009). However, it is produced in the form of a fine powder with particle sizes on the order of a few microns; the small particle size produced by this technique makes it necessary to treat the powders to form a monolith. In this study, the powders were pressed into pellets (19–25 mm diameter, 5–10 mm thick) and fired to achieve the desired bulk density (>90% of theoretical density). Sodalite was the predominant structure that formed during the solution-based process during the scoping studies of FY2009. Cancrinite, while identified as the best candidate mineral in terms of maximum waste loading, was produced during the process but converted to sodalite upon firing.

The FY2010 efforts focused on two areas that include 1) increasing the bulk density of the sodalite waste form and 2) synthesis of a cancrinite waste form (Riley et al., 2010). To increase bulk density of the sodalite, the firing temperature was varied to determine the maximum firing temperature above which the volatility of Cl became significant. First, the optimum firing temperature was determined based on bulk density, Cl loss, and PCT response. Second, a sintering aid (1–7 mass%) was added in the form of powdered borosilicate glass (NBS-1, see Table 3.3) (Vienna et al., 1998). The powdered glass was added during the process, directly after gel formation before the gel was dried.

Results in FY2010 showed that full density was achieved in Sodalite 5A at 950°C. By adding the NBS-1 glass sintering aid, we showed that similar density could be achieved at 850°C. However, the small crystallite grain sizes resulted in PCT responses that were higher than expected for the waste form. In

general, in terms of phase assemblages, we saw that as firing temperature was increased, the concentrations of unreacted salts and zeolite phases were reduced. In some cases, sodalite increased as the unreacted salt and zeolite disappeared; however in most cases, this resulted in the formation of sodium aluminosilicates, e.g., nepheline and carnegieite. The sodium aluminosilicates are higher temperature phases than zeolites or sodalites, and thus both of these phases can convert to sodium aluminosilicates with increased heat-treatment temperature.

Based on the literature, sodalite is more likely to form when the only anion present is Cl^-. If significant concentrations of CO_3^{2-}, NO_3^-, or OH^- are present, then cancrinite can become the preferred structure (Ocanto et al., 2008; Ocanto et al., 2009; Liu et al., 2007). In FY2010, we made changes to the solution chemistry in an attempt to form cancrinite in place of sodalite (Riley et al., 2010). The additions of NO_3^-, CO_3^{2-}, and OH^- were examined to determine which, if any, would form cancrinite instead of sodalite, since cancrinite has a higher theoretical waste loading (23 mass%) than sodalite (13 mass%). The targeted compositions for sodalite synthesis are given in Table 2.3. Note: the method for cancrinite mineral synthesis is presented in our earlier work (Riley et al., 2010).

Table 2.3. Target elemental compositions of sodalite formulations (in molar formula units), glass sintering aids, and waste loading (mass % addition to original composition). The "Label" is used to identify the samples in later sections. "Ln" denotes the addition of lanthanides. Here, "CS" is colloidal silica, "TEOS" is tetraethyl orthosilicate, and "Ge-EtO" is germanium(IV) ethoxide.

Label:	**Ideal**	**S5A**	**S5C**	**S5D**	**S6**
Component/Property	**Sodalite**	Series	Series	Series	Series
Al	6.0	6.0	6.0	6.0	6.0
Si/Ge	6.0	6.0	6.0	6.0	6.0
Si/Ge additive	-	CS	TEOS	Ge-EtO	CS
Alkaline earth + Ln	-	0.1	0.1	0.1	0.1
Alkali	8.0	7.9	7.9	7.9	7.9
Cl^-, NO_3^-	2.0	2.0	2.0	2.0	2.0
O	24.0	24.0	24.0	24.0	24.0
Glass sintering aid, mass%	-	-	5*	-	1.0–7.0†
Total	46.0	46.0	46.0	46.0	46.0
Waste loading, mass%	-	13.7	13.7	10.7	12.7–13.5

*Sintering aids listed Table 3.3 (other than NBS-1) were used. †NBS-1 glass was used.

2.2 Tellurite Glasses: Background

Tellurite glass was selected as the candidate host for the XCl_{20} waste components in FY2009 because these glasses showed promise for moderate-to-high mass% loadings of up to ~15 mass% XCl_{20} and had very high volumetric waste loading—or storage density, ρ_S—due to the high density of normal tellurite glass, $\rho_S > 5\times10^3$ kg/m^3 (Crum et al., 2009).

The tellurite glass compositions that we fabricated in FY2009 were randomly selected, were not optimized, and did not have high chemical durability. Thus, to better evaluate these glasses as a potential waste form, a literature study was conducted in FY2010 to identify promising candidate formulations for further investigation (Riley et al., 2010). This was followed up with a scoping study in which glasses were fabricated on a small scale (~5 g) to evaluate the glass formation ability with and without the XCl_{20} simulant. The scoping study was designed to assess some basic properties of a wide variety of simple tellurite glass compositions; these glasses were designated "S-series" glasses.

From the scoping studies, five systems were identified for further investigation and included tellurite glasses with the following additives: PbO, Al_2O_3+B_2O_3, WO_3, P_2O_5, and ZnO. The successful formulations with these five systems were then made in 20-g batches and further characterized; these 20-g

batches were designated "P-series" glasses. The P-series glasses were then characterized with assessments of a few of the properties including the following: volatility and pour viscosity during the melting process, density, microstructure, and chemical durability (assessed with the PCT). A summary of the characterization results from these 20-g glasses is presented in Table 2.4. As seen in Table 2.4, some of the properties for the P-series glasses varied widely, especially the volatility and the chemical durability. The lead-tellurite glasses performed the best and were further investigated in FY2011.

Table 2.4. Summary results for the P-series tellurite glasses that were analyzed with the PCT. The "Glass" column lists those glasses batched on a 20-g scale for the PCT. Batch composition of each glass is listed in mass% additive; the balance is TeO_2. The composition of XCl_{20} is found in Table 2.1. The melting temperature is denoted T_M. The "volatility" is ranked based on degree of "fuming" observed during the melt process, from none (0) to a lot (4). Viscosity (η) was estimated as compared to standards. The overall deviation associated with the density measurements is $\pm 0.015\times10^{-3}$ kg/m^3 (Riley et al., 2010). Phase separation was determined based on visual ("Bulk") and microscopy ("Small") observations. The normalized sodium release during the PCT is given as (NL_{Na}).

Glass ID	Batch Composition (mass% additive)	T_M (°C)	Volatility (0–4)	η (cP)	$\rho\times10^{-3}$ (kg/m^3)	Phase Separation		NL_{Na} (g/m^2)
						Bulk	Small	
P-8	22.0% PbO	705	0	50–100	6.12	-	✔	-
P-11	19.8% PbO, 10.0% XCl_{20}	705	1	10	5.16	✔	-	0.478
P-7	8.8% Al_2O_3, 9.0% B_2O_3	720	0	200	4.44	-	✔	-
P-2	7.9% Al_2O_3, 8.1% B_2O_3, 10.0% XCl_{20}*	690	3	50	4.13	✔	✔	6.71
P-9	25.0% WO_3	725	0	100	5.92	✔	-	-
P-12	22.5% WO_3, 10.0 XCl_{20}	675	4	10	5.11	✔	-	10.3
P-5	8.9% P_2O_5	675	0	400	5.11	-	-	-
P-14	8.1% P_2O_5, 10.0% XCl_{20}	675	2	50–100	4.72	✔	✔	86.0
P-4	18.0% ZnO	730	0	100	5.49	-	-	-
P-13	16.2% ZnO, 10.0% XCl_{20}	730	1	10	4.67	-	-	88.9

*The composition of the Echem salts was batched with a different XCl_{20} (XCl_y) in glass P-2 (see Appendix A)

2.3 Te-O Structures Present in Tellurite Glasses

2.3.1 Tellurite Glass Structural Configurations

A tellurite glass network consists of several different structural arrangements depending on the specific glass network modifiers, intermediates, and other additives present in the glass. Analytical techniques including X-ray diffraction (XRD) (Brady, 1956, 1957; Dimitriev et al., 1987), neutron diffraction (Neov et al., 1979), Fourier transform infrared (FTIR) spectroscopy (Dimitriev et al., 1987; Heo et al., 1992), Raman spectroscopy (Khatir et al., 1993; Duverger et al., 1997; Dimitriev et al., 1983; Kashchieva, 1984; Sekiya et al., 1994a; Chowdari and Kumari, 1999; Murugan et al., 2005, 2006; Sekiya et al., 1994b), ^{125}Te-based nuclear magnetic resonance (NMR) (Sakida et al., 2001; Sakida et al., 1999a, b), extended X-ray absorption fine structure (Shimizugawa et al., 1995; Yamamoto et al., 1994), and Mössbauer spectroscopy (Nishida et al., 1990) have been used to determine the various structural configurations present in tellurite glasses. Observations of tellurite structural units have been discussed in the literature as they are affected by oxide additives including alkalis (Rao and Bhat, 2001; Bhat et al., 2004; Arnaudov et al., 1982; Akagi et al., 1999), alkaline earths (Arnaudov et al., 1982), and transition metals (Arnaudov et al., 1982; Kozhukharov et al., 1986; Bürger et al., 1992).

Thus far, at least eight different Te structural units have been identified that can be broadly categorized as either asymmetrical trigonal bipyramidal (*tbp* or TeO_4) or trigonal pyramidal (*tp* or TeO_3) units. Notations for these different structural units are presented in Table 2.5 with pictorial representations in Figure 2.1. In each of the tellurite structural units, there exists a lone pair of electrons at the unoccupied equatorial position on the Te atom, a position that is generally accepted as being present in one of the sp^3d hybridized orbitals (Lindqvist, 1968; Rao and Bhat, 2001).

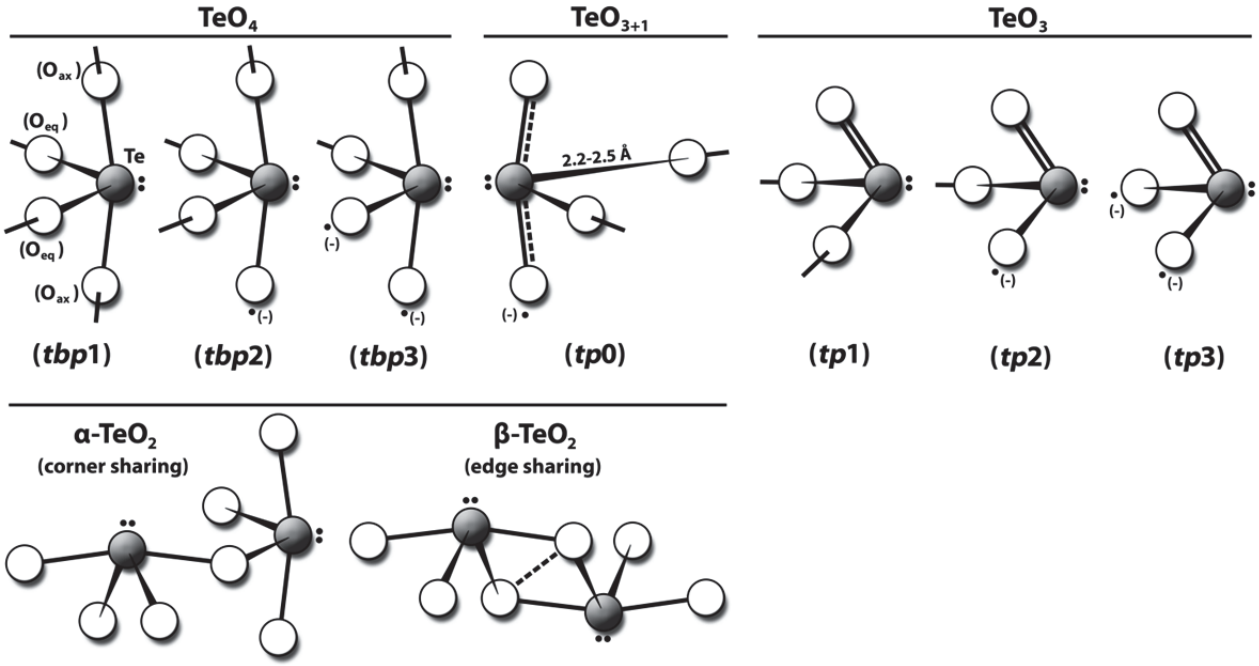

Figure 2.1. TeO_4 trigonal bipyramidal, *tbp*, and TeO_3 trigonal pyramidal, *tp*, structural units in tellurite glasses based on other representations in the literature (Himei et al., 1994; Sekiya et al., 1994b; Sakida et al., 1999a; Lindqvist, 1968; Rao and Bhat, 2001; Sakida et al., 1999b). Species are presented in order of decreasing quantity of bridging oxygens, i.e., from four to two for *tbp* and from two to zero for *tp*. Oxygen assignments are broken down into equatorial positions (O_{eq}) and axial positions (O_{ax}) for *tbp*1. According to Lindqvist, the distance between the Te atom and axial oxygens (i.e., Te–O_{ax}) is 2.08 ± 0.02 Å, and the distance between the Te atom and equatorial oxygens (i.e., Te–O_{eq}) is 1.90 ± 0.02 Å (Lindqvist, 1968). Non-bridging oxygen assignments were arbitrarily chosen.

The different structural units shown in Figure 2.1 are referred to with a wide variety of notations in the literature. The most common are the polyhedral notations (e.g., TeO_4, TeO_3) and the $T^c_{b.o.}$ notation, where "T" is the Te atom, "c" is the charge on the structural unit, and "b.o." is the number of "bridging oxygens" included in the structural unit. For example, according to Lindqvist, in crystalline α-TeO_2, the Te has a lone pair of electrons in the valence shell, and the preferred structural units are *tbp*1 and T^0_4 (Lindqvist, 1968; Bhat et al., 2004) (see Table 2.5 and Figure 2.1).

When modifiers, intermediates, and other additives are introduced into the tellurite network, the *tbp*1 structural units are no longer constrained, extending the Te-O interatomic bonds (Akagi et al., 1999; Neov et al., 1978). Consequently, additives stabilize the vitreous state (Arnaudov and Dimitriev, 2001). In the *tbp*1 configuration, the distance between the Te atom and both axial oxygens (i.e., Te–O_{ax}) is 2.08 ± 0.02 Å, and the distance between the Te atom and both equatorial oxygens (i.e., Te–O_{eq}) is 1.90 ± 0.02 Å (Lindqvist, 1968; Kozhukharov et al., 1986). It is commonly accepted that tellurite glasses possess the α-TeO_2 framework structure with a density of ~5.75 g/cm^3.

Table 2.5. Tellurium oxide structural units present in glass according to the literature (Himei et al., 1994; Sekiya et al., 1994b; Sakida et al., 1999a; Lindqvist, 1968; Rao and Bhat, 2001; Sakida et al., 1999b).

Unit	*tbp*1	*tbp*2	*tbp*3	*tp*0	*tp*1	*tp*2	*tp*3
Reference	(Himei et al., 1994)	(Himei et al., 1994)	(Sekiya et al., 1994b)	(Sekiya et al., 1994b)	(Himei et al., 1994)	(Himei et al., 1994)	(Sakida et al., 1999a)
Polyhedron	TeO_4	TeO_4 $TeO_{3/2+1}^-$	TeO_4	TeO_{3+1}	TeO_3 $TeO_{2/2+1}$	TeO_3 $TeO_{1/2+2}^-$	TeO_3 $TeO_{1+1}^-{}_{+1}^-$
$T^c_{b.o.}$ notation	T_4^0	T_3^{-1}	T_2^{-2}	T_2^{-1}	T_2^0	T_1^{-1}	T_0^{-2}
NMR notation (Sakida et al., 2001)	N_4^0	N_4^-	N_4^{2-}	N/A	N_3^0	N_3^-	N_3^{2-}
	(α-TeO_2 type)			(Distorted)	(Bridging)	(Terminal)	(Isolated)
Bonding	$TeO_{4/2}$	$O_{3/2}Te\text{-}O^-$	$O_{2/2}Te(\text{-}O^-)\text{-}O^-$	$O_{1/2}Te(\text{-}O^-)(\text{-}O\text{---}Te)(\text{---}O)$	$O_{2/2}Te{=}O$	$O_{1/2}Te(=O)\text{-}O^-$	$O{=}Te(\text{-}O^-)\text{-}O^-$
Q^n	Q^4	Q^3	Q^2	$Q^{1\text{-}3}$	Q^2	Q^1	Q^0
Number of non-bridging oxygens (including double bonds)	0	1	2	1*	1	2	3
Number of double bonds	0	0	0	0	1	1	1
Equivalent in network	TeO_2	$[Te_2O_5]^{2-}$	$[Te_2O_6]^{4-}$	$[Te_2O_5]^{2-}$	TeO_2	$[Te_2O_5]^{2-}$	$[TeO_3]^{2-}$

*+1 long bond; another O is long-bonded to next Te

In contrast with the α-TeO_2 crystal, the β-TeO_2 crystal has an orthorhombic, layered structure, consisting of edge-shared trigonal bipyramidal TeO_4 units (Figure 2.1) with a higher density at ~6.04 g/cm^3 (Patnaik, 2003). In the *tp* structures, only three oxygens are bonded to the Te atom, and one of the oxygens is double bonded (Figure 2.1). A detailed explanation for the formation of these structural reconfigurations in tellurite glasses has been given elsewhere (Rao and Bhat, 2001).

Another structural unit, TeO_{3+1}, can be found in tellurite glasses when one Te-O_{ax} is stretched so that the local coordination is three with a fourth oxygen some farther distance away (Kozhukharov et al., 1986) (Figure 2.1). From another perspective, TeO_{3+1} units result from a continuous section of a tellurite glass chain of mostly TeO_4 *tbp* units with TeO_3 *tp* units on either end, forming *tp*2-*tbp*3-*tp*2, or a $[Te_3O_8]^{4-}$ unit (Sekiya et al., 1994b). If several of these sections are put together, the end *tp* units of each section resemble "loosely associated" TeO_{3+1}, with the "other" oxygen being contributed by the next chain fragment. This gives a *tp*0-*tbp*3-*tp*0 sequence that can be represented as $[Te_3O_8]_\infty^{4-}$ (Sekiya et al., 1994b).

2.3.2 Effect of Selected Additives on Tellurite Glass Structure

No data was found in the literature discussing the structural effect of the XCl_{20} components in the compositional variation glass systems. However, some literature was found on the structural effects of these oxide additives in tellurite glasses (Khatir et al., 1993; Duverger et al., 1997; Dimitriev et al., 1983; Kashchieva, 1984; Sakida et al., 2001; Sekiya et al., 1992a; Rada et al., 2008; Rong et al., 1992; Sekiya et al., 1994a; Chowdari and Kumari, 1999; Murugan et al., 2006; Sekiya et al., 1994b; Bürger et al., 1992; Murugan et al., 2005; Kozhukharov et al., 1986). That data is summarized below and was used to interpret the data for the compositional variation glasses with XCl_{20} additions. Below, we focus primarily on structural interpretations from Raman spectra.

TeO_2-PbO glasses. Lead-tellurite glass Raman spectra have been reported previously (Khatir et al., 1993; Duverger et al., 1997). Because TeO_3 structural units tend to dominate the glass structure as PbO is added to tellurite glass, Pb is deemed to act as a network modifier (Silva et al., 2001). However, increasing Pb also promotes the conversion of PbO_6 octahedra into PbO_4 tetrahedra with more non-bridging oxygens (Khatir et al., 1993; Silva et al., 2001).

TeO_2-Al_2O_3-B_2O_3 glasses. Glass formation in alumino-borate-tellurite systems has been investigated in the past though no references on Raman spectroscopy in this ternary system were found (Dimitriev et al., 1983; Kashchieva, 1984). However, structural studies were found in the literature on binary TeO_2-Al_2O_3 systems (Raman) and TeO_2-B_2O_3 systems (Raman and infrared spectroscopies) (Sakida et al., 2001; Sekiya et al., 1992a; Rada et al., 2008; Rong et al., 1992). Glass structure studies of TeO_2-Al_2O_3 systems show that, with increasing Al_2O_3, TeO_4 *tbp* and AlO_6 polyhedra decrease in favor of TeO_3 *tp* and AlO_4 and AlO_5 units, while Al-O-Al bridging bonds are not formed up to ~14 mole% Al_2O_3 additions to TeO_2 (Sakida et al., 2001). AlO_4 units are preferably connected to *tbp*2 units, while AlO_5 and AlO_6 units are preferably connected to *tp*2 units. TeO_2-B_2O_3 systems with low B contents are generally believed to be continuous structures composed of mostly TeO_4 *tbp* containing BO_4 and a small fraction of BO_3 and B_2O_5 groups (Sekiya et al., 1992a). As B content increases, the amount of TeO_3 groups increases. Some TeO_6 has even been proposed when B_2O_3 is 30 mole% or more (Rada et al., 2008). Other studies indicated that BO_3 and BO_4 are present as discrete units and not as borate rings in glasses with 15–30 mole% B_2O_3. TeO_3 units were proposed at these compositions as well (Rong et al., 1992).

TeO_2-WO_3 glasses. Tungstate-tellurite glass Raman spectra have been reported in the literature (Sekiya et al., 1994a; Chowdari and Kumari, 1999). The structure of these glasses is generally thought to consist of a primary tellurite network with regions of quasi-phase-separated "clusters" of WO_6 or WO_{4+2} polyhedra.

TeO_2-P_2O_5 glasses. Phospho-tellurite glass Raman spectra have been discussed recently, notably in (Murugan et al., 2006, 2005). Phosphate glasses consist of PO_4 tetrahedra composed of a single double-

bonded, non-bridging oxygen and three bridging oxygens. As metal oxides (e.g., TeO_2) are added to the glass network, P–O–P bonds are broken, resulting in more non-bridging oxygens.

TeO_2-ZnO glasses. Zinc oxide-tellurite glass Raman spectra have also been reported in the literature (Duverger et al., 1997; Sekiya et al., 1994b; Kozhukharov et al., 1986; Bürger et al., 1992). The role of ZnO in ZnO-TeO_2 glasses is described as both a modifier and as forming ZnO_6 or ZnO_{4+2} polyhedra within the glass network (Kozhukharov et al., 1986). As a modifier, ZnO converts TeO_4 *tbp* or TeO_{3+1} units to TeO_3 *tp* units, creating non-bridging oxygens similar to the effect of adding alkali oxides and alkaline earth oxides to tellurite glass (Sakida et al., 1999b; Sekiya et al., 1994b; Tatsumisago et al., 1994). The main difference between ZnO, alkali oxides, and possibly MgO (or other alkaline earth oxides) is that ZnO also tends to form part of the network backbone of the glass structure.

For example, Kozhukharov et al. studied an 80 mol% TeO_2+20 mol% ZnO binary glass with neutron diffraction with radial distribution function (RDF) analysis and observed a mean atomic distance, $\bar{R}$, between oxygen bonds of $\bar{R}_{O-O}$ = 2.95 Å (Kozhukharov et al., 1986). This correlates closely with that of α-TeO_2, $\bar{R}_{O-O}$ = 2.85 Å. Kozhukharov et al. claim that the offset is due to the O–O distances in the ZnO_{4+1+1} polyhedra. Also, RDF analysis gave a measured average coordination number of the Te atoms in this glass composition of 3.35, suggesting that ~35% of the Te atoms were *tbp*1, and 65% had a lower coordination number (i.e., *tp*3 units and TeO_3-type units). TeO_2-ZnO glasses appeared to have more *tp* than *tbp* structural units. Bürger et al. applied Raman spectroscopy to the same TeO_2-ZnO binary system in addition to neutron diffraction and RDF analysis and found that the TeO_4 polyhedra were easily deformed to give variations in the Te–O_{ax} bonds (Bürger et al., 1992) (Figure 2.1). They also determined that TeO_{3+1}:TeO_4 groups were a function of composition: higher ZnO concentration led to more disordered Te polyhedra, thereby increasing TeO_{3+1}:TeO_4.

2.3.3 Effect of Chlorides on the Tellurite Glass Structural Units

The structural effects of chlorides on the network of tellurite glasses have been studied to a lesser extent (Rao and Bhat, 2001; Bhat et al., 2004; Rojo et al., 1990; Tanaka et al., 1988a). Using XRD, Iwadate et al. determined that the average coordination number of the Te atoms in LiCl-Li_2O tellurite glasses was between 3 and 4, indicating a mixture of *tp* and *tbp* Te species (Iwadate et al., 2000). Two types of Te–O–Te linkages are present in tellurite glasses, one formed by connecting a long Te–O bond (~2.0 Å) and a short Te–O bond (<2.0 Å) and the other by joining two structural units with Te–O bonds (>2.0 Å). Iwadate et al. showed that two types of Te–O correlations measured ~2 Å and demonstrated the presence of *tbp* and *tp* species, a coordination in the range of *tp*3 and *tbp*4 species for both glasses, i.e., $n_{\mathrm{Te-O_{ax}}} + n_{\mathrm{Te-O_{eq}}} + n_{\mathrm{Te-Cl}}$ = ~3.3–3.4, where n_i is the average coordination number of the *i*-th bond). This led to their conclusion that the Cl^- substituted for O^{2-} in the network.

Rao and Bhat and Bhat et al. made several borotellurite glasses with and without Li_2O, including varying additions of the LiCl, which they did not expect to influence the tellurite glass network structure (Rao and Bhat, 2001; Bhat et al., 2004). In their studies, adding LiCl resulted in a *tbp*1 → *tp*1 conversion. In contrast, when studying TeO_2-Li_2O-LiCl glasses through vibrational spectroscopy, Tanaka et al. found that when LiCl was added to a TeO_2-Li_2O matrix, the LiCl formed a non-bridging oxygen bond, Te–Cl_{eq}, in place of one of the Te–O_{eq} bonds, e.g., Te–O(1) in Figure 2.1 (Tanaka et al., 1988a). This, in turn, strengthened the Te–O_{ax} bond and suppressed formation of the *tp* species.

3 METHODS

3.1 High-Halide Minerals

Unique identifiers were applied to the various sets of high-halide minerals that we studied in fiscal year (FY) and calendar year (CY) 2011 and are is presented in Table 3.1.

Table 3.1. Labels for the various sets of high-halide minerals fabricated in FY/CY2011. Here, CS, TEOS, and Ge-EtO denote that samples were made with colloidal silica, tetraethyl orthosilicate, and germanium(IV) ethoxide, respectively. See Table 2.3 for the S5A and S6A compositions.

Sample series	Description
S5A-CS	Samples were made with the 5A composition and CS as the 4-coordinated Group IV component
S5C-TEOS	Samples were made with the 5A composition and TEOS as the 4-coordinated Group IV component
S5D-GeEtO	Samples were made with the 5A composition and Ge-EtO as the 4-coordinated Group IV component
S6A-CS	Samples were made with the 6A composition and CS as the 4-coordianted Group IV component

3.1.1 Solution-Based Fabrication Method for Halide Minerals

A solution-based process was used to form the high-halide minerals, followed with cold pressing and firing to convert the dried gel into a monolithic waste form. Figure 3.1 shows a schematic of the experimental apparatus; these are the steps taken during the process:

1) Simulated spent salt ($X\text{Cl}_{20}$, see Table 2.1) was dissolved in deionized water (DIW) – see Figure 3.1-(A).
2) Dissolved salt was heated to ~75°C in the reaction beaker, which was heated by an oil bath (Table 3.2). The solution was continuously stirred with a serpentine Pt wire throughout the formation process.
3) The silica (SiO_2) or germania (GeO_2) source was slowly added as a separate solution to the dissolved salt solution—see Figure 3.1-(B). The Si-O or Ge-O source is designated in Table 2.3 for each sample series.
4) The solution was then gelled by slow addition of sodium aluminate solution—see Figure 3.1-(C).
5) For some of the batches, a sintering aid (1–7 mass%) was added at this stage in the form of powder (not shown in Figure 3.1). See Table 3.3 for a list of the sintering aids studied along with the glass compositions and a few properties.
6) The gel was stirred and heated for 10–30 min to drive off excess water.
7) Lastly, the gel-containing beaker was heated at 105°C overnight to complete the drying process.

The dried material was a moderately bound fine powder. The amounts of waste simulant, colloidal silica, and sodium aluminate added were determined by the target waste form composition.

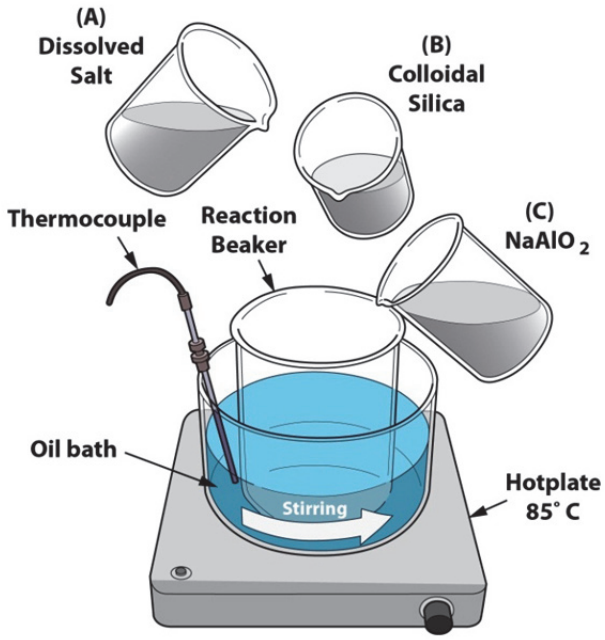

Figure 3.1. Schematic of the simplified solution-based process.

Table 3.2. Concentration of $X\text{Cl}_{20}$ salts representative of the salt waste added in Step 1), above.

Component	Concentration, g/L
KCl	68.43
LiCl	53.77
NaCl	21.09
$NdCl_3$	9.66
CsCl	7.12
$CeCl_3$	6.34
$LaCl_3$	4.13
$BaCl_2$	3.63
$SmCl_3$	2.88

For the silica-based sodalites that were made with TEOS as the silica source, a representative process included the following:

1) Added 30.0 mL of salt solution (see Table 3.3) to a 250 mL beaker with a platinum stirring rod
2) Added 52.8 mL of TEOS to the beaker (99.0% purity, Sigma-Aldrich, St. Louis, MO)
3) Added 51.0 mL of $NaAlO_2$ (38% solution, USALCO, LLC, Baltimore, MD)
4) Added 13.8 mL of absolute ethanol
5) Added 2.05 g of glass (on a 5 mass% basis)
6) After the glass was added, the viscosity greatly increased to form a solid in an exothermic reaction (~30 seconds)
7) Beaker was placed in a special drying oven, (approved for drying flammables), overnight.
8) The resulting product was powdered and pressed into pellets for analysis.

The glass sintering aids that we studied in FY2011 are presented in Table 3.3. The sodium borosilicate glass sintering aids, denoted as SA-###, were selected based on their lower melting temperatures and were labeled based on the predicted temperatures (~700, 750, 800, and 850°C) at which the viscosity was predicted to be 100 Pa·s with SciGlass models (v 7.0, ITC, Inc., Newton, MA). The NaAlP-B4 is discussed in detail elsewhere (Donald et al., 2007) and P-8 is a tellurite glass discussed here as well as in our previous work (Riley et al., 2010). The NaAlP-B4 glass was selected based on past success as a sintering aid for an apatite mineral waste form (Donald et al., 2007). The P-8 glass is one of the tellurite glasses discussed here that was selected because it has a high affinity for the Echem waste components and has a good chemical durability (Riley et al., 2010). Each of these binders was fabricated with a melt-quench technique and then powdered for addition in Step 5, above.

Table 3.3. Compositions (in mass%) of glass sintering aid (SA) additions tested in FY2011. The NBS-1 (Vienna et al., 1998) glass from FY2010 studies is listed for comparison purposes (Riley et al., 2010). Some of the data was not available for TePbO (TPb_0) or NaAlP-B4 for comparison, e.g., T_L represents the liquidus temperature, in place of the T_M for NaAlP-B4.

Components	**NBS-1**	SA-700	SA-750	SA-800	SA-850	NaAlP-B4	TePbO
SiO_2	**60.00**	28.57	40.83	42.5	48.31	-	-
Na_2O	**15.00**	38.32	37.49	32.88	34.89	40.0	-
B_2O_3	**10.00**	33.11	21.68	24.62	16.80	2.0	-
Li_2O	**5.00**	-	-	-	-	-	-
Al_2O_3	**5.00**	-	-	-	-	19.0	-
ZrO_2	**5.00**	-	-	-	-	-	-
P_2O_5	-	-	-	-	-	39.0	-
TeO_2	-	-	-	-	-	-	78.00
PbO	-	-	-	-	-	-	22.00
T @ 100 Pa·s	**963**	700	751	805	850	[b]	<600[a]
T_M, °C	**1250**[a]	850	900	950	1000	742 (T_L)	650[a]

(a) These values are estimated
(b) These values are unknown

3.2 Tellurite Glasses

3.2.1 Tellurite Glass Fabrication

All of the tellurite glasses discussed here were batched from oxides, boric acid, and chlorides of high purity (all > 99.0% pure). The XCl_{20} components that were added to the waste-loaded glasses were added in the ratios presented in Table 3.4. In all cases, the glasses were mixed in a mortar and pestle, the powders were then placed in a Pt/10%Rh crucible with a Pt/10%Rh lid, melted for 30 minutes, and quenched by pouring on a stainless steel plate. The as-quenched glasses were subsequently prepared for various tests. The variables in the fabrication parameters included the batch mass and T_M. The T_M used for the tellurite glasses varied. The specific values used for the compositional variation study glasses are presented in Table 2.4 and are listed separately in the text for each set of glasses. The glasses discussed below are grouped into different sections based on the purpose of study and include the following: 1) compositional variation study glasses, 2) lead-tellurite variation study glasses, and 3) structural investigation study glasses.

Table 3.4. Composition of the $X\text{Cl}_{20}$ salt added to the tellurite glasses along with the melting temperatures for some of the components (in order of mass fraction from largest to smallest). The melting temperature (T_M) and bulk density (ρ_B) are also included for each (Haynes, 2011).

Component	Mass%	Mole%	T_M, °C	ρ_B, $\times 10^{-3}$ kg/m^3
KCl	37.99	33.83	771	1.99
LiCl	29.89	46.82	610	2.07
NaCl	11.71	13.30	801	2.17
$NdCl_3$	5.36	1.42	759	4.13
CsCl	3.91	1.54	646	3.99
$CeCl_3$	3.51	0.95	807	3.97
$LaCl_3$	2.29	0.62	858	3.84
$BaCl_2$	2.01	0.64	961	3.9
$PrCl_3$	1.72	0.46	786	4.0
$SmCl_3$	1.61	0.42	682	4.46

The naming convention of the glasses presented in the FY2010 report was changed in this report to make it easier to track the glass by composition as opposed to tracking the glasses by the sequential-numbering sample identification. However, both of these naming conventions are retained here for cross-referencing to our other work (see Table 3.5).

3.2.1.1 Compositional Variation Study Glasses

The glasses for the compositional variation study include ten "P-# series" glasses that were fabricated in FY2010 and were previously discussed in our FY2010 report, but were renamed here for easier cross-reference to the glass compositions (Table 3.5) (Riley et al., 2010). The structural characterizations of these glasses, i.e., X-ray diffraction (XRD) and Raman, will be discussed here in further detail. All of these glasses were fabricated on a 20 g scale and T_M values are listed in our FY2010 report.

Table 3.5. Compositions (in mole%) from tellurite glass compositional variation study batched with and without $X\text{Cl}_{20}$ additions.* These values are also presented in mass% in Figure A.1 (Appendix A), although they are presented here as mole% because that is more appropriate for the discussion of the glass structure. Each of the "+Cl" glasses were batched with a target of 10 mass% $X\text{Cl}_{20}$-loading.

Composition	Pb	Pb+Cl	Al/B	Al/B+Cl	W	W+Cl	P	P+Cl	Zn	Zn+Cl
Glass ID	P-8	P-11	P-7	P-2	P-9	P-12	P-5	P-14	P-4	P-13
TeO_2	83.2	64.8	70.5	59.4	81.3	63.1	90.0	71.2	69.9	56.9
PbO	16.8	13.1	-	-	-	-	-	-	-	-
Al_2O_3	-	-	11.8	10.0	-	-	-	-	-	-
B_2O_3	-	-	17.7	14.9	-	-	-	-	-	-
WO_3	-	-	-	-	18.7	14.5	-	-	-	-
P_2O_5	-	-	-	-	-	-	10.0	7.9	-	-
ZnO	-	-	-	-	-	-	-	-	30.1	24.5
$BaCl_2$	-	0.142	-	0.192	-	0.144	-	0.134	-	0.119
$CeCl_3$	-	0.210	-	0.245	-	0.212	-	0.198	-	0.175
CsCl	-	0.342	-	0.611	-	0.346	-	0.322	-	0.286
KCl	-	7.50	-	8.06	-	7.60	-	7.07	-	6.27
$LaCl_3$	-	0.138	-	0.160	-	0.139	-	0.130	-	0.115
LiCl	-	10.4	-	3.48	-	10.5	-	9.78	-	8.68

Composition	Pb	Pb+Cl	Al/B	Al/B+Cl	W	W+Cl	P	P+Cl	Zn	Zn+Cl
Glass ID	P-8	P-11	P-7	P-2	P-9	P-12	P-5	P-14	P-4	P-13
NaCl	-	2.95	-	2.38	-	2.99	-	2.78	-	2.47
$NdCl_3$	-	0.315	-	0.372	-	0.319	-	0.297	-	0.263
$PrCl_3$	-	0.102	-	0.119	-	0.104	-	0.0963	-	0.0855
$SmCl_3$	-	0.0925	-	0.111	-	0.0936	-	0.0871	-	0.0773

*A different XCl$_{20}$ composition was used for the Al/B+Cl glass than for the other XCl$_{20}$-containing glasses – see previous work (Riley et al., 2010).

3.2.1.2 Lead-Tellurite Waste-Loading Variation Study Glasses

The second set of tellurite glasses fabricated and studied in FY2011 was a series of lead-tellurite glasses with a fixed target TeO_2:PbO ratio (by mass) of 3.5455 and a fixed target ratio of Te:Pb (by mole) of 4.9583, both based on the P-8 and P-11 glasses. This glass system was chosen based on the chemical durability of these glasses according to the FY2010 results. The fraction of XCl$_{20}$ added to the baseline lead-tellurite glass, TPb$_0$, was varied from 0 to 22.5 mass%. The compositions of these glasses are listed in Table 3.6, in which the ratios between the XCl$_{20}$ components can be extrapolated from Table 3.5 (mole%) or Figure A.1 (Appendix A, mass%). All of these glasses were fabricated in 30-g batches and melted at 700°C for 30 minutes. It is worth noting that the TPb$_{14}$ glass was batched two times to verify the properties due to some anomalies in the data for this glass.

Table 3.6. Compositions of lead-tellurite variation study glasses in both mass% and mole%. The subscripts on the glass identification (ID) represent the XCl$_{20}$-loading in mass%. TPb$_0$ and TPb$_{10}$ represent compositions similar to P-8 and P-11, respectively, from previous work (Riley et al., 2010) but these glasses were all melted at 700°C and with a different target mass (30 g vs. 20 g). The sequential glass numbering identification, or "Alternate ID", is also provided for tracking purposes.

Glass ID	Alternate ID	Mass%			Mole%		
		TeO_2	PbO	XCl$_{20}$	TeO_2	PbO	XCl$_{20}$
TPb$_0$	T2G-21	78.0	22.0	0.0	83.2	16.8	0.0
TPb$_5$	T2G-22	74.1	20.9	5.0	73.3	14.8	11.9
TPb$_{10}$	T2G-23	70.2	19.8	10.0	64.8	13.1	22.1
TPb$_{12.5}$	T2G-24	68.3	19.2	12.5	60.9	12.3	26.8
TPb$_{14}$	T2G-31	67.1	18.9	14.0	58.7	11.8	29.5
TPb$_{15}$	T2G-26	66.3	18.7	15.0	57.3	11.5	31.2
TPb$_{17.5}$	T2G-25	64.4	18.1	17.5	53.9	10.9	35.2
TPb$_{22.5}$	T2G-30	60.5	17.0	22.5	47.7	9.6	42.7

3.2.1.3 Structural Variation Study Glasses

The last series of tellurite glasses, the structural variation study glasses, was designed to provide better insight into the effects of composition on the glass structure. Several different sets of glasses were fabricated in which various components were altered individually, in most cases. These different sets of glasses are presented and discussed below.

Set 1: TeO_2:PbO. The purpose of these glasses was to investigate the glass formation in lead-tellurite glasses with a lower mass fraction of PbO than that used for the lead-tellurite variation study glasses, i.e., 22 mass% PbO (with a TeO_2 balance) where TeO_2:PbO = 3.545 (by mass). The compositions of this set of glasses are presented in Table 3.7.

Table 3.7. Compositions for T2G-21, T2G-21b, T2G-21c, and T2G-21d (in mole%) in which the mass% of PbO was 22, 20, 18, and 16 mass%, respectively. The baseline glass for this series is T2G-21, listed in bold type.

Glass ID:	**T2G-21**	T2G-21b	T2G-21c	T2G-21d
TeO_2	**83.22**	84.83	86.43	88.01
PbO	**16.78**	15.17	13.57	11.99
m(TeO_2:PbO)	**3.55**	4.00	4.56	5.25
M(Pb:Te)	**0.202**	0.179	0.157	0.136

Set 2: PbO/$PbCl_2$. The purpose of this study was to look at the structural effect of the anion in the lead-tellurite glasses where lead was added as either PbO or $PbCl_2$ and the Te:Pb molar ratio was fixed at 0.202, to match that of T2G-21 (TPb_0), where "Pb" = total Pb. This variation method was chosen so the amount of Te and Pb atoms interacting in the glass would be equivalent between the glasses. These compositions are presented in Table 3.8.

Table 3.8. Composition of $PbCl_2$-PbO compositional variation glasses to study the structural effect of the anion in the lead-tellurite glasses. For all of the glasses in this series, the molar ratio, *M*, of Pb:Te was fixed at 0.202. The baseline glass, T2G-21, is listed in bold type for reference.

Glass ID:	**T2G-21**	T2G-32	T2G-33
		Mole%	
TeO_2	**83.22**	83.22	83.22
PbO	**16.78**	-	8.39
PbCl	**-**	16.78	8.39
		Mass%	
TeO_2	**78.00**	74.00	75.95
PbO	**22.00**	-	10.71
PbCl	**-**	26.00	13.34
M(Pb:Te)	**0.202**	0.202	0.202

Set 3: XO_{20} versus XCl_{20}. The purpose of this study was to look at the glass structural effect of the XCl_{20} anions. Thus, for T2G-34, all of the XCl_{20} components were replaced by the oxide versions where the cation ratios (by mole) were maintained from the 5 mass% XCl_{20}-loaded glass, T2G-22, and the XO_{20}-loaded glass. Thus, ratios of Te and Pb to each of the waste component cations, (Cat.), remained fixed between the two glasses, i.e., Te:Cat. and Pb:Cat., respectively. The ratio of Te and Pb to the total moles of the waste component cations were fixed at 6.16 and 1.24, respectively, for both T2G-22 and T2G-34. The compositions, corresponding ratios, and the XO_{20} composition are presented in Table 3.9.

Table 3.9. Summary of compositions for the waste-component-anion substitution glasses as well as the composition of XO_{20} with values sorted by mole%. T2G-34 was fabricated from oxide versions of the chloride waste components in which the same total waste component cations (Cat.) were identical to the equivalent glass batched with the chloride components, T2G-22, thus T2G-22 serves as a reference for this study. Thus, the ratios of Te:Cat and Pb:Cat were fixed at 6.16 and 1.24, respectively. As with the other lead-tellurite glasses, the Pb:Te ratio for these glasses was fixed at 0.202.

Glass ID:	**T2G-22**	T2G-34
	Mass%	
TeO_2	**74.1**	74.6
PbO	**20.9**	21.0
XCl_{20}	**5.0**	
XO_{20}		4.4
	Mole%	
TeO_2	**73.3**	77.9
PbO	**14.8**	15.7
XCl_{20}	**11.9**	
XO_{20}		6.4
M(Pb:Te)	**0.202**	0.202
M(Te:Cat.)	**6.16**	6.16
M(Pb:Cat.)	**1.24**	1.24

Component	Mole%	Mass%
Li_2O	46.5	19.09
K_2O	33.6	43.48
Na_2O	13.2	11.25
Cs_2O	1.53	5.93
Nd_2O_3	1.41	6.51
BaO	1.27	2.68
Ce_2O_3	0.940	4.24
La_2O_3	0.617	2.76
Pr_2O_3	0.458	2.08
Sm_2O_3	0.414	1.98

Set 4: PbO-KCl/K_2O and Set 5: ZnO-KCl/K_2O. The purpose of these studies was to compare the structural differences between PbO/ZnO glasses with additions of potassium as either a chloride or an oxide. The purpose of adding potassium as either KCl or K_2O was to determine the anion effect on the structure. For each of these sets (PbO or ZnO), the ratios between the metal additive and TeO_2 were kept constant from the original P-series glasses and the K:Te and K:M (where M = Pb,Zn) ratios were also kept constant for each system. The PbO (P-8 and P-11) and ZnO (P-4 and P-13) glasses performed very differently during the PCT and this study was designed to investigate the possibility of structural differences in these more simple glass formulations (Table 2.4). Compositions for the PbO and ZnO glasses are presented in Table 3.10 and Table 3.11, respectively.

Table 3.10. Compositions for T2G-27a, T2G-27b, T2G-29a, and T2G-29b anion variation glasses (in mole%) as well as the mass ratio of TeO_2:PbO. Here, *m* and *M* denote ratios by mass and moles, respectively. The baseline P-series glasses for this variation study, P-8 and P-4, are listed in bold type.

Glass ID:	**P-8**	T2G-27a	T2G-27b
TeO_2	**83.22**	76.47	70.73
PbO	**16.78**	15.42	14.27
K_2O	**-**	8.11	-
KCl	**-**	-	15.00
m(TeO_2:**PbO**)	**3.55**	3.55	3.55
M(**Pb**:Te)	**0.202**	0.202	0.202
M(K:Te)	**-**	0.212	0.212
M(K:**Pb**)	**-**	1.05	1.05

Table 3.11. Compositions for T2G-29a and T2G-29b anion variation glasses (in mole%) as well as the mass ratio of TeO_2:PbO. Here, *m* and *M* denote ratios by mass and moles, respectively. The baseline P-series glasses for this variation study, P-8 and P-4, are listed in bold type.

Glass ID:	**P-4**	T2G-29a	T2G-29b
TeO_2	**69.91**	66.23	62.92
ZnO	**30.09**	28.51	27.08
K_2O	**-**	5.26	-
KCl	**-**	-	10.00
m(TeO_2:ZnO)	**4.56**	4.56	4.56
M(Zn:Te)	**0.430**	0.430	0.430
M(K:Te)	**-**	0.159	0.159
M(K:Zn)	**-**	0.369	0.369

3.3 Tellurite Crystal Fabrication

We selected twelve tellurite crystals to fabricate from the list put forth by Sakida et al., and they are listed in Table 3.12 (Sakida et al., 1999a). The list we selected included a few of the crystals from each category —see Figure 1.1. We made a few assumptions regarding the methods for fabricating these crystals based on the methods proposed by Sakida et al. because of missing details in the published methods. The assumptions and comments are as follows:

- Sakida et al. did mention that they had melted (M) the reactants in Table 3.12 at a particular temperature but they did not report the dwell time for the melt at that temperature. Therefore, we assumed the dwell time of 1 h to be sufficient for this process. Further, they either cooled the melt to room temperature (**RT**) or quenched (**QU**) it but did not report the cooling rate. In this context, we assumed that a cooling rate of 5 K/min should be sufficient.
- Sakida et al. did not list the crucible type that they used. We assumed that a platinum alloy crucible and lid would be sufficient.
- Sakida et al. added small quantities of Fe_2O_3 (0.3 mole%) to their batches to improve the NMR signal to noise ratio by shortening the relaxation times of Te nuclei with $I = ½$. We also did this.

Table 3.12. Tellurite crystals selected for fabrication at PNNL from the list proposed by Sakida et al. (Sakida et al., 1999a). Multiple steps are numbered for some of the crystals. Crystals in **bold** and *italics* show similar amorphous structure for the TeO_3-isolated and α-TeO_4 units, respectively (see Figure 3.2).* The methods listed here were those that proved successful by Sakida et al. (Sakida et al., 1999a). HT stands for heat-treatment. *Note: All crystals listed here also have an additional 0.3 mol% Fe_2O_3 added to shorten the relaxation time for the Te nuclei with I = ½ during NMR analysis.*

Type	Crystal	Starting Materials	Temp. (°C)/ HT time (hr)	Powder Diffraction File (PDF) Reference
TeO_3-isolated	**$PbTeO_3$**	TeO_2, PbO, Fe_2O_3	**(1)** 850(M)/1 → **RT** **(2)** 450(**10**) → **RT**	(Sciau et al., 1986)
	Li_2TeO_3	TeO_2, Li_2CO_3, Fe_2O_3	850(M)/1 → **RT**	(Folger, 1975b)
	$ZnTeO_3$	TeO_2, ZnO, Fe_2O_3	**(1)** 1200(M)/1 → **QU** **(2)** 650(**6**) → **RT**	(Hanke, 1967)
	$BaTeO_3$	TeO_2, $BaCO_3$, Fe_2O_3	1200(M)/1 → **RT**	(Folger, 1975a)
TeO_3-	$Cs_2Te_2O_5$	TeO_2, Cs_2CO_3, Fe_2O_3	550(M) → **RT**	(Loopstra and Goubitz, 1986)

Type	Crystal	Starting Materials	Temp. (°C)/ HT time (hr)	Powder Diffraction File (PDF) Reference
terminal	$Te_2V_2O_9$	TeO_2, V_2O_5, Fe_2O_3	**(1)** 650(M)/1 → **RT** **(2)** 430(**12**) → **RT**	(Darriet and Galy, 1973)
TeO_{3+1}	$Zn_2Te_3O_8$	TeO_2, ZnO, Fe_2O_3	**(1)** 850(M)/1 → **QU** **(2)** 650(**7**) → **RT**	(Hanke, 1966)
	$Mg_2Te_3O_8$	TeO_2, MgO, Fe_2O_3	**(1)** 1200(M)/1 → **QU** **(2)** 650(**7**) → **RT**	(Tromel and Ziethen-Reichnach, 1970)
α-TeO_4	*$SnTe_3O_8$*	TeO_2, SnO_2, Fe_2O_3	650(**85**) → **RT**	(Meunier and Galy, 1971)
	$ZrTe_3O_8$	TeO_2, ZrO_2, Fe_2O_3	650(**65**) → **RT**	(Meunier and Galy, 1971)
	$TiTe_3O_8$	TeO_2, TiO_2, Fe_2O_3	650(**85**) → **RT**	(Meunier and Galy, 1971)
β-TeO_4	$NaVTeO_5$	TeO_2, Na_2CO_3, V_2O_5, Fe_2O_3	**(1)** 600(M)/1 → **RT** **(2)** 500(**4**) → **RT**	(Darriet et al., 1972)

*Simulated patterns were generated with JADE with a 10 Å crystallite size and 0% strain
M: melting (time = 1–2 hr)
RT: room temperature with a cooling rate of 1°C/min?)
QU: quenched

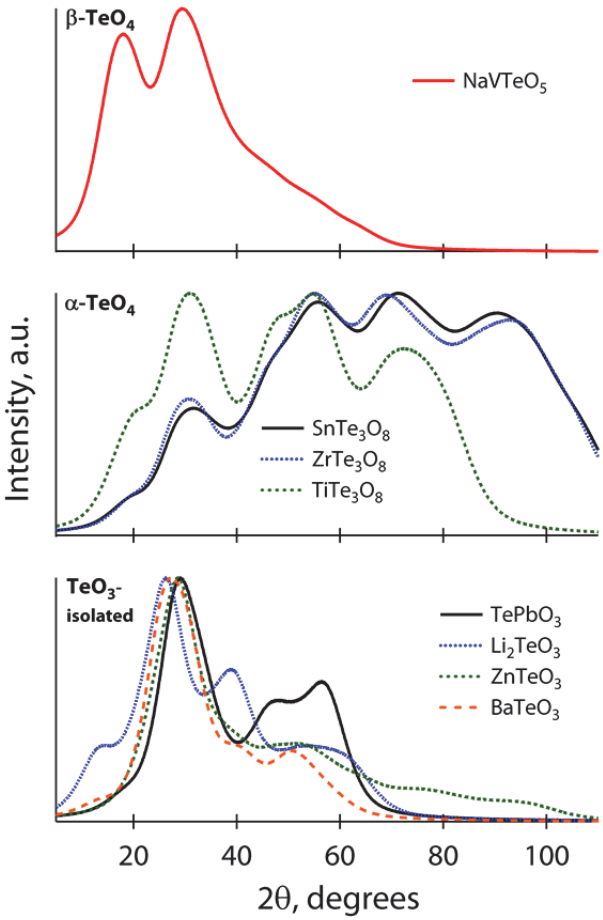

Figure 3.2. Simulated amorphous patterns of a few tellurite crystals. These patterns were generated in JADE by setting the crystallite size to 10 Å and putting 0% strain on the network.

3.4 Waste Form Characterization

3.4.1 Optical Microscopy and Photo-Documentation

Specimen microstructure was analyzed with Olympus SZH10 and Olympus PMG-3 microscopes. In some cases, a polished cross-section of the glasses was observed in reflected or transmitted light, depending on the opacity of the specimen, but most of the time, the glasses were observed as quenched. Low-magnification optical micrographs and photographs were collected of the bulk glasses, of the crucible, and of the pour plate surface after most melts for process comparisons between compositions, with a Canon T1i camera (Canon U.S.A., Inc., Lake Success, NY).

3.4.2 Helium Pycnometry – Density Measurements for Tellurite Glasses

The density of each tellurite glass for PCT measurements was measured with a Micromeritics AccuPyc II 1340 helium gas pycnometer. The pycnometer was configured to perform five purges and ten measurements during calibration and specimen analysis. The pycnometer was calibrated using a standard of known volume and the equilibrium rate was 0.0050 psig/min. Mass values were measured with an analytical balance (±0.0003 precision). For all of these measurements, the entire specimen was placed into the 10 cm^3 sample chamber—this allowed for a more representative measured density of the entire specimen.

3.4.3 Density and Porosity Measurements for High-Halide Minerals

Bulk density was measured by taking accurate mass and geometric volume measurements (average height and diameter) of the ceramic pellets before firing (green density) and after firing (sintered density). Pellet masses were measured with a PR2003 DeltaRange analytical balance (Mettler-Toledo, Inc., Columbus, OH) and volumetric measurements were taken with digital calipers with a precision of ± 0.01 mm. Efforts were made to minimize cupping of the pellets; however, some cupping was observed, leading to error in the measured fired densities with this method. Archimedes' method was used to measure density in these cases since it accommodates irregularly shaped specimens.

Archimedes' method was also performed to measure bulk density excluding open porosity of the fired pellets; this method accommodates irregularly shaped objects, so pellet cupping does not introduce error into the measurements. The specimen masses were measured dry on the PR2003 DeltaRange analytical balance and then submerged in ethanol (saturated). The temperature of the ethanol was monitored and used to calculate the bulk density, ρ_{bulk} according to Equation (1):

$$\rho_{bulk} = (m_{dry} * \rho_{EtOH}) / (m_{sat} - m_{sub}) \quad (1)$$

where m_{dry}, m_{sub}, and m_{sat}, are the masses (in g) of the specimen dry, submerged in ethanol, and saturated in ethanol, respectively, and ρ_{EtOH} is the density of ethanol ($\rho_{EtOH} = -8.54\times10^{-4}*T + 0.806$, where temperature, T, is ~ 15–25°C) (*Standard density and volumetric tables*, 1924). For measuring m_{sub}, the specimen was left submerged in the ethanol when mass was recorded on the Archimedes apparatus. For m_{sat}, the specimen was removed from ethanol, excess ethanol on the specimen surface was wiped away with a cloth and the mass was recorded on the scale without the Archimedes apparatus. Before the submerged and saturated masses were measured, the specimens were allowed to sit in ethanol under vacuum (1.3–6.7 Pa) for ~ 20 min to remove all air from open pores of the pellet. From these data, the porosity, ϕ, of the specimens was measured based both on mass differences (ϕ_m) and based on the ratio of ρ_{bulk} to the theoretical density of sodalite (2.27×10^3 kg/m^3) (ϕ_ρ) as seen in Equation 2 (Lacks and Gordon, 1993):

$$\phi_m = (m_{sat} - m_{dry}) / (m_{sat} - m_{sub}) \quad (2a)$$

$$\phi_\rho = 1 - (\rho_{bulk} / 2.27\ g/cm^3) \quad (2b)$$

3.4.4 Storage density

Measured density was then combined with the waste loading for each specimen and the storage density, ρ_S, calculated with Equation 3. Storage density (ρ_S) is defined as the mass of waste per volume of waste package, where "waste package" denotes the glass with immobilized waste.

$$\rho_S = \frac{\text{mass waste (kg)}}{\text{volume of waste package (m}^3\text{)}} \quad (3)$$

3.4.5 X-Ray Diffraction

The X-ray diffractometer (XRD) used for structure and phase analysis was a Bruker D8 Advanced equipped with a Cu Kα target set to a power level of 40 kV and 40 mA. The detector used was a position-sensitive detector with an angle range of 3° 2θ. Typical scan parameters used for specimen analysis were 5–110° 2θ for the tellurite compounds and 5–70° 2θ for the high-halide minerals with a step of 0.015° 2θ and a 0.3 second dwell at each step. JADE™ 6 and Bruker AXS© EVA and Topas 4.2 software were used to identify and quantify phase assemblages.

Specimens of both the sodalites and glasses were analyzed with XRD in powder form. These powders were generated by placing the glasses in a tungsten carbide milling chamber. For the halide minerals, pellets were ground into a fine powder and placed in the XRD to measure the crystal structure of the phases present in the waste form.

3.4.6 Raman Spectroscopy

Raman spectra were collected on *powdered* glasses with a SPEX 1877 Triplemate spectrometer (Horiba JY, Edison, NJ) equipped with a liquid nitrogen-cooled silicon charge-coupled device (CCD) detector (Princeton Instruments, Trenton, NJ) and the 514.5 nm line of a Coherent (Santa Clara, CA) Innova 307 Ar ion laser for excitation. Data were collected in backscatter geometry with a 400 μm slit with approximately 5 mW of laser power at the specimen and a 100 s acquisition time. The estimated uncertainty of the peak frequencies was ±1 cm^{-1} for all of the Raman spectra.

Quantitative spectral analysis and curve fitting of the Raman data was performed using Thermo Fisher Scientific (Waltham, MA) Grams/32 AI software, which uses the Levenburg-Marquardt nonlinear peak fitting method (Levenberg, 1944). Prior to curve fitting, a decaying exponential baseline correction was used to remove the background due to Rayleigh scattering. The remaining spectrum in the 300–1500 cm^{-1} region was fitted, giving results with $R^2 \geq 0.998$.

Several protocols were considered for quantitative fitting of the Raman spectra. First, peak fitting was performed with no constraints and trends compared. This seemed to work satisfactorily with the compositional variation study glasses where a series of bands were identified and coordinated with literature values. However, for the lead-tellurite and structural variation study glasses, this method was deemed unsatisfactory, so a subsequent set of fits were performed with "fixed" wavenumber positions determined from the optimum positions for the TPb_0 glass for the main Raman bands in that glass. The frequencies, assignments, and literature references for these bands are shown in Table 3.13. The fixed frequency approach yielded R^2 fit values better than 0.999. For the purposes of analysis, ratios of peak areas were compared as a function of XCl_{20}-loading or Cl/O ratio. For the P-series glasses, the Raman fitting was performed with no fixed parameters, and the peak frequencies of the bands were allowed to float as well as the widths as opposed to fixing the frequencies and just allowing the widths to float, as we did subsequently. As mentioned above, the latter method with fixed frequencies appeared to result in more consistent results when the $TPb_{\#}$ glasses were analyzed as a function of composition change. The fixed Raman frequency bands that we used for quantitative analysis of the $TPb_{\#}$ glasses are presented in Table 3.13 where the "**E1**/**E2**" bands were combined into "**E**" for the compositional variation study but were deconvoluted into **E1** and **E2** for the rest of the glasses.

In order to determine the structural differences between the two phases present in the 15% $X\text{Cl}_{20}$-loaded glass, both macro- and micro-Raman spectra were collected on each phase from this bulk piece. Raman spectra were obtained with the same spectrometer and laser (514.5 nm) as used in the macro measurements. However, the laser beam was coupled to a confocal Olympus BH2 microscope (Center Valley, PA) equipped with an 80× objective and numerical aperture equal to 0.75. Laser power at the specimen was approximately 10 mW. The slit width was 400 μm and the exposure time was 100 s for all specimens.

Table 3.13. Raman band assignments for tellurite glasses. Here, "*tbp*" denotes trigonal bipyramidal TeO_4 units, "*tp*" denotes trigonal pyramidal TeO_3 units, "NBO" denotes a non-bridging oxygen, LFE denotes the low-frequency ($\tilde{\nu}$) envelope, and HFE denotes the high-frequency envelope. The "Fitted" column denotes the peak locations for the fixed-frequency fitting technique that we used to fit the lead-tellurite and structural variations study glasses. The "**E1**" and "**E2**" bands were split from the "**E**" band for the lead tellurite and structural variation study glasses. The bands listed below "**E2**" are bands that were unique to a particular family of glasses and remain without a particular band name assignment due to their unique occurrences.

Band	Range ($\tilde{\nu}$), cm^{-1}		Group	Glasses present	Interpretation	References
	Literature	Fitted				
A	770–780	769.7	HFE	All	Te-O^- and Te=O stretch in TeO_3 and deformed TeO_{3+1} *tp*	(Chowdari and Kumari, 1999; Mazzuca et al., 1995; Murugan et al., 2006)
B	700–760	710.9	HFE	$TPb_{\#}$ series, P-8 "Pb", P-11 "Pb+Cl"	Te-O^- and Te=O stretch in TeO_3 and TeO_{3+1} *tp*	(Chowdari and Kumari, 1999; Mazzuca et al., 1995; Murugan et al., 2006; Duverger et al., 1997)
C	645–670	648.0	HFE	All	Te-O asymmetric stretch in TeO_4 *tbp*, does not vary with type or amount of modifier; may have contribution from TeO_{3+1}	(Chowdari and Kumari, 1999; Murugan et al., 2006; Sekiya et al., 1992b)
D	595–615	596.5	HFE	$TPb_{\#}$ series, P-5 "P", P-14 "P+Cl", P-8 "Pb", P-11 "Pb+Cl"	Te-O asymmetric stretch in TeO_4 *tbp*	(Chowdari and Kumari, 1999; Mazzuca et al., 1995; Murugan et al., 2006)
E1	400–500	432.7	LFE	All	Te-O-Te symmetric bend in vertex sharing polyhedral	(Chowdari and Kumari, 1999; Murugan et al., 2006; Sekiya et al., 1992b)
E2	400–500	476.0	LFE	$TPb_{\#}$ series	Te-O-Te symmetric bend in vertex sharing polyhedral; Te-O-Te chains in 4-coordinated TeO_4 *tbp*	(Chowdari and Kumari, 1999; Murugan et al., 2006; Sekiya et al., 1992b; Tatar et al., 2010)
-	355			P-9 "W", P-12 "W+Cl"	Deformation vibrations of WO_6	(Sekiya et al., 1994a; Chowdari and Kumari, 1999)
-	840–860			P-9 "W", P-12 "W+Cl"	Stretch of W-O associated with WO_6 with no W=O or asymmetric stretch of WO_4 having W=O	(Sekiya et al., 1994a; Chowdari and Kumari, 1999)
-	820–850			P-7 "Al/B", P-2 "Al/B+Cl"	B-O-B stretch, pyroborate; 2 NBO per B(III)	(Brow et al., 1997; Li et al., 2003)
-	925–940			P-9 "W",	Stretch of W=O or possibly W-O^- located at	(Sekiya et al., 1994a; Chowdari

Band	Range ($\tilde{\nu}$), cm^{-1} Literature	Fitted	Group	Glasses present	Interpretation	References
				P-12 "W+Cl"	the edge of W clusters	and Kumari, 1999)
-	1040–1050			P-5 "P", P-14 "P+Cl",	PO_4 tetrahedra with one bridging oxygen Q^1	(Murugan et al., 2006; Chowdari and Kumari, 1999)
-	1200–1300			P-7 "Al/B"	Pyroborates [2 NBO per B(III)] or Al(IV) substituting for B(IV) in borate network	(Brow et al., 1997; Li et al., 2003)

3.4.7 Chemical Durability

The chemical durability test performed was the PCT, a seven-day static leaching test in deionized water at 90°C (*Standard Test Methods for Determining Chemical Durability of Nuclear, Hazardous, and Mixed Waste Glasses and Multiphase Glass Ceramics: The Product Consistency Test (PCT)* ASTM C 1285-08, 2002). The PCT was performed on each of the glasses according to Test Method B (PCT-B) of the ASTM International Standard C 1285-02. The chemical durability is characterized quantitatively by the normalized sodium release (NL_{Na}, in g/m^2), being higher for less chemically durable glasses. Detailed methods and results were described in the FY2010 report (Riley et al., 2010).

3.4.8 Thermal Analysis

The P-series lead-tellurite glasses were analyzed with a TA Instruments SDT Q600 (New Castle, DE) differential thermal-thermogravimetric analyzer (DTA-TGA). Here, specimens were run at various ramp rates (e.g., 10°C, 15°C) to determine the effect of ramp rate on the glass transition temperature (T_g), onset crystallization temperature (T_x), crystallization temperature (T_c), and T_M.

Differential scanning calorimetry (DSC) and TGA were performed on the powder of each glass from the lead tellurite series with a Jupiter® STA 449C (NETZSCH Instruments N.A. LLC, Burlington, MA). For the DSC/TGA experiments, specimens were loaded into alumina (Al_2O_3) pans, without lids, placed onto a DSC(/TG) High RG4 sample carrier, and heated at 10°C/min from room temperature (~25°C) to 750°C with air as the carrier gas at a flow rate of 50 mL/min. The spectra were analyzed with Proteus® software (v 5.3.0 /24.05.2011, NETZSCH).

The DTA and DSC results were analyzed and the glass-formation ability (K_{gl}) was calculated according to the Hruby criterion—see Equation 4—where T_M is the melting temperature of the glass (Hruby, 1972).

$$K_{gl} = (T_c - T_g) / (T_M - T_g) \quad (4)$$

Since the DSC data at temperatures above 500°C did not appear reliable, the T_M could not be determined, accurately. Thus, we used a modified version of the Hruby criterion, presented by Wang et al., to compare the glass-formation ability with only the numerator from Equation 4, $T_c - T_g$ (Wang et al., 1994). This difference provides an estimate of how difficult it would be to quench from a melt and prevent crystallization before reaching the T_g.

Additionally, thermal diffusivity was measured for P-11 and Sodalite S5A with a NETZSCH Laser Flash Apparatus 457 (LFA), (NETZSCH Instruments North America, LLC, Burlington, MA). For the sodalites, powders of Sodalite 5A were pressed into a pellet, and fired at 850°C. Then, 12.5 mm discs were core-drilled out of the pellets that were ~2-mm thick. These were coated with Graphit®, provided by NETZSCH, which was applied to help make sure that all of the LFA laser energy was absorbed at the front face of the specimen. Measurements were made on both specimens at room temperature, and then every 100°C between 100°C and 700°C.

After some trial and error trying to make the tellurite glasses into discs for thermal diffusivity measurements, we found that the easiest method was to pour-cast the glasses into fused silica casts at the T_M. Thus, the glasses were melted, poured into cylindrical quartz molds and annealed at 240°C for 4 hours, after which the annealing furnace was allowed to air-cool to room temperature. These cylinders (Figure 3.3) were then cut into discs with a wire saw and polished to a thickness of ~2–3 mm. The most pristine and intact disc of P-11 was coated with Graphit® and loaded into the instrument. Measurements were made at 20°C and then in 50°C increments from 50°C to 250°C, terminating near the glass transition temperature, T_g, of the material. Five data points were collected at each temperature and averaged.

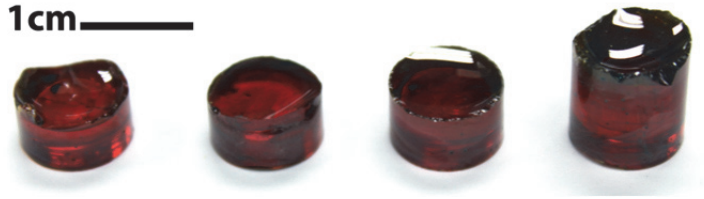

Figure 3.3. Cast cylinders of P-11 glass from which discs were cut for the thermal diffusivity measurements.

3.4.9 Scanning Electron Microscopy – Energy Dispersive Spectroscopy

Specimens were observed in greater detail with scanning electron microscopy (SEM) and energy dispersive spectroscopy (EDS). Two different SEMs were used and included a JSM-5900 with a tungsten filament and a JSM-7001F with a field emission gun (JEOL, Ltd., Tokyo, Japan). For both of these systems, an EDAX Apollo II 30 mm^2 Si-drifted EDS detector (AMETEK, Berwyn, PA) was used for compositional analysis. Samples were analyzed coated with palladium on the JSM-5900 and samples were analyzed uncoated on the JSM-7001F

4 RESULTS & DISCUSSION

4.1 Halide Minerals

4.1.1 Halide Minerals: X-Ray Diffraction

The sodalite pellets that we made in FY2010 without sintering aids showed moderate sodalite concentrations of ~ 60 mass%, mostly independent of the firing temperature (Figure 4.1). However, we were able to increase these values with some modifications to the process that included the addition of NBS-1, a glass sintering aid, and component substitutions for the CS.

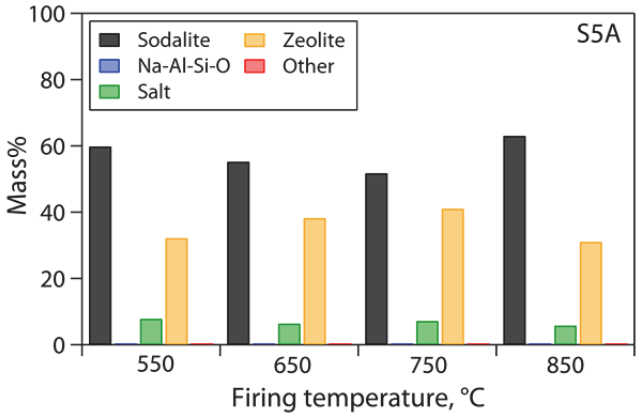

Figure 4.1. Summary of phase distribution in S5A samples at different firing temperatures. The bars progress from sodalite at the far left to "other phases" at the far right.

Figure 4.2 provides a comparison between the as-made, unfired and dried gel of Sodalite S5 series made with CS in FY2010 (S5A), S5C made with TEOS in FY2011, and S5D made with Ge-EtO in FY2011. Here, it is obvious that these slight modifications to the process resulted in widely different phase distributions. The unfired S5A specimen had a very small fraction of sodalite at 24% but was increased to 76 mass% in a separate sample that was dried at 90°C for 5 days. The S5C specimen had a very large sodalite fraction (96%) with the S5D specimen not much lower (82%). This suggests that an organic form of the Group IV component may be the preferred precursor to achieve a large sodalite fraction in the as-made gel. Also, with the organic precursors, the fraction of unreacted salt was reduced.

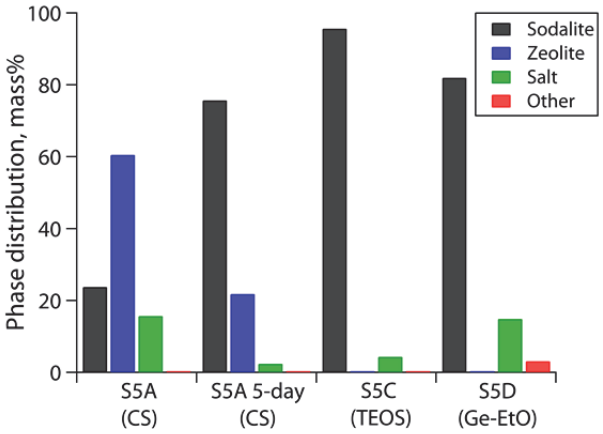

Figure 4.2. Summary of phase distribution in the S5A, S5A after drying for 5-days at 90°C, S5C, and S5D formulations as-made (unfired). The bars progress from sodalite at the far left to "other phases" at the far right.

Figure 4.3 provides a comparison summary of the phase distribution in pellets made with different sintering aids and fired at different temperatures. All of the SA-### sintering aids behaved similarly with a maximum sodalite concentration at the lower sintering temperatures (550–600°C) and an inverse correlation between the sodalite and Na-Al-Si-O phase concentrations with increasing firing temperatures. This is likely due to chloride volatility with increased firing temperatures. This inverse relationship was similarly observed with S5C-TePbO and S5C-NBS1 but was highly exaggerated with S5C-NaAlP.

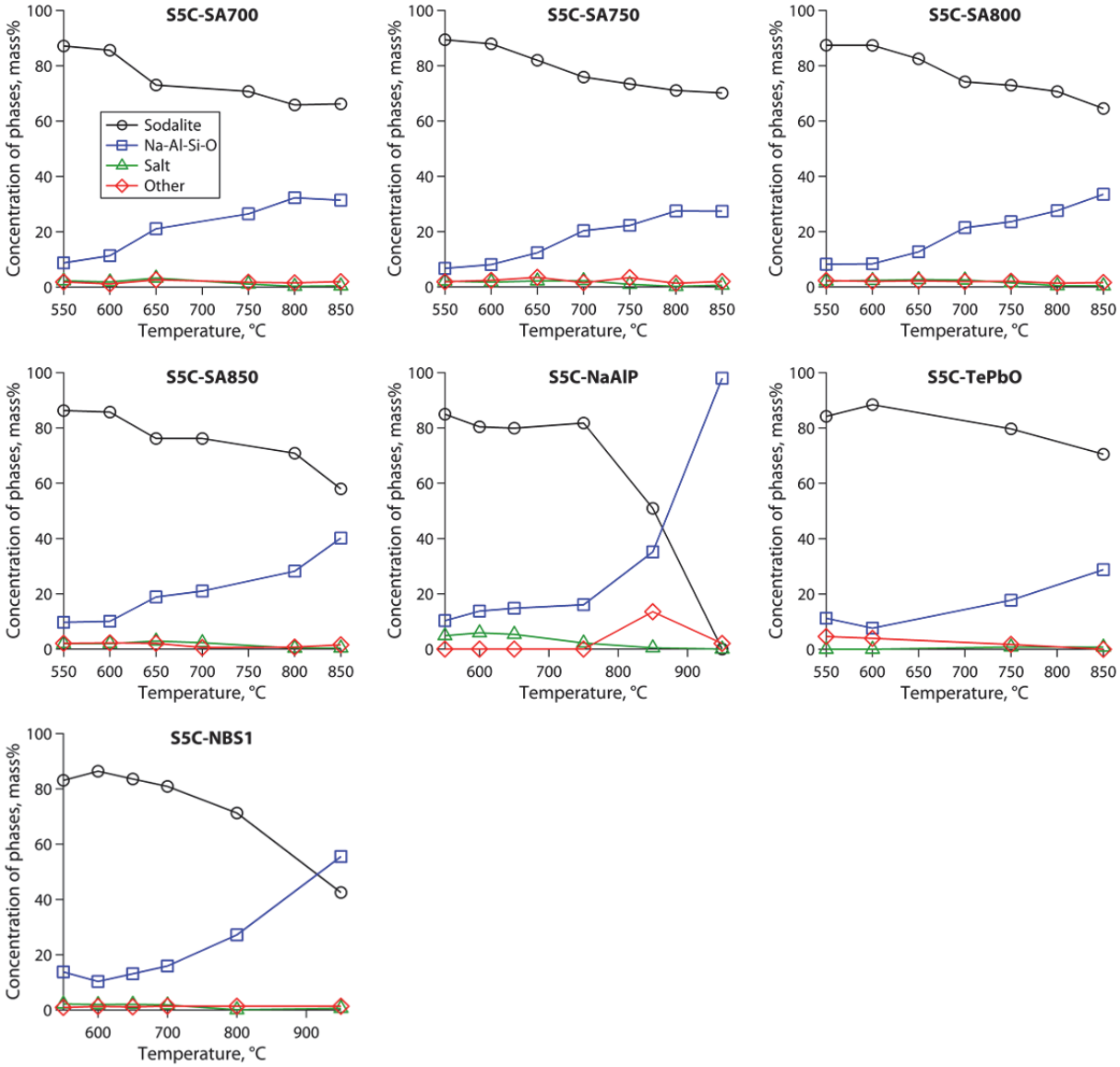

Figure 4.3. Phase distribution for the various S5C formulations at fired at different temperatures. The legend presented in the upper left figure is valid for all figure parts.

All of the crystalline phases used for the Rietveld refinement of the sodalite specimens are summarized in Table 4.1. These phases are similar to those found with the CS-based sodalites we made in FY2010, although in some cases alternative phases were found for the sodalite and Na-Al-Si-O structural fits. More information on the exact phases found for each specimen and the actual Rietveld refinement patterns are presented in Appendix B.

Table 4.1. Summary of phases identified in the halide minerals. The table shows powder diffraction file (PDF) and/or International Crystal Structure Database (ICSD) identifications, the space group (SG), the space group number (SG#), and references for the patterns. More details can be found in Appendix B.

Phase ID	Category	PDF#	ICSD#	SG (SG#)	Reference
Cancrinite	Cancrinite	83-1183	80298	*P*3 (143)	(Lindner et al., 1995)
Sodalite	Sodalite	37-0476	41188	*P*-43*n* (218)	(Beagley et al., 1982)
Hydrosodalite	Sodalite	75-5343	413502	*P*-43*n* (218)	(Kendrick and Dann, 2004)
Ge-sodalite	Sodalite	79-0711	65664	*P*-43*n* (218)	(Fleet, 1989)
Carnegieite low	NaAlSiO	44-1496	73511	*Pb*21*a* (29)	(Withers and Thompson, 1993)
Nepheline	NaAlSiO	76-2465	37354	*P*63 (173)	(Foreman and Peacor, 1970)
$Na_{1.55}Al_{1.55}Si_{0.45}O_4$	NaAlSiO	49-0006	280473	*Pbca* (61)	(Thompson et al., 1998)
Analcime 1Q	NaAlSiO	73-6448	34058	*I*41/*ACDZ*	(Meier, 1973)
Sylvite (KCl)	Salt	41-1476	28938	*Fm*3*m* (225)	(Barrett and Wallace, 1954)
LiCl	Salt	74-1972	27981	*Fm*3*m* (225)	(Ott, 1923)
Halite (NaCl)	Salt	05-0628	28948	*Fm*3*m* (225)	(Barrett and Wallace, 1954)
Li_2SiO_3	Other	83-1517	100402	*Cmc* (21)	(Seemann, 1956); (Hesse, 1977)
$Y_6Cl_{10}(Si_4O_{12})$	Other	70-8429	94464	*C*2/*m* (12)	(Hartenbach and Schleid, 2001)

4.1.2 Halide Minerals: Pellet Densities and Porosity

The full data set for density and porosity measurements on the alternative sintering aids is presented in Table 4.2, with a graphical representation in Figure 4.4. It should be noted that the S5C-NBS1sample is a S5C sample made in FY2011 with TEOS. Here, we see that the maximum density with the NBS-1 glass sintering aid was 86% of theoretical (2.27×10^3 kg/m^3) at 750°C. With the new sintering aids, we were able to achieve densities of up to 96% of theoretical. The optimum heat-treatment temperature to achieve maximum density for the SA-### sintering aids was 750°C for most of the specimens, with the exception of SA-750. The NaAlP-B4 and TePbO and sintering aids did not help densify the pellets; even at 850°C firing temperatures the densities were still < 60% of theoretical density at 55% and 57%, respectively. This suggests that these sintering aid compositions were not as reactive with the mineral components as the SA-### and NBS-1 sintering aids.

Also shown in Figure 4.4 is a comparison of the density and sodalite mass% for each sintering aid at the 750°C firing temperature, the most efficient firing temperature for densification in the SA-### samples. From this plot, it is evident that the SA-### sintering aids did a good job at closing the pores and allowing a good amount of sodalite to form during firing. However, at this temperature, the SA-### sintering aids are not much more efficient than the NBS-1 glass. Also, the effect of increased viscosity for NBS-1 over the SA-### sintering aids is evident by the high porosity for S5C-NBS1 at temperatures ≤ 750°C.

Table 4.2. Measured bulk density (ρ_B), porosity, and % of theoretical density of pure sodalite (2.27×10^3 kg/m^3) for 5 mass% additions of various sintering aids to S5C series (TEOS-based) sodalite specimens at different firing temperatures. The heat-treatment temperatures resulting in the maximum density are shown in bold type.

Specimen ID	Firing Temperature, °C	ρ_B, ($\times10^3$ kg/m^3)	% Porosity	% Theortical density
S5C-NBS1	550	1.059	56%	47%
	600	1.090	55%	48%
	650	1.198	51%	53%
	750	**1.959**	**21%**	**86%**
S5C-SA700	550	1.247	49%	55%
	600	1.584	34%	70%
	650	2.104	13%	93%
	750	**2.180**	**11%**	**96%**
	850	2.131	14%	94%
S5C-SA750	550	1.165	51%	51%
	600	1.316	45%	58%
	650	1.564	35%	69%
	750	2.026	18%	89%
	850	**2.060**	**16%**	**91%**
S5C-SA800	550	1.077	56%	47%
	600	1.264	48%	56%
	650	1.757	27%	77%
	750	**2.145**	**12%**	**95%**
	850	2.027	18%	89%
S5C-SA850	550	1.067	56%	47%
	600	1.350	44%	59%
	650	1.832	24%	81%
	750	**2.100**	**15%**	**92%**
	850	1.910	23%	84%
S5C-NaAlP	550	1.061	55%	47%
	600	1.069	55%	47%
	650	1.005	58%	44%
	750	1.259	48%	55%
	850	**1.251**	**50%**	**55%**
S5C-TePbO	550	1.015	59%	45%
	600	1.033	58%	45%
	650	1.008	60%	44%
	750	1.230	52%	54%
	850	**1.296**	**51%**	**57%**

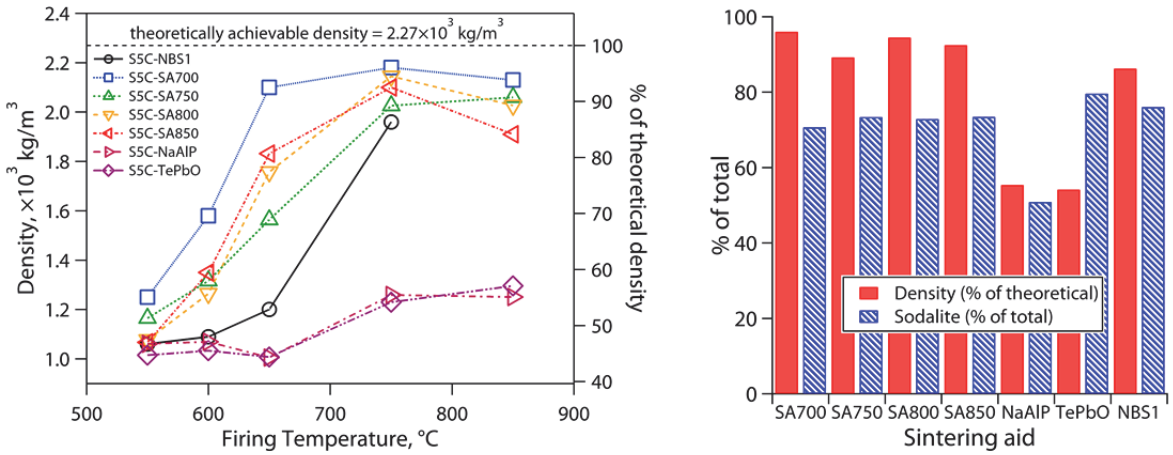

Figure 4.4. (left) Summary of the pellet density as a function of firing temperature for S5C series specimens made with an additional 5 mass% of various sintering aids (see Table 3.3 for more details). (right) Column chart comparing the mass% of sodalite in each specimen with the density (% of theoretical) for all S5C samples fired at 750°C.

The germania-based sodalite sample, S5D, was pressed and fired at 750°C. The open porosity was so high (>40%) that this was abandoned without further investigation. However, this approach of including germania-based precursors or sintering aids could be considered in the future.

4.1.3 Halide Minerals: Thermal Properties

The thermal diffusivity of the Sodalite 5A pellets was quantified with NETZSCH LFA 457 on pellets (see Table 2.3 for the composition). The results from these measurements are presented in Figure 4.10a. These results show that the thermal diffusivity of the S5A specimens ranged from 0.17–0.40×10^{-6} m^2/s with a maximum value at the lower temperature and a steady decrease with increasing temperature. The values are presented in Figure 4.5.

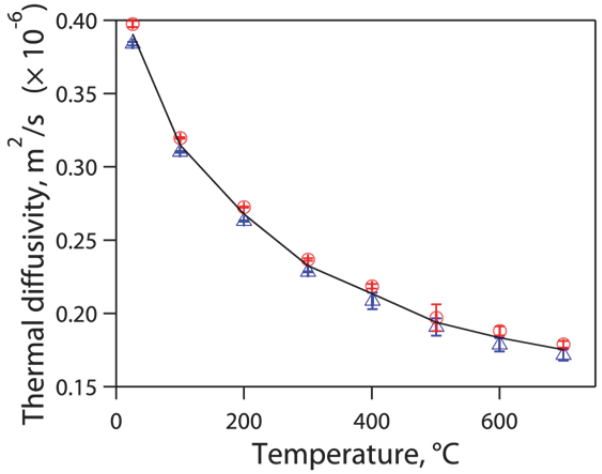

Figure 4.5. Thermal diffusivity of Sodalite 5A pellets. Error bars for the measured thermal diffusivity are included on the data points.

4.2 Tellurite Glasses

4.2.1 Tellurite Glasses: Compositional Variation Study

4.2.1.1 X-Ray Diffraction

To recap from our FY2010 report, before the PCT, all ten "P-series" tellurite glasses were determined by XRD to be bulk amorphous; in other words, if crystallinity was present in some of the glasses it was below the detection limit of the instrument (Riley et al., 2010). Figure 4.6 provides fitted backgrounds for the amorphous pre-PCT XRD spectra, which help reveal the subtle differences in peak location and intensity. The PbO glasses had the tallest and narrowest amorphous humps, suggesting that they were the most "structured" of this glass set.

Simulated amorphous diffraction patterns were generated for the different α-TeO_4 and β-TeO_4 PDF patterns in the ICSD that matched diffraction peaks for the various glasses with Jade 6 software with a set crystallite size of 10 nm and 0% strain (see Table 4.3). The three simulated patterns differed in amorphous hump location and intensity as seen in the bottom portion of Figure 4.6. When observing Figure 4.6 (primarily the low-2θ hump) with the vertical guides as a reference, it is apparent that some of the glasses seem to fit the simulated orthorhombic β-TeO_4 phase (PDF# 74-1131, Table 4.3), such as the Al_2O_3/B_2O_3-containing glasses (P-7 "Al/B" and P-2 "Al/B+Cl"), while the other glasses seemed to fit with the tetragonal α-TeO_4 phases (PDF#s 42-1365 and 78-1713, Table 4.3).

A summary of the XRD results for the ten glasses after the PCT is shown in Figure 4.6b with the best-fit structures presented in Table 4.3. Diffraction peaks matching $Pb_2Te_3O_7$ crystals were observed in P-8 "Pb" and P-11 "Pb+Cl" glasses after the PCT, although quantities were close to the detection limit for P-11. For the tungstate glasses, only P-12 "W+Cl" crystallized (to Ba_3WO_6) after the PCT. The other three families, the Al_2O_3/B_2O_3 (P-7 and P-2)-, ZnO (P-4 and P-13)-, and P_2O_5 (P-14 and P-5)-containing glasses all had characteristically different behavior with and without added XCl_{20}. Without XCl_{20}, all formed some α-TeO_4 (tetragonal paratellurite), while the Zn glass (P-4) also formed some $Zn_2Te_3O_8$. After adding XCl_{20}, all formed some β-TeO_4 (orthorhombic tellurite), while Al/B+Cl (P-2) also formed some $Na_2Te_2O_7$, and Zn+Cl (P-13) formed some $Zn_2Te_3O_8$.

It should be noted that of the glasses that showed crystalline TeO_2 phases after the PCT (i.e., P-7 "Al/B," P-2 "Al/B+Cl", P-5 "P", P-14 "P+Cl", P-4 "Zn", and P-13 "Zn+Cl"), those containing XCl_{20} always formed β-TeO_4, whereas those without XCl_{20} always formed α-TeO_4. This demonstrates that mixed-chloride additions to the tellurite glass network affected the structure of the network in a consistent way. It seems that adding XCl_{20}, or perhaps the alkali and lanthanides with the chlorides, favors the formation of β-TeO_4 structures in these systems.

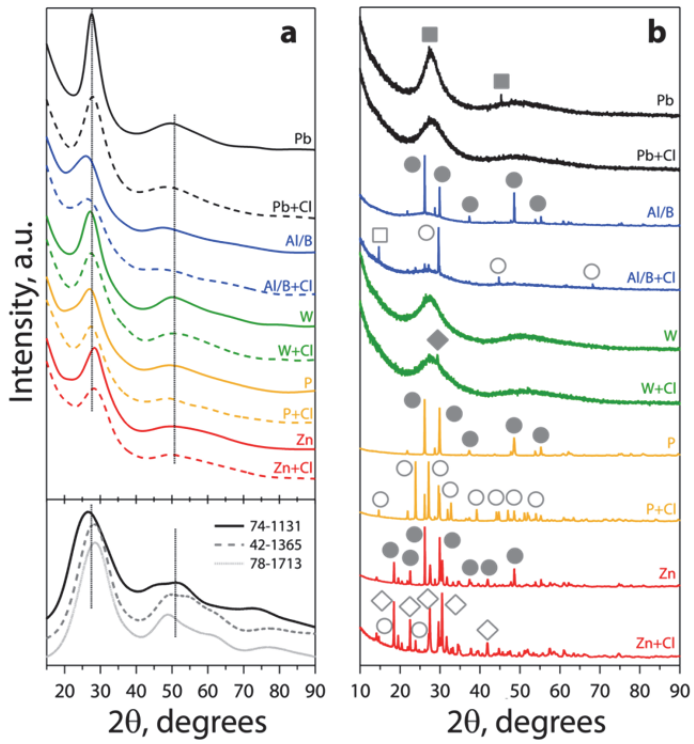

Figure 4.6. **(a)** XRD summary plot showing the amorphous background fits for all glasses before PCT for comparison with three amorphous simulated patterns for TeO_4 PDF structures (74-1131, 42-1365, and 78-1713; see Table 4.3). Vertical lines are added as a visual guide for the location of the primary amorphous humps. The spectra are vertically offset (intensities retained) to accentuate the differences so the vertical scale is listed in arbitrary units (a.u.). **(b)** XRD spectra for all 10 glasses after PCT. Best-fit diffraction peaks were identified and are denoted by symbols near the most intense of the diffraction peaks for each phase observed for each glass. Here, ● denotes tetragonal α-TeO_4, ○ denotes orthorhombic β-TeO_4, ■ denotes $Pb_2Te_3O_7$, □ denotes $Na_2Te_2O_7$, ◆ denotes Ba_3WO_6, and ◇ denotes $Zn_2Te_3O_8$. This figure was recreated from our previous work (Riley et al., 2010).

Table 4.3. Summary of phases identified in the tellurite glasses for the composition-variation study.

Phase ID	PDF#	ICSD#	SG (SG#)	Reference	Glasses
α-TeO_4	78-1713	62897	*P*43212 (96)	(Kondratyuk et al., 1987)	P-4 "Zn", P-7 "Al/B"
α-TeO_4	42-1365	27515	*P*41212 (92)	[a]	P-5 "P"
β-TeO_4	74-1131	26844	*Pbca* (61)	(Beyer, 1967)	P-2 "Al/B+Cl", P-14 "P+Cl", P-13 "Zn+Cl"
$Pb_2Te_3O_7$	43-0549	N/A	*Fm*-3*m* (225)	(Kulcu, 1987)	P-8 "Pb", P-11 "Pb+Cl"
$Na_2Te_2O_7$	35-1263	N/A	*Imm*2 (44)	(Knop and Demazeau, 1981)	P-2 "Al/B+Cl"
Ba_3WO_6	33-0182	N/A	*Fm*-3*m* (225)	[b]	W-12 "W+Cl"
$Zn_2Te_3O_8$	89-4454	50705	*C*2/*c* (15)	(Feger et al., 1999)	P-13 "Zn+Cl"

[a] Blanchard, F., Department of Geology, University of Florida, Gainesville (1990).

[b] National Bureau of Standards (U.S.) Monogr. 25, **19**, p 21 (1982).
N/A: not applicable

4.2.1.2 Raman Spectroscopy

Figure 4.7 shows example results for the Raman curve fitting for the lead-tellurite "P-series" glasses. Assignments for tellurite bands **A** through **E** have been made according to Table 3.13 with structural

representations of these units presented in Figure 2.1 derived from the literature. Raman spectra for the specimens with and without XCl_{20} are shown in Figure 4.8. Peak wavenumbers ($\tilde{\nu}$) and areal intensity determined from the fitting are shown in Table 4.4. In all cases except the PbO-containing glasses (P-8 "Pb" and P-11 "Pb+Cl"), **A** and **B** bands assigned to TeO_3 and TeO_{3+1} *tp* groups could not be distinguished, so they were assigned to **A**, the higher frequency band. In only two cases, P_2O_5-containing and PbO-containing glasses, could a **D** band, assigned to Te-O asymmetric stretch in TeO_4, be distinguished. A summary of peak fitting for the different glass systems is presented below.

- **PbO-glasses** (P-8 "Pb" and P-11 "Pb+Cl"). Fitting all of the tellurite bands **A** (*tp*), **B** (*tp*), **C** (*tbp*), **D** (*tbp*), and **E** (Te-O-Te) was required.
- **Al_2O_3/B_2O_3-glasses** (P-7 "Al/B" and P-2 "Al/B+Cl"). Spectra were fitted with **A** (*tp*), **C** (*tbp*), and **E** (Te-O-Te) tellurite bands. Additional bands were observed at ~840 cm^{-1} and, in the case without chlorides, at ~1300 cm^{-1}. Both of the aforementioned bands were assigned to B-O-B(III) in pyroborate structures, though the latter band has been also applied to Al(IV) substituting for B(IV) in the borate network (Brow et al., 1997; Li et al., 2003).
- **WO_3-glasses** (P-9 "W" and P-12 "W+Cl"). The fit of current data incorporated tellurite bands **A** (*tp*), **C** (*tbp*), and **E** (Te-O-Te). In addition, another band was observed in the **E** envelope (408–412 cm^{-1}) distinct from the ~360 cm^{-1} band, which is also visible in the spectra (Figure 4.8c) and previously assigned to deformation vibrations of WO_6 (Sekiya et al., 1994a; Chowdari and Kumari, 1999). In the fitting procedure, the three apparent bands in the 300–600 cm^{-1} region were fit with only two bands as shown in Table 4.4. Bands ~860 and ~930 cm^{-1} were assigned to W-O stretches internal and external to the clusters, respectively (see Table 3.13).
- **P_2O_5-glasses** (P-5 "P" and P-14 "P+Cl"). Glasses in the current study were fit with six Raman bands, including four of the tellurite bands: **A** (*tp*), **C** (*tbp*), **D** (*tbp*), and **E**. Raman fitting required two peaks in the envelope of the **E** peak assigned to the Te-O-Te bending vibrations (see Table 3.13). Normally the P-O-P bending vibrations are at lower wavenumbers, i.e., $\tilde{\nu}$ < 300 cm^{-1}, but it is possible that some band mixing occurred to cause the asymmetry in this first peak. One or two weak peaks around 1000 cm^{-1} can be ascribed to PO_4 groups with one or two non-bridging oxygens.
- **ZnO-glasses** (P-4 "Zn" and P-13 "Zn+Cl"). Spectra in the current study were adequately fit with only three tellurite bands: **A** (*tp*), **C** (*tbp*), and **E** (Te-O-Te bending).

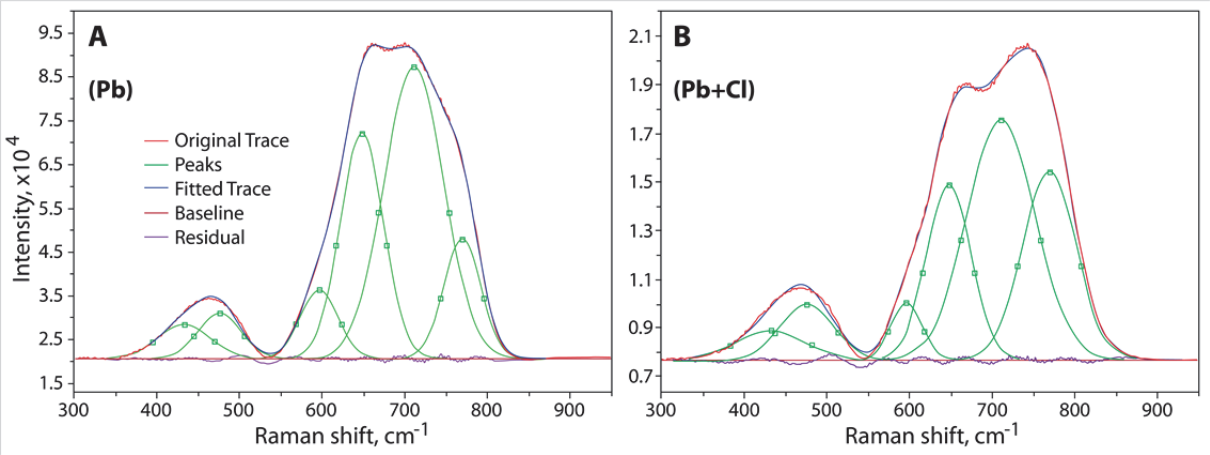

Figure 4.7. Examples of curve fitting for (A) Pb (P-8) and (B) Pb+Cl (P-11) glasses.

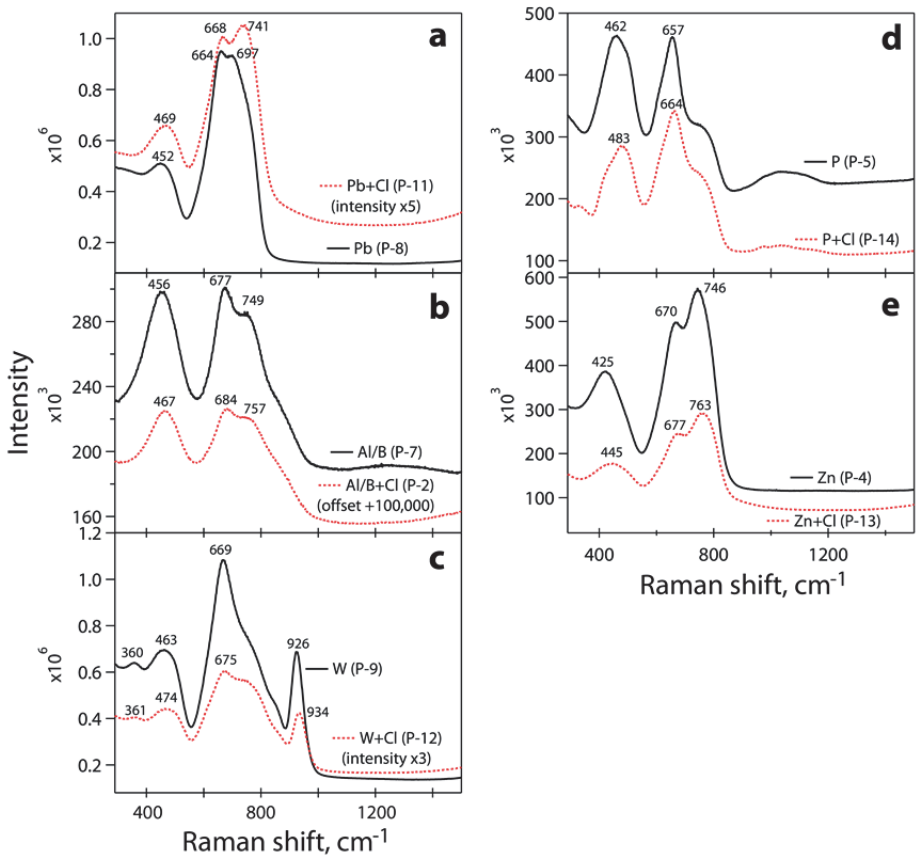

Figure 4.8. Raw Raman spectra without backgrounds removed for glasses with and without XCl_{20} (listed as "Cl"). Spectra are not offset but are shown as collected unless otherwise noted. (**a**) PbO-glasses P-8 (bottom, black) and P-11 (top, red, intensity 5× from measured); (**b**) Al_2O_3/B_2O_3-glasses P-7 (top, black) and P-2 (bottom, red, offset +100,000 counts); (**c**) WO_3-glasses P-9 (top, black) and P-12 (bottom, red, intensity 3× from measured); (**d**) P_2O_5-glasses P-5 (top, black) and P-14 (bottom, red); and (**e**) ZnO-glasses P-4 (top, black) and P-13 (bottom, red).

Table 4.4. Results of quantitative fitting of Raman bands on P-series glasses. This table consists of peak location in wavenumber ($\tilde{\nu}$, ±1 cm^{-1}) and integrated intensity, *I*. Note that these glasses were fitted with peak frequencies allowed to float (not fixed).

Glass ID	Composition	R^2 of fit	**A**		**B**		**C**		**D**		**E**		other	
			$\tilde{\nu}$	*I*	$\tilde{\nu}$	*I*	$\tilde{\nu}$	*I*	$\tilde{\nu}$	*I*	$\tilde{\nu}$	*I*	$\tilde{\nu}$	*I*
P-8	Pb	0.9998	770	1.55E+07	711	6.03E+07	648	3.40E+07	597	9.10E+06	476	6.21E+06	433	6.27E+06
P-11	Pb+Cl	0.9996	770	6.36E+06	711	1.01E+07	648	4.87E+06	597	1.15E+06	476	1.90E+06	433	1.33E+06
P-7	Al/B	0.9990	764	4.53E+06	-	-	676	9.72E+06	-	-	457	1.10E+07	843	4.78E+06
													1295	1.38E+06
P-2	Al/B+Cl	0.9993	774	1.83E+06	-	-	686	6.99E+06	-	-	468	5.24E+06	846	3.74E+06
P-9	W	0.9974	765	6.06E+07	-	-	662	6.66E+07	-	-	481	1.73E+07	412	1.24E+07
													856	5.50E+06
													927	2.65E+07
P-12	W+Cl	0.9984	762	1.55E+07	-	-	657	8.29E+06	-	-	483	2.89E+06	408	1.52E+06
													868	5.47E+05
													935	4.02E+06
P-5	P	0.9984	756	9.83E+06	-	-	655	1.50E+07	559	3.23E+06	447	1.50E+07	505	7.14E+06
													1046	5.58E+06
P-14	P+Cl	0.9993	756	1.20E+07	-	-	661	1.81E+07	598	3.57E+06	418	2.38E+06	484	1.44E+07
													1042	4.53E+06
P-4	Zn	0.9987	757	4.27E+07	-	-	659	2.88E+07	-	-	430	1.70E+07	-	-
P-13	Zn+Cl	0.9987	770	1.89E+07	-	-	669	1.28E+07	-	-	447	5.42E+06	-	

As a rough estimate of the fraction of *tp* units as compared to *tbp* units (TeO_3/TeO_4) in the glass, areal intensity ratios were taken from the fitted spectra of the intensity of the **A** band to that of the **C** band, i.e., *I*(**A** band)/*I*(**C** band) (Chowdari and Kumari, 1999; Himei et al., 1994). These corresponding ratios are shown in Table 4.5. It should be noted that these ratios seem to imply similar Raman cross-sections between the various bands, which might not necessarily be the case. Because it was not always clear whether the bands in the region (i.e., 720–780 cm^{-1}) should be assigned to **A** or **B**, the intensity ratio of **A** + **B** to the **C** band, i.e., *I*(**A** + **B** bands)/*I*(**C** band), was also analyzed. Only the data for the PbO-containing glasses P-8 (Pb) and P-11 (Pb+Cl) were influenced by this approach.

Table 4.5. Ratios of key tellurite peaks from the Raman data. Since "**B**" was only observed in the Pb-containing glasses, the ratio *I*(**A** + **B**)/*I*(**C**) is only different from *I*(**A**)/*I*(**C**) for these glasses.

Glass ID	Composition	*I*(**A**)/*I*(**C**)	*I*(**A** + **B**)/*I*(**C**)	Mole% oxide additive	Crystalline phases after PCT
P-8	Pb	0.46	2.23	16.8	$PbTe_3O_7$
P-11	Pb+Cl	1.31	3.38	13.1	$PbTe_3O_7$
P-7	Al/B	0.47	0.47	29.5	α-TeO_4
P-2	Al/B+Cl	0.26	0.26	24.9	β-TeO_4, $Na_2Te_2O_7$
P-9	W	0.91	0.91	18.7	None
P-12	W+Cl	1.87	1.87	14.5	Ba_3WO_6
P-5	P	0.66	0.66	10.0	α-TeO_4
P-14	P+Cl	0.66	0.66	7.9	β-TeO_4
P-4	Zn	1.48	1.48	30.1	α-TeO_4, $Zn_2Te_3O_8$
P-13	Zn+Cl	1.48	1.48	24.5	β-TeO_4, $Zn_2Te_3O_8$

As stated by Himei et al., all of these band ratios should be properly corrected by a *y*-intercept when against O/Te on a molar basis (Himei et al., 1994). However, we elected not to follow this approach because we were more interested in comparing the influence of primary dopants and the presence of mixed chlorides on the structural variation(s) between glasses in each binary/ternary system. Glasses with *I*(**A**) < *I*(**C**) should have more TeO_4 units, and those with ratios > 1 should have more TeO_3 units. Ratios that decrease in the XCl_{20}-containing glass should indicate presence of more TeO_4 than glasses without XCl_{20}, while ratios that increase should indicate more TeO_3. Glasses with ratios < 1 include almost all of the glasses: P-8 (Pb), P-11 (Pb+Cl), P-7(Al/B), P-2 (Al/B+Cl), P-9 (W), P-5 (P), and P-14 (P+Cl). Glasses predicted to have primarily TeO_3 units include P-12 (W+Cl), P-4 (Zn), and P-13 (Zn+Cl). It is likely that results for P-9 (W) and P-12 (W+Cl) are influenced by peaks from the W network because, according to Sekiya et al., bands **A**, **B**, and **C** all have contributions from the W-network modes while **E** contains only contributions from the Te network (Sekiya et al., 1994a). Therefore, it is difficult to comment on the P-9 (W) and P-12 (W+Cl) with only the Raman spectra.

It was instructive to compare the ratios for the Zn glasses with those of the Al/B glasses. These four glasses had nearly identical molar additions of oxides to the TeO_2. However, the Zn glasses (P-4 and P-13) were highly depolymerized (i.e., the TeO_4 *tbp* units have been changed to mostly TeO_3 *tp* units), as observed in other studies. This is because the ZnO breaks the Te-O chains and only secondarily acts as a glass former. In Al/B glasses (P-7 and P-2), however, only TeO_4 units are expected from TeO_2-B_2O_3 systems (Rong et al., 1992). This leaves 8–9 mole% Al_2O_3, which creates ~15% *tp* groups based on NMR of TeO_2-Al_2O_3 (Sakida et al., 2001). Ignoring the role of B_2O_3, for 8–9 mole% Al_2O_3, one would estimate ~45% Al in AlO_6, ~20% in AlO_5, and ~34% in AlO_4, though it is unknown how the simultaneous presence of B_2O_3 would affect the Al speciation (Sakida et al., 2001). When adding XCl_{20} to these glasses, the spectra for the P-13 (Zn+Cl) glass did not noticeably change while the ratios decreased for P-2 (Al/B+Cl), indicating that even more TeO_4 formed. These differences are important when considering the radically different behavior of the Zn glasses (P-5 and P-14) and Al/B glasses (P-7 and P-2) in chemical durability tests. As shown Table 4.6, in P-4 (Zn) P-13 (Zn+Cl) glasses were very

soluble, whereas the P-7 (Al/B) and P-2 (Al/B+Cl) glasses were only slightly soluble, i.e., P-13 (Zn+Cl) showed very high NL_{Na} at 88.9 g/m^2 and P-2 (Al/B+Cl) showed low NL_{Na} at 6.71 g/m^2.

For the Pb glasses, P-8 and P-11, the estimated fraction of *tp* from NMR data in the literature is ~33% for the ~17 mole% PbO-TeO_2 glass, which is similar to our glass without chlorides (Sakida et al., 2001). This suggests that the ratio I(**A**)/I(**C**) is more reliable than NMR. The value of this ratio is < 1 (*tbp* > *tp)*, while I(**A** + **B**)/I(**C**) is > 1 (*tbp* < *tp)*. The fraction of *tp* for P-8 (Pb) glass estimated from NMR (~33%) is significantly greater than that estimated for the P-7 (Al/B) glass (~15% *tp*) but the amount of *tp* clearly decreased in P-11 (Pb+Cl) glass when chlorides were added.

Though P-5 (P) and P-14 (P+Cl) glasses showed predominantly *tbp* structures, their chemical durability was very poor. The P+Cl glass was phase-separated, the leachate from this glass was highly enriched in P, and the residual solids were composed primarily of crystalline β-TeO_4 (Riley et al., 2010). Kozhukharov et al. investigated the TeO_2-P_2O_5 binary system for regions of miscibility/immiscibility and found that uniform glass was formed at 3–15 mole% P_2O_5 (Kozhukharov et al., 1978). However, many complex immiscible phases also occurred at various temperatures within this region. These results could explain the incongruent leaching observed during the PCT as well as the phase separation.

4.2.1.3 Chemical Durability Analysis

The chemical durability of the glasses studied here did not appear to fit an obvious trend and varied widely from NL_{Na} = 0.478 to 88.9 g/m^2 release over the course of the seven-day PCT (see Table 4.6). The variation was attributed to phase separation in some of the glasses and the ratio of *tp*:*tbp* structural units. The Pb+Cl (P-11) glass showed the highest chemical durability, W+Cl (P-12) and Al/B+Cl (P-2) were only somewhat durable, and P+Cl (P-14) and Zn+Cl (P-13) showed poor chemical durability. The reduced chemical durability in the Al/B+Cl (P-2) and P+Cl (P-14) glasses was likely due to phase separation, which was clearly visible in these glasses with the naked eye (Riley et al., 2010).

Table 4.6. Summary of normalized release results from seven-day PCT-B for P-series tellurite glasses with XCl_{20} (Riley et al., 2010).

Glass ID	Composition	NL_{Li} (g/m^2)	NL_{Na} (g/m^2)	NL_K (g/m^2)	NL_{Cl} (g/m^2)
P-11	Pb+Cl	1.00	0.478	0.298	0.528
P-2	Al/B+Cl	5.50	6.72	3.45	3.85
P-12	W+Cl	7.25	10.3	2.85	4.62
P-14	P+Cl	82.7	86.0	88.4	30.3
P-13	Zn+Cl	85.3	88.9	89.1	84.7

Although the Pb+Cl glass, P-11, performed very well in the PCT, it had a I(**A**)/I(**C**) ratio similar to that of the Zn+Cl glass (P-13), which performed the worst of all the glasses studied (NL_{Na} = 88.9 g/m^2), implying similar *tp*:*tbp* fractions in these two glasses (see Table 4.5). However, since the Pb glasses, P-8 and P-11, also had a **B** band present adding to the *tp* signal (>60%), the fraction of *tp* units in the Pb+Cl glass was the highest of the glasses studied, i.e., I(**A** + **B**)/I(**C**). This suggests that perhaps the *tp* structure is necessary to increase chemical durability, although more work is needed to verify the difference between the **A** and **B** bands since the **B** band did not appear in any of the glasses other than the Pb glasses and seem to contribute significantly to the *tp* unit signal.

The Al/B+Cl glass, P-2, was the second-best-performing XCl_{20}-loaded glass, with NL_{Na} = 6.72 g/m^2. However, the Al/B+Cl and Pb+Cl (P-11) glasses were an order of magnitude apart in NL_{Na} and the leaching appeared very different in each glass. The leaching in the Al/B-glasses, P-7 and P-2, appeared incongruent, likely due to the fact that the Al/B+Cl glass was visibly phase-separated before the PCT; also, the PCT leachate was enriched in B and Cl. Interestingly, the total dissolved Al species measured in the PCT leachates from both the Al/B-glasses was very low (Riley et al., 2010). Also, the dissolved B species measured in the PCT leachates for the Al/B glass was nearly double (1.855×) that in the Al/B+Cl glass, whereas the amount of B_2O_3 present in the Al/B+Cl glass was not very different from that in the Al/B glass (P-7, 8.1 versus 9.0 mass%) (Riley et al., 2010). This seems to suggest the presence of boron,

which would imply a more chemically stable configuration, in the presence of XCl_{20} in the Al/B glasses, and that Al_2O_3 seems to be a very stable component in this particular glass formulation.

4.2.1.4 Thermal analysis

The P-8 (Pb) and P-11 (Pb+Cl) P-series lead-tellurite glasses were studied with the TA Instruments SDT Q600 DTA-TGA and the results are presented in Table 4.7 and Figure 4.9. The T_g of P-8 (~291°C) is comparable to a typical tellurite glass and when 10 mass% of XCl_{20} was added to P-8 to produce the P-11 glass, the T_g was reduced to ~254°C for the 10°C/min ramp rate. The temperature stability of these glasses can be increased by incorporating additional components into the glass, such as GeO_2 and Al_2O_3; these options are currently under investigation (Hocdé et al., 2004).

Table 4.7. Summary of DTA-TGA results for P-8 and P-11 run at both 10 and 15°C/min ramp heating rates.

Glass ID	Rate, °C/min	Mass, mg	T_g, °C	Peak ID	T_x (onset), °C	T_c (max), °C	T_M, °C
P-8	10	75.549	290.53	(1)	321.37	334.42	524.22
				(2)	371.98	387.26	620.10
	15	67.482	288.68	(1)	321.00	334.15	522.09
				(2)	374.79	390.59	619.90
P-11	10	34.805	253.90	(1)	392.36	417.02	536.38
				(2)	-	-	-
	15	33.378	264.00	(1)	326.79	340.06	542.38
				(2)	366.59	395.03	

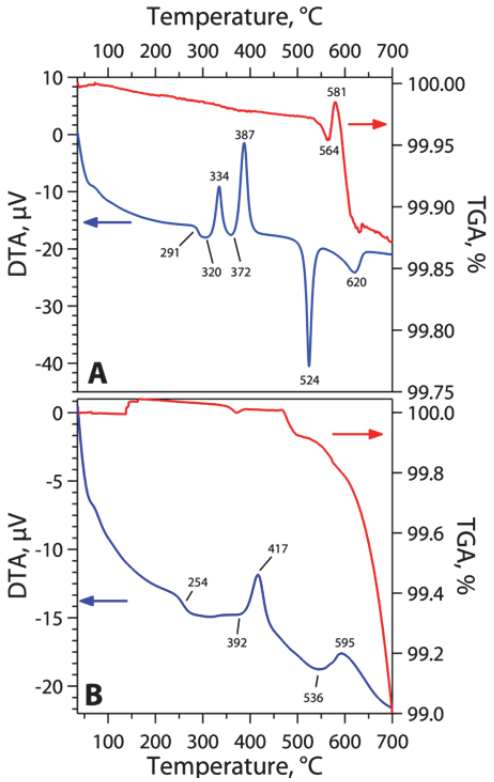

Figure 4.9. DTA/TGA results for (A) P-8 and (B) P-11.

In addition, the thermal diffusivity was measured for P-11 with a NETZSCH LFA-457. In order to perform these measurements, discs of the specimens were prepared from cylinders cast in fused quartz

molds (see Figure 3.3). The thermal diffusivity for P-11 was measured at 0.23–0.28×10^{-6} m^2/s and these results are presented in Figure 4.10a. We did prepare a disc of P-8 for thermal diffusivity measurements, although the glass tends to crystallize when we try to pour and anneal cylinders that can be cut into discs (see Figure 4.10b). These crystals would make it difficult to accurately measure the thermal diffusivity for the glassy phase.

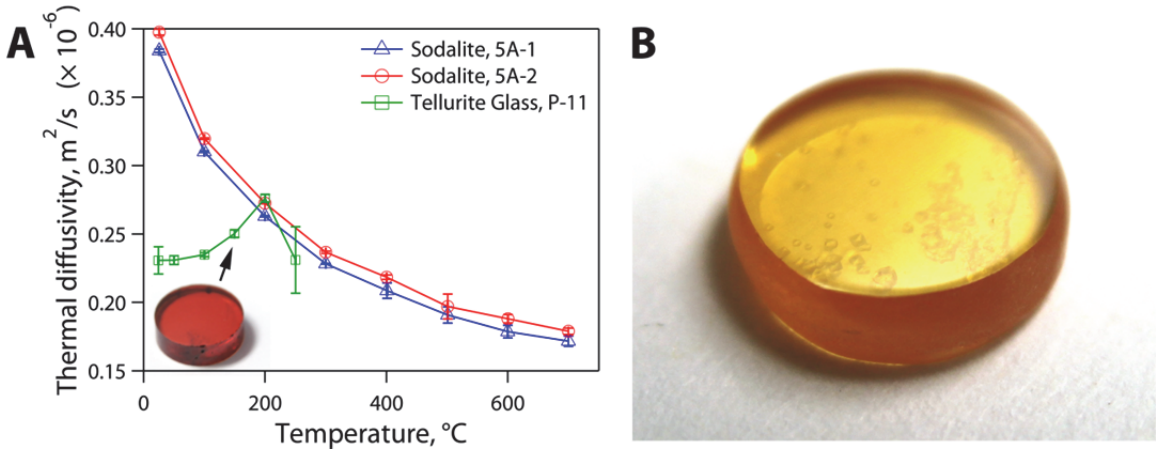

Figure 4.10. (A) Thermal diffusivity, α, for tellurite glass, P-11, as well as PNNL Sodalite, 5A, as a function of temperature. (B) A P-8 specimen prepared for LFA measurements; it is slightly crystallized (see small, clear $Pb_2Te_3O_7$ crystals throughout the bulk).

4.2.2 Tellurite Glasses: Lead-Tellurite and Structural Variation Glasses Study

4.2.2.1 Visual Appearance

The lead-tellurite glasses appeared very different from one another; TPb_0 was a transparent yellow-orange glass; TPb_5, TPb_{10}, $TPb_{12.5}$, and TPb_{14} were transparent red glasses; TPb_{15} was phase-separated; and $TPb_{17.5}$ and $TPb_{22.5}$ were dark yellow-white and opaque ceramic-like in appearance (Figure 4.11). Phase separation was observed at 15% $X$$Cl_{20}$-loading, although not at 14%. Thus, the $X$$Cl_{20}$-loading limit was determined to be between 14% and 15% in this lead tellurite system (TeO_2:PbO = 3.545, by mass).

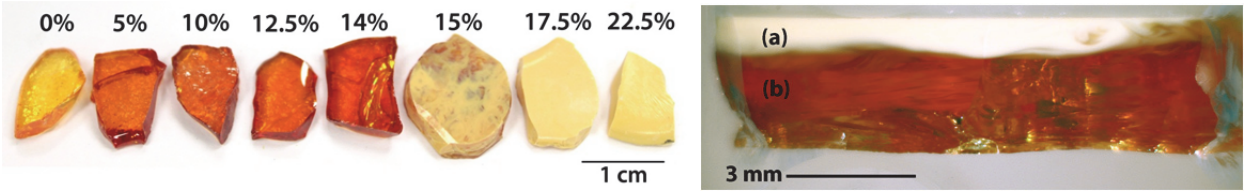

Figure 4.11. Pictures of lead-tellurite glasses at different waste loadings including a polished cross-section of the two phases present in the phase-separated T2G-1-PbO specimen (Riley et al., 2010). The layers in the polished cross-section are discussed on the following page.

Pictures of all the structural variation glasses are presented in Figure 4.12. From Figure 4.12, it is evident that the structural variation glasses all had appearances based on colors but that the crystalline/amorphous nature varied somewhat; some made very nice glasses (e.g., T2G-33 and T2G-34) while others were highly crystalline (e.g., T2G-21b – T2G-21d). All of these glasses had very low viscosities during melting/pouring. For all of the lead-tellurite glasses, a temperature of 700°C was sufficient for melting. For the ZnO-based glasses, T2G-29a and T2G-29b, a higher temperature of 730°C was required for melting. Some volatilization was observed for T2G-29a, T2G-32, and T2G-33 whereas no volatilization was observed for T2G-27a, T2G-27b, or T2G-34.

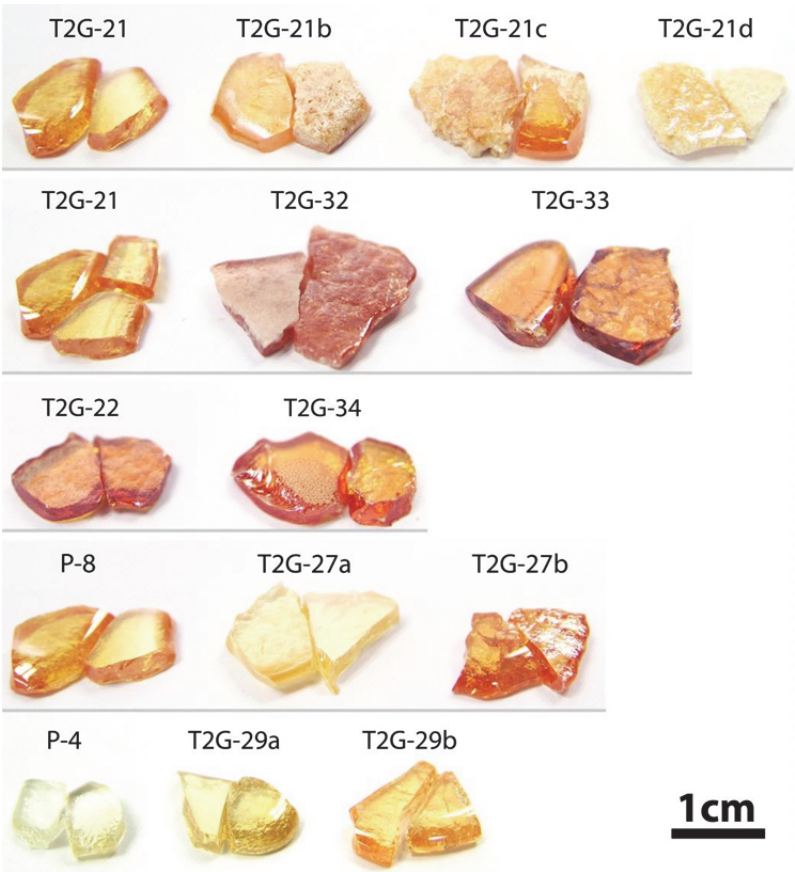

Figure 4.12. Summary figure providing visual comparisons between the structural variation glasses. Here, T2G-21 was used as a placeholder for P-8 since they have identical compositions and appearances.

T2G-1-PbO, a glass of the same composition as TPb_{15} but from FY2010, is a lead-tellurite glass with 15 mass% XCl_{20} and was discussed briefly in the FY2010 report (Riley et al., 2010). This glass was phase-separated (Figure 4.11), and showed very minor XRD diffraction peaks when analyzed as a mixed powder, with PbO as the best-fitting phase (Figure 4.16). This phase separation was observed as two distinct phases, (a) an opaque yellow-white, ceramic-like phase on the top surface and (b) a transparent red glass on the bottom (see Figure 4.11). A piece of the phase-separated T2G-1-PbO glass was mounted in Quick Cure resin (Allied High Tech Products, Inc., Rancho Dominguez, CA), cross-sectioned, polished and analyzed with optical microscopy and scanning electron microscopy-energy dispersive spectroscopy (SEM-EDS). Phase (a) was determined to be higher in Cl (by 36%), Na (by 23%), K (by 50%), and Pb (by 9%) than phase (b) with the balance in phase (b) being a higher quantity of measured TeO_2 (in mass percent) (Riley et al., 2010).

4.2.2.2 Raman Analysis

Micro-Raman analysis of the two phases in T2G-1-PbO (Figure 4.11) revealed that, qualitatively, the **B** (*tp*) band was substantially larger than the **C** (*tbp*) band in phase (a) when compared to phase (b), as seen in Figure 4.13—see Table 3.13 for band assignments. This implies that the *tbp* units are more prevalent in phase (b), suggesting that alkali and/or chlorine enrichment in phase (a) leads to more depolymerization of the tellurite network (i.e., more *tp* TeO_3 or TeO_{3+1} units). The strongest, cleanest micro-Raman signal of the white phase was analyzed quantitatively as well. Microscopy and XRD did not indicate that the white phase was crystalline, but it could have been phase-separated on a very small scale.

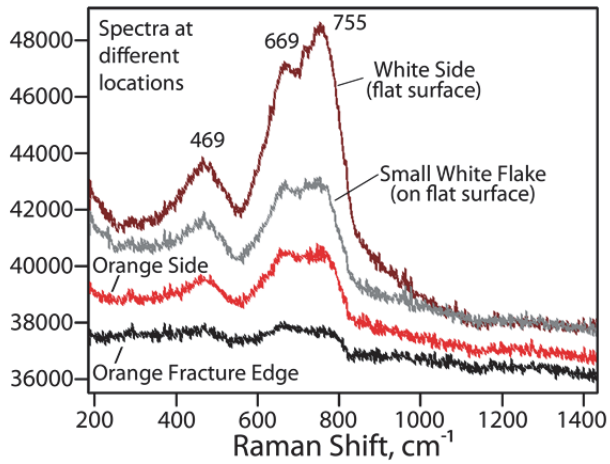

Figure 4.13. Micro-Raman spectroscopy of separated phases in T2G-1-PbO (same composition as TPb_{15}).

The glass structure in the lead-tellurite and some of the structural variation glasses was further assessed by investigating the Raman spectra. Some representative Raman spectra are shown in Figure 4.14. From both parts of Figure 4.14 it can clearly be observed that adding XCl_{20} to these glasses reduces the overall Raman intensity. Spectra were fitted as previously described, and the resultant area deconvolution is shown in Table 4.8 according to the bands assigned in Table 3.13.

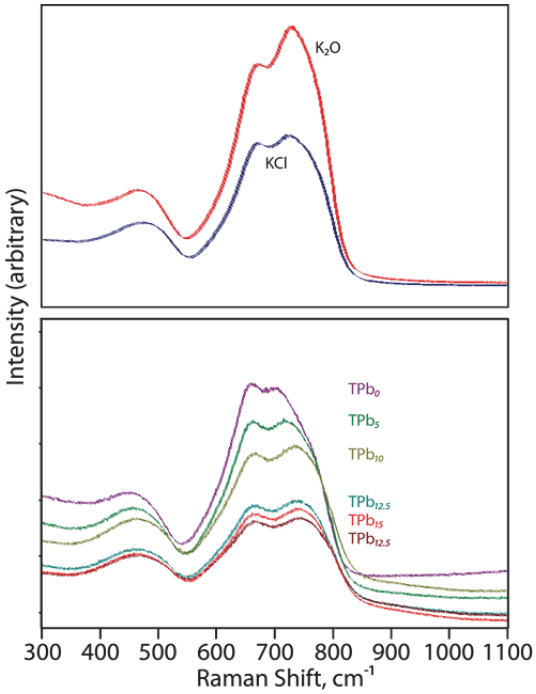

Figure 4.14. Raman spectra of K_2O and KCl glasses (top) and some of the lead-tellurite glasses (bottom).

Table 4.8. Fitted Raman data for lead-tellurite and some of the structural variation study glasses. The band names are listed in **bold** type. Note that the frequencies were fixed during the fitting and are shown at the top of each column of integrated intensities.

	$\tilde{\nu}$ (cm^{-1}):	432.7	476	596.5	648	710.9	769.7
Name	Alternate Name	**E1**	**E2**	**D**	**C**	**B**	**A**
TPb_0	T2G-21	3.84E+05	2.40E+05	3.73E+05	1.48E+06	2.49E+06	6.82E+05
P-8	-	6.27E+06	6.21E+06	9.10E+06	3.40E+07	6.03E+07	1.55E+07
TPb_5	T2G-22	3.49E+05	3.53E+05	3.27E+05	1.22E+06	2.14E+06	1.04E+06
TPb_{10}	T2G-23	2.50E+05	4.60E+05	2.78E+05	8.59E+05	1.77E+06	1.06E+06
P-11	-	1.33E+06	1.90E+06	1.15E+06	4.87E+06	1.01E+07	6.36E+06
$TPb_{12.5}$	T2G-24	1.99E+05	4.02E+05	1.98E+05	5.86E+05	1.43E+06	7.83E+05
TPb_{14}	T2G-30	3.07E+05	9.46E+05	5.80E+05	1.46E+06	3.41E+06	2.11E+06
$TPb_{14\text{-}repeat}$	T2G-30b	4.35E+04	9.69E+04	2.45E+04	1.57E+05	4.56E+05	2.56E+05
$TPb_{15\text{-}powder}$	T2G-1	1.39E+05	4.46E+05	1.32E+05	4.56E+05	1.32E+06	6.58E+05
$TPb_{15\text{-}white}$	T2G-1	8.03E+04	1.11E+05	3.01E+04	2.60E+05	4.84E+05	4.45E+05
$TPb_{17.5}$	T2G-25	2.16E+05	4.47E+05	1.80E+05	5.02E+05	1.52E+06	7.30E+05
$TPb_{22.5}$	T2G-30	9.58E+04	2.91E+05	1.15E+05	4.53E+05	1.20E+06	6.84E+05
K_2O	T2G-27a	6.17E+05	6.85E+05	1.00E+06	2.67E+06	7.70E+06	2.89E+06
KCl	T2G-27b	6.35E+05	6.42E+05	4.85E+05	1.93E+06	4.57E+06	1.74E+06
XO_{20}	T2G-34	5.71E+04	7.92E+04	1.09E+05	3.08E+05	7.55E+05	3.02E+05

A progression of the *tbp*/*tp* relative ratio, which indicates polymerization of the tellurite network, as determined from the area ratio (**C** + **D**)/(**A** + **B**) in the high frequency envelope, is shown in Figure 4.15a. The trend is a smooth decrease until about 15 mass%, after which it remains nearly unchanged. Waste loadings 0, 10, 14, and 15 mass% have two data points each, and the line is an average ratio of the two samples produced at this waste loading (Figure 4.15a). Noting that the 14 mass% points are considerably different, it may be that the 14 mass% glass is on the verge of major structural change associated with devitrification, and slightly different cooling profiles produce different glass structures. It should be remembered that 15 mass% XCl_{20} represented the point at which phase separation began to be visibly apparent. One of the data points at 15 mass% represents the Raman spectra taken on a powdered glass containing both phases, and the other is a fit of the white phase micro-Raman data. In contrast with the 14 mass% data, these 15 mass% ratios are remarkably similar to each other. At loadings higher than that inducing phase separation, it appears that the relative depolymerization of the tellurite network (as measured by *tbp*/*tp*) proceeds no further. From the micro-Raman and EDS on the phase-separated 15 mass% XCl_{20}, the orange-red glassy phase is enriched in Te and has more *tbp* groups than the cloudy-whitish phase that is enriched in alkali, Cl, and slightly in Pb, and has more *tp* groups.

Figure 4.15b shows a plot of the peak width as a function of waste loading for several of the Raman bands fitted with fixed frequencies. It is apparent that at least up to 15 mass% *X*Cl loading and probably higher, the band width for **A** + **B** bands assigned to *tp* units increases, indicating increased local site disorder. By contrast, the band width of the **C** + **D** bands assigned to *tbp* units do not change much with mixed chloride loading. This implies that the disorder with increasing additions of alkali, alkaline earth, lanthanide, and chloride ions manifests in the *tp* structural units, which makes sense since it is these depolymerized tellurite units that accommodate these ions in the glass structure. Since there are so many

different waste ions to be incorporated, it seems reasonable that as the loading is increased, the number of different local *tp* units would increase (i.e., the disorder increases). This effect seems to saturate near 15 mass% as also was seen with the area ratios in Figure 4.15a, and data in Figure 4.15b for the *tp* peaks (**A** + **B**) are also not inconsistent with a change in mechanism near 15 mass%, but data are more scattered for the peak width.

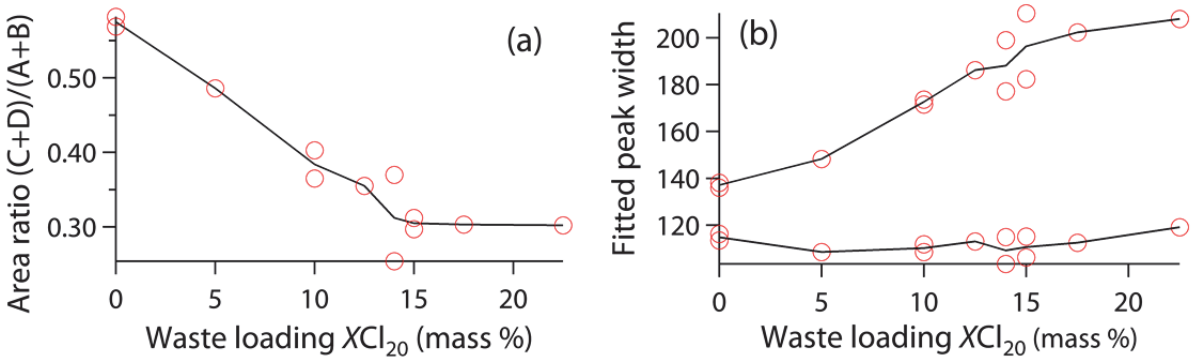

Figure 4.15. Quantitative Raman analysis for the lead-tellurite glasses. (a) *tbp*/*tp* area ratio from Raman spectra as a function of waste loading. **A** lower (**C**+**D**)/(**A**+**B**) ratio represents a more depolymerized network. (b) Fitted peak width as a function of loading, indicating site disorder in the *tp* part of the glass structure with increasing waste loading. In both figures, lines indicate averages where more than one data point (circle) is shown.

An examination of the effect of Cl/O ratio for the structural variation glasses is shown in Table 4.9. From this data we can examine the effects of both Cl and cations. Comparing the TPb_0 and TPb_5 specimens, the addition of 5 mass% XCl_{20} results in a depolymerization of the network (lower area ratio), but it is not entirely clear whether this is due to the Cl or the cations in the waste or both. Comparing TeO_2-PbO-XO_{20} (T2G-34) and TeO_2-PbO-XCl_{20} (TPb_5) gives an idea of the separate effects of the cations and chloride, since the amounts of Te and Pb relative to the waste cations is the same for both the oxide and the chloride waste. The data indicate that the chloride in XCl_{20} actually *repolymerizes* the tellurite network compared to the XO_{20} glass with the same modifier cations, presumably by scavenging some of the alkali (or possibly alkaline earths and/or lanthanides), reducing the amount available for network breaking and formation of *tp* units. Finally, comparison of the K_2O and KCl glasses having the same relative amount of K compared to Te and Pb (see Table 3.10), indicates the same trend, i.e., that the chloride-containing glass is slightly more polymerized than the one without chloride when both contain the same relative amount of alkali to the main glass formers. This is in agreement with Tanaka et al., who observe a suppression of formation of the *tp* units when Cl is substituted for O in Li-Te-O-Cl glasses due to the strengthening of the Te-O_{ax} bond since a smaller electronic charge is donated from Te-Cl_{eq} than from Te-O_{eq} (Tanaka et al., 1988b)—see Figure 2.1.

Table 4.9. Quantitative Raman analysis of some of the lead-tellurite and structural variation glasses.

Sample ID	Glass System	Cl/O	(C+D)/(A+B)
T2G-21 (TPb_0)	TeO_2-PbO (TPb_0)	0.000	0.58
T2G-22 (TPb_5)	TeO_2-PbO-*X*Cl (TPb_5)	0.080	0.49
T2G-34 (XO_{20})	TeO_2-PbO-*X*O	0.000	0.39
T2G-29a	TeO_2-PbO-K_2O	0.000	0.35
T2G-29b	TeO_2-PbO-KCl	0.096	0.38

4.2.2.3 X-Ray Diffraction (XRD) Analysis

The XRD results for the lead-tellurite glasses are presented in Figure 4.16 where the best-fitting phases were identified as those presented in Table 4.10. XRD analysis showed a small fraction of octahedral lead tellurite ($Pb_2Te_3O_7$) crystals in TPb_0 observed with optical microscopy (Kulcu, 1987). TPb_5, TPb_{10},

$TPb_{12.5}$, and TPb_{14} were determined to be amorphous whereas TPb_{15}, $TPb_{17.5}$, and $TPb_{22.5}$ showed a small degree of crystallization. The glasses with XCl_{20}-loadings at ≥15 mass% looked highly crystalline, so the small degree of crystallization was surprising considering the appearance. Later, with SEM, we verified that this color change was the result of nano-phase-separation of alkali chloride inclusions in the yellow-white phase (see Figure 4.18). At 15 mass% loading, a small fraction of PbO was observed in the diffraction pattern. This PbO was not observed as a crystalline product in any of the other glasses. At XCl_{20}-loadings >15 mass%, chloride phases were observed. At an XCl_{20}-loading of 17.5 mass% ($TPb_{17.5}$), $NaClO_3$, Ba_4OCl_6, and $BaPrO_3$ were the best-fitting patterns and at an XCl_{20}-loading of 22.5 mass% ($TPb_{22.5}$), KCl, NaCl, $CsPbCl_3$, and K_2PrCl_5 were the best-fitting patterns. Since $CsPbCl_3$ is the only one of these seven phases that contains the glass-forming components, this suggests that the waste-loading limit was achieved because the waste components were no longer stable in the glass network.

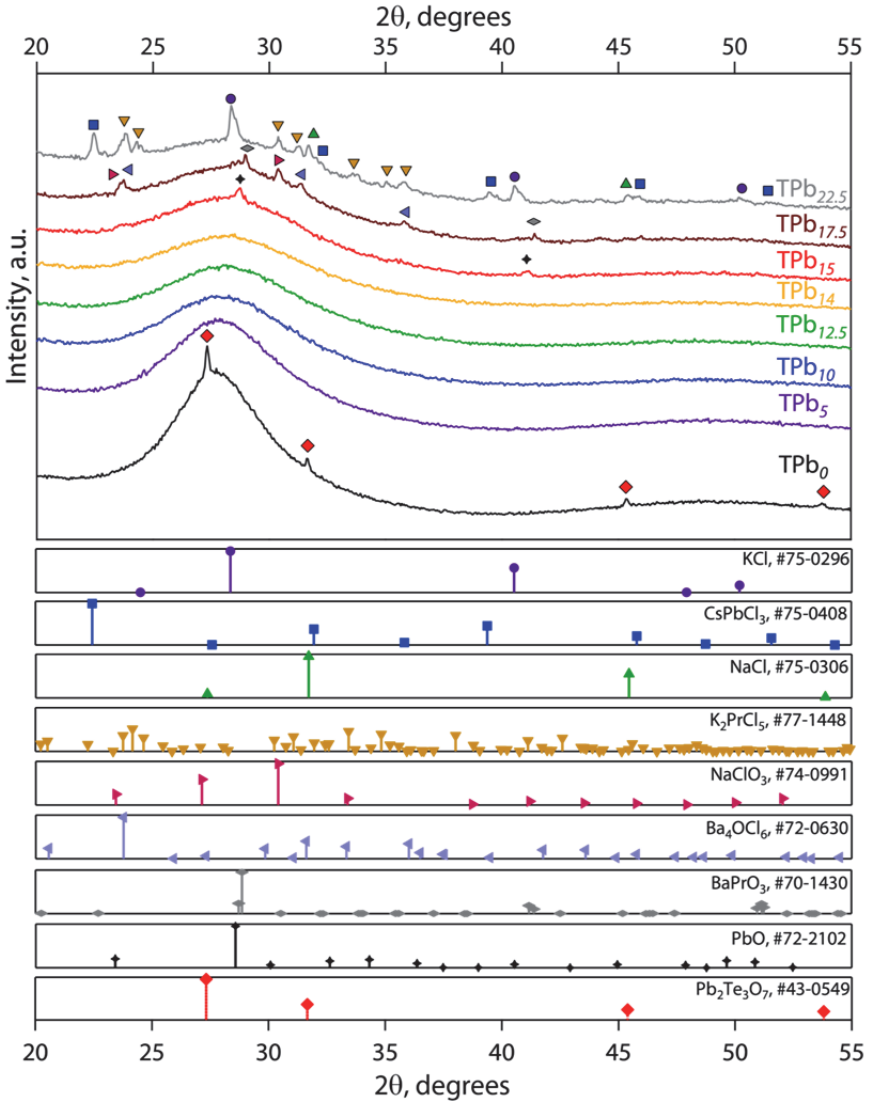

Figure 4.16. Summary of XRD results for lead-tellurite variation study glasses. The details of these phases can be found in Table 4.10.

Table 4.10. Summary of crystalline compounds identified in lead-tellurite glasses with XRD.

Compound	PDF#	ICSD#	SG (SG#)	Reference
KCl	75-0296	28938	*Fm*-3*m* (225)	(Barrett and Wallace, 1954)
NaCl	75-0306	28948	*Fm*-3*m* (225)	(Barrett and Wallace, 1954)
$CsPbCl_3$	75-0408	29067	*Pm*-3*m* (221)	(Moller, 1957)
K_2PrCl_5	77-1448	48190	*Pnma* (62)	(Meyer et al., 1985)
$NaClO_3$	74-0991	26684	*P*213 (198)	(Zachariasen, 1929)
Ba_4OCl_6	72-0630	16026	*P*63*mc* (186)	(Frit et al., 1970)
$BaPrO_3$	70-1430	2753	*Pbnm* (62)	(Jacobson et al., 1972)
PbO	72-2102	20362	*Pbcn* (60)	(Zaslavsky et al., 1950)
$Pb_2Te_3O_7$	43-0549	N/A	*Fm*-3*m* (225)	(Kulcu, 1987)

The fitted backgrounds from the XRD spectra were plotted to show the differences in the amorphous structure between the lead-tellurite glasses (Figure 4.17a). From this plot, it clear that the amorphous structure of the $X\text{Cl}_{20}$-loaded glasses is fairly consistent, though different from TPb_0 without the $X\text{Cl}_{20}$ addition. The location of the amorphous humps does shift with $X\text{Cl}_{20}$ additions, suggesting a consistent structural shift as the waste components modify the glass network (Figure 4.17b).

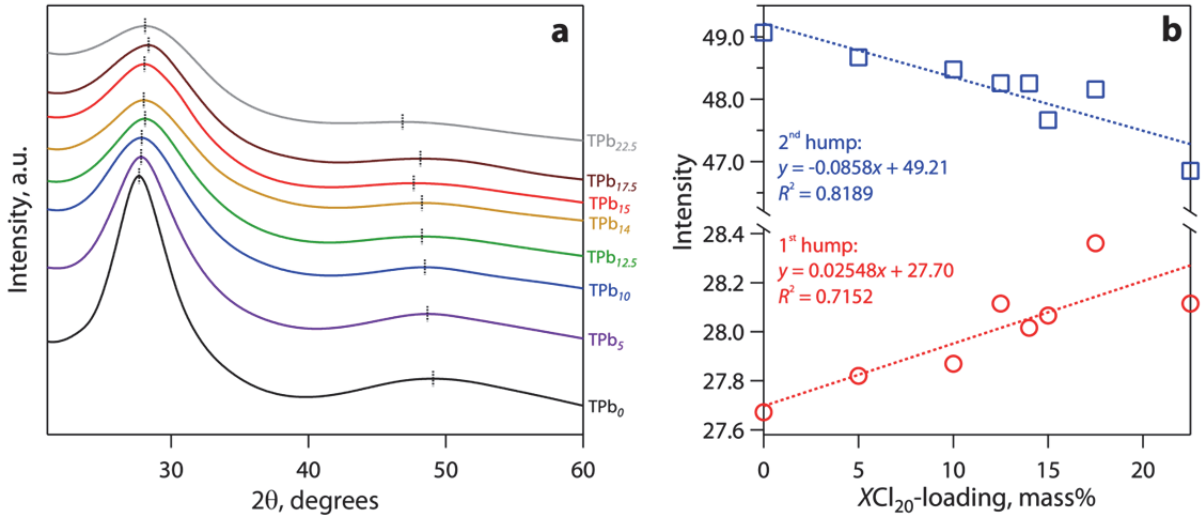

Figure 4.17. (a) Background fits on raw XRD data from the lead-tellurite glasses presented in Figure 4.16. (b) Amorphous hump maxima locations in 2θ—locations denoted by vertical lines in (a)—along with linear data fits for informational purposes only.

4.2.2.4 Scanning Electron Microscopy and Energy Dispersive Spectroscopy

After observing the T2G-1-PbO glass in the SEM, it was apparent that the yellow-white phase was actually phase-separated from the bulk glass. This phase-separation was only observed in the top, yellow-white portion of the glass as dark spherical inclusions—see Figure 4.18. These dark inclusions had a much lower average atomic number than the surrounding matrix as evidenced by the backscattered imaging technique used to collect the micrographs where elements with a higher atomic number appear brighter than elements with a lower average atomic number.

In the yellow-white phase, these inclusions ranged in size from 288±38 nm in diameter towards the top of the yellow-white phase to smaller droplets at 61±10 nm towards the bottom of the yellow-white phase, next to the glassy phase. Very few droplets were observed in the top 5 µm of the yellow-white phase at the very top of the sample and we believe this is due to the fact that this surface was cooled by the air

during quenching more rapidly than the glass just below the surface. Also the droplets that were found at the top of the sample were very small (< 60 nm).

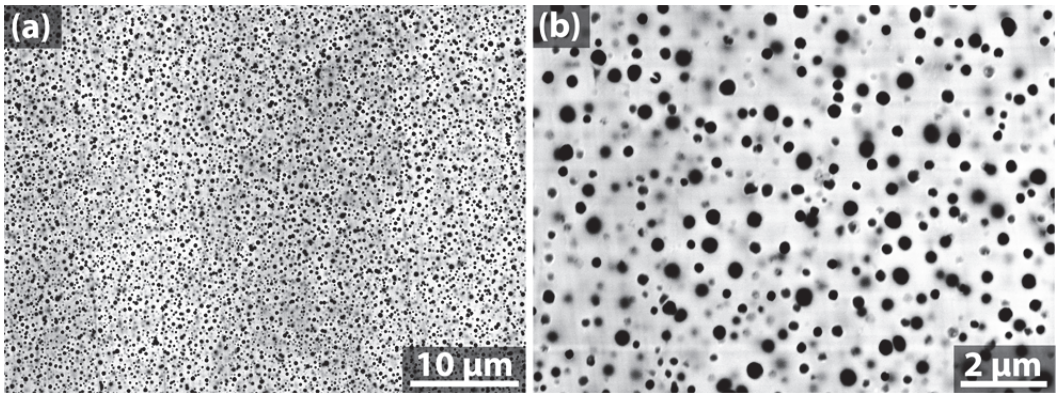

Figure 4.18. Scanning electron microscopy of yellow-white region in T2G-1-PbO showing nano-droplet phase-separation.

EDS area analysis was performed on several of these inclusions in different regions and the compositional results were compared with the results from a series of area scans of the surrounding matrix—see Figure 4.19. From Figure 4.19, it is apparent that the droplets show a higher concentration of the alkali chloride mixture, a higher tellurium concentration, and a lower lanthanum concentration than the surrounding matrix. These results suggest the following:

1) As the $X\text{Cl}_{20}$-loading was increased in these glasses, some of the $X\text{Cl}_{20}$ components were incorporated into the glass (e.g., Ln) while others (e.g., Na, K, and Cl) were excluded from the glassy phase in regions where the cooling rate was not sufficiently high.
2) As the $X\text{Cl}_{20}$-loading was increased, the alkali chlorides were not incorporated into the glass as well as the fraction of lanthanide salts.
3) The Ln fractions observed in both the glassy and inclusion phase were significantly higher in the phase-separated fraction of the sample (>20 mass%) than in the as-batched glass (~8.3 mass%)—see Figure 4.19b. This suggests that the Ln fraction from the lower, glassy region of the sample was pushed up into the upper phase-separated portion.

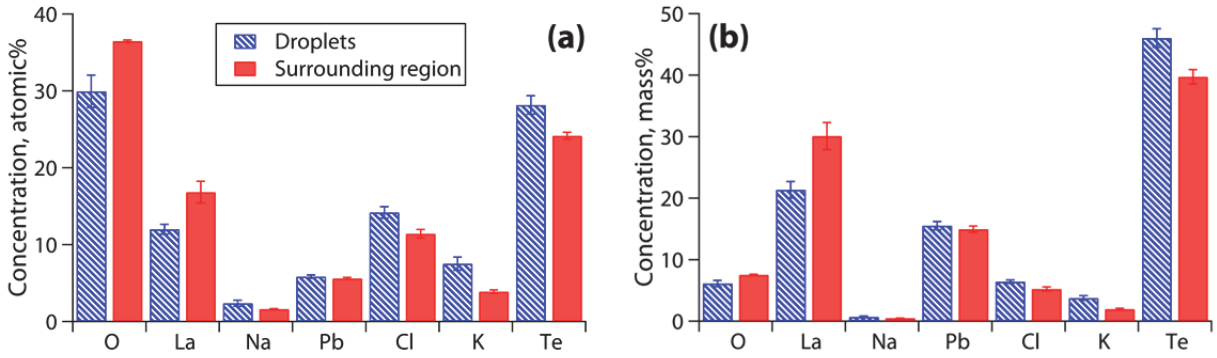

Figure 4.19. Energy dispersive spectroscopy on phase-separated region of T2G-1-PbO where the average composition of the dark droplets in Figure 4.18 is compared to that of the surrounding lighter matrix. The data is presented in both (a) atomic% and (b) mass%. It should be noted that that Li cannot be detected with this technique and is likely present in the droplets along with the other alkali cations. We expect that that the compositional values for the droplets are slightly skewed by the bulk matrix just below the droplets due to electron beam penetration into and interaction with the subsurface matrix.

These results reveal the real reason why the yellow-white phase on the top of T2G-1-PbO is opaque, which is that these phase-separated droplets of alkali halide salt are so small that they cause light-scattering centers, preventing the light to transmit through the sample in these regions. It is interesting

that the alkali chloride phase(s) did not show up on the XRD spectrum for this glass (Figure 4.16), even though they were present in such large quantities considering that these inclusions were found on the top ~40% of the glass in a fairly high density (>15% by volume). We presume that this implies that the alkali halide droplets are amorphous in structure although this has not yet been confirmed.

4.2.2.5 Density Analysis

Adding $X\text{Cl}_{20}$ to the baseline lead-tellurite glasses decreased the density, as one would expect considering that the density of the waste components, ρ_{salt}, is lower than that of the glass, ρ_B, at $< 3\times10^3$ kg/m^3 vs. $> 6\times10^3$ kg/m^3, respectively (see Table 3.4 and Figure 4.20a). The values obtained with the pycnometer are very representative of the entire glass sample in each case, considering that the bulk of each glass was analyzed at the same time. Thus, this does not account for a density difference between the individual phases present in the phase-separated glasses. The trend line drawn between the data points in Figure 4.20a would probably be linear if the waste components did not volatilize during the melting process (see section 4.2.2.6, Thermogravimetric Analysis).

Figure 4.20b shows the storage densities (ρ_S) of the different glasses as functions of waste loading. The "ρ_S" concept is presented here to show the large difference between the volumetric waste loading of the tellurite glasses compared to that of the baseline glass-bonded sodalite (163 kg/m^3). A waste form with a high ρ_S is preferred because it will require a smaller volume to store an equivalent mass of waste. For comparison, the final glass-bonded sodalite baseline waste form for the Echem waste is ~90% of its theoretical density with ρ_B = 2170 kg/m^3, ~7.5 mass% waste loading, giving ρ_S = 163 kg/m^3.

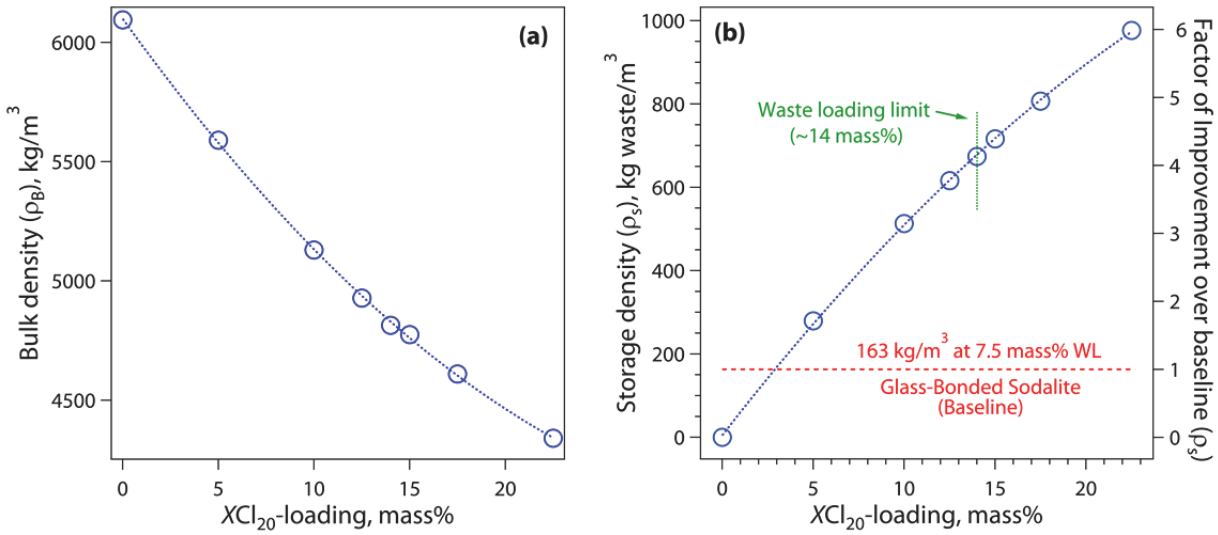

Figure 4.20. (a) Bulk density (ρ_B) and (b) storage density (ρ_S) of the lead-tellurite glasses as a function of $X\text{Cl}_{20}$-loading. In (b) a comparison is given to the baseline glass-bonded sodalite.

4.2.2.6 Thermogravimetric Analysis

Thermogravimetric analysis (TGA) of the lead-tellurite glasses showed that a small mass loss occurred during heating up to ~600°C (<1 mass%) with an increasing mass loss at T > 600°C (<6 mass%) where the glasses began to melt (Figure 4.21a). It is worth noting that the cumulative mass loss up to the heat-treatment temperature of 735°C increased in a consistent manner up to 14 mass% $X\text{Cl}_{20}$-loading, where it then plateaued (Figure 4.21b). This suggests that the $X\text{Cl}_{20}$ components, in addition to the maximum waste-loading (14 mass%), are probably retained in the glass as inclusions during cooling from liquid-liquid phase separation, as evidenced by SEM analysis (Figure 4.18), and not evolved.

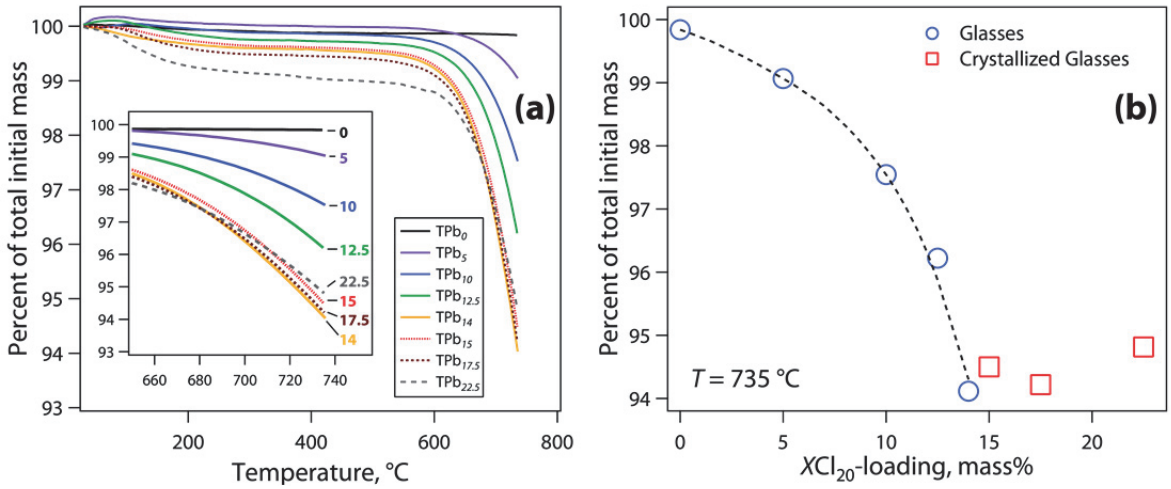

Figure 4.21. Summary of the TGA results for the lead-tellurite glasses. Figure (a) shows the thermogravimetric loss as a function of temperature; the inset shows a magnified view of the high-temperature end of the plot. (b) Cumulative mass retention at 735°C for all of the glasses.

The DSC results on the lead-tellurite glasses were interesting. We had difficulty setting up the instrument with a good baseline for data correctly, especially at temperatures above 500°C. Thus, the data collected in that temperature range was not displayed in Figure 4.22a. Glass TPb_0 had a distinct glass transition temperature (T_g) and two distinct exothermic events denoted by upward peaks of crystallization, $T_{c(1)}$ at the lower temperature and $T_{c(2)}$ at the higher temperature.

Table 4.11. Summary of the DSC results for the lead-tellurite glasses.

Glass ID	Alternative ID	T_g, °C	$T_{c(1)}$, °C	$T_{c(2)}$, °C	T_M, °C
TPb_0	T2G-21	263.6	308.9	355.9	527.7
TPb_5	T2G-22	278.5	-	383.2	-
TPb_{10}	T2G-23	258.6	-	382.5	-
$TPb_{12.5}$	T2G-24	246.1	348.6	379.3	-
TPb_{14}	T2G-31	220.3	267.7	397.1	-
TPb_{15}	T2G-26	244.2	290.5	381.9	-
$TPb_{17.5}$	T2G-25	228.0	283.5	373.1	-
$TPb_{22.5}$	T2G-30	220.7	292.1	373.7	-

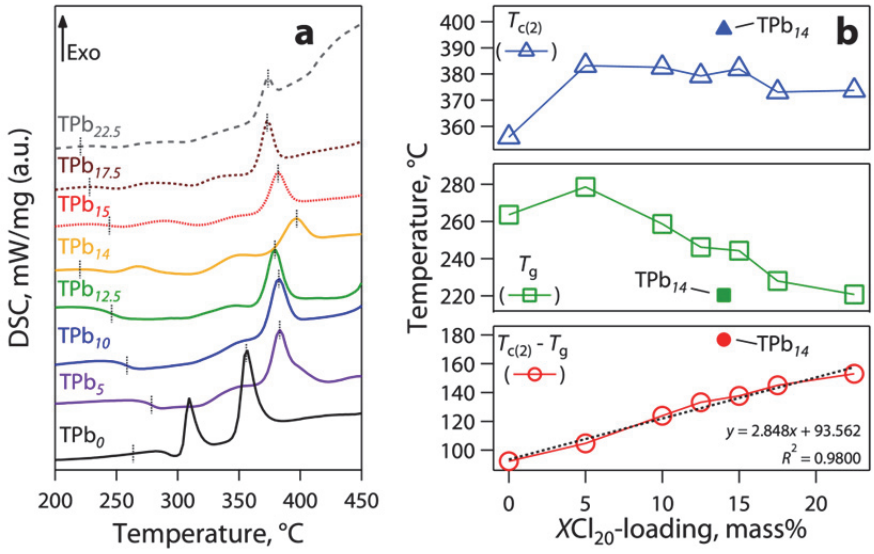

Figure 4.22. DSC results for the lead-tellurite glasses. Figure (a) shows the heat-flow curves as a function of temperature where the calculated T_g and $T_{c(2)}$ are marked with vertical lines. Figure (b), plotted from the data in Table 4.11, shows the trends for $T_{c(2)}$ (top), T_g (middle), and $T_{c(2)} - T_g$ (bottom); TPb_{14} did not fit well on any of the plots so it is denoted by solid symbols on each trend.

As the XCl_{20} was added to the TPb_0 composition, the T_g shifted (both to higher and lower temperatures) the $T_{c(1)}$ peak became buried in the noise, and the distance between the T_g and $T_{c(2)}$ became larger and larger (Figure 4.22b), suggesting a greater glass formation ability—see Equation 4.

These data revealed a few things that were occurring in the glasses during heating:

1) The thermogravimetric mass loss during heating was very low at $T \leq 600$°C (<1 mass%) but increased at $T > 600$°C (≤6 mass%) where the glasses melted. Since all of these glasses were melted at the same temperature of 700°C, which is not likely to be the ideal temperature for all of them, this volatility could be reduced by melting the glasses at their ideal melting temperatures.
2) The total mass loss as a function of XCl_{20}-loading increased to the glass that had the maximum loading without phase separation (TPb_{14}) where it then plateaued. This suggests that the glass was stabilized by the added waste components at a waste loading above 14 mass% XCl_{20}-loading.
3) Glassy phase(s) present seem to be stabilized by greater additions of the XCl_{20} components according to Figure 4.22b as evidenced by a greater K_{gl} as XCl_{20}-loading was increased. However, it is difficult to feel confident with this assessment after considering the phase-separation observed with the SEM in the glasses with ≥15 mass% XCl_{20}-loading (Figure 4.18).

4.3 Tellurite Crystals

In FY2011, only five of the tellurite crystals were fabricated and included: $ZnTeO_3$, $Zn_2Te_3O_8$, $SnTe_3O_8$, $ZrTe_3O_8$, and $TiTe_3O_8$. The procedures used to fabricate these samples were first attempted with the procedures laid out in Table 3.12, but in some cases changes were made to the proposed process. Pictures of these crystals are presented in Figure 4.23. It was difficult to achieve 100% of the target phases in all cases, except with $ZnTeO_3$, without at least minor impurities from unincorporated reactants. A summary of the crystalline phases found in these samples during XRD analysis is presented in Table 4.12.

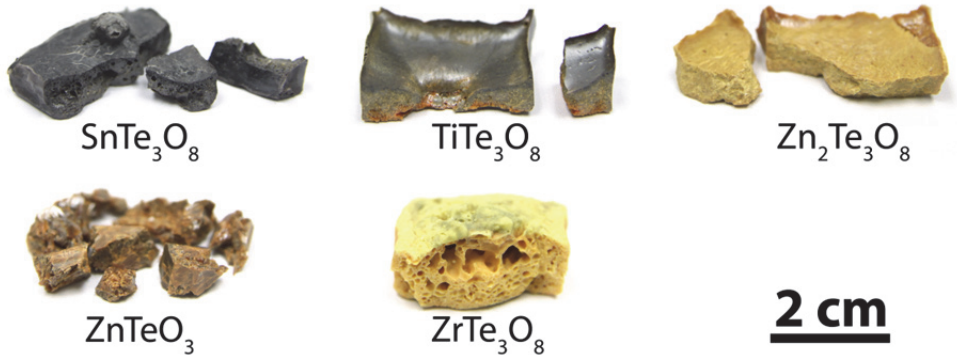

Figure 4.23. Pictures of the tellurite crystals fabricated in FY2011. The scale-bar is valid for all micrographs.

Table 4.12. Summary of crystalline phases identified in tellurite crystals.

Phase	PDF#	ICSD#	SG (SG#)	Reference
$SnTe_3O_8$	70-2440	9077	*Ia*-3 (206)	(Meunier and Galy, 1971)
$TiTe_3O_8$	70-2439	9076	*Ia*-3 (206)	(Meunier and Galy, 1971)
$ZnTeO_3$	44-0240	N/A	*Pbca* (61)	[a]
$ZnTeO_3$	72-1410	16937	*Pbca* (61)	(Hanke, 1967)
$Zn_2Te_3O_8$	89-4454	50705	*C*2/*c* (15)	(Feger et al., 1999)
$ZrTe_3O_8$	70-2442	9079	*Ia*-3 (206)	(Meunier and Galy, 1971)
SnO_2	70-6153	91517	*P*42/*mnm* (136)	(Kim et al., 2000)
SnO_2	41-1445	N/A	*P*42/*mnm* (136)	(McCarthy and Welton, 1989)
α-TeO_4	42-1365	27515	*P*41212 (92)	[b]
α-TeO_4	74-0269	25706	*P*41212 (92)	(Leciejewicz, 1961)
TiO_2	70-7347	93097	*P*42/*mnm* (136)	(Ballirano and Caminiti, 2001)
ZrO_2	89-9069	89429	*Fm*-3*m* (225)	(Wang et al., 1999)

[a] Rosenstingl, J., CH Hoffmann, E Irran, CH Lengauer, E Tillmanns, Vienna, Austria. ICDD Grant-in-Aid (1992)

[b] Information given in PDF card: Blanchard, F., Department of Geology, University of Florida, Gainesville (1990).

4.3.1 TeO_3-Isolated Crystals

The only crystal in this category that was made successfully was the $ZnTeO_3$ crystal, which we made as phase-pure because all of the diffraction peaks fit well to the ICSD standard in the database. The XRD pattern is presented in Figure 4.24. It is worth noting that this sample seemed to be the most brittle of the 5 that we made.

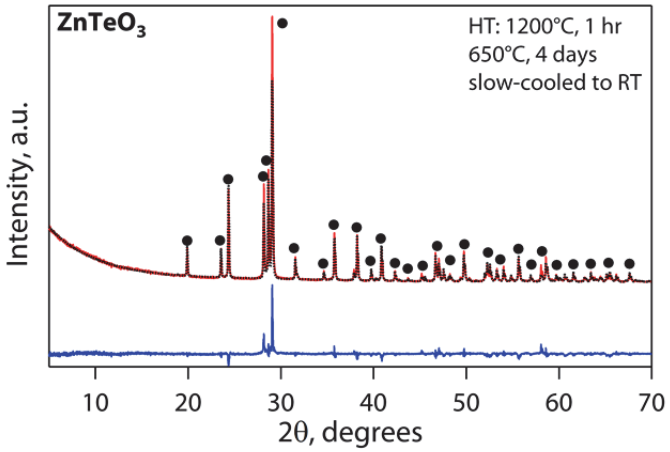

Figure 4.24. Rietveld refinement on $ZnTeO_3$ crystals showing the measured, calculated, and difference spectra. Here, ● represents the target phase ($ZnTeO_3$, PDF#72-1410, Table 4.12).

4.3.2 TeO_3-Terminal Crystals

The only crystal that was attempted in the class of TeO_3-terminal crystals was $Zn_2Te_3O_8$; this was achieved at high purity levels with minor impurities of what appeared to be the $ZnTeO_3$ phase. The Rietveld refinement of this pattern is presented in Figure 4.26.

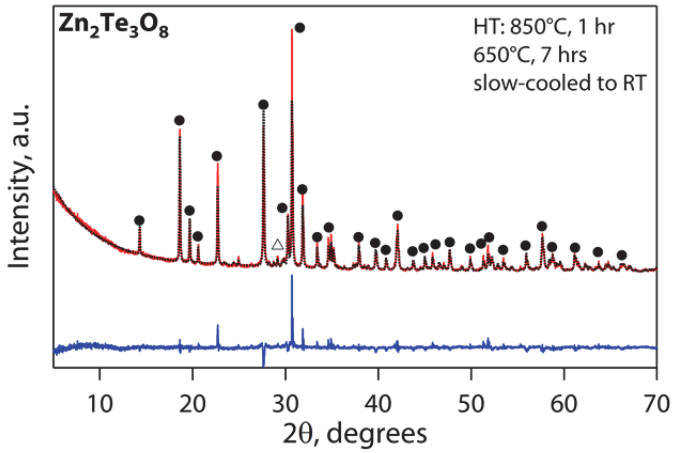

Figure 4.25. Rietveld refinement on $Zn_2Te_3O_8$ crystals showing the measured, calculated, and difference spectra. Here, ● represents the target phase ($Zn_2Te_3O_8$, PDF#89-4454) at 97.08 mass% and △ represents a minor impurity phase, $ZnTeO_3$ (PDF#75-1410) at 2.92 mass% (Table 4.12).

4.3.3 α-TeO_4 Tellurite Crystals

Three phases in this class of materials were investigated in FY2011: $ZrTe_3O_8$, $SnTe_3O_8$, and $TiTe_3O_8$. $SnTe_3O_8$ and $TiTe_3O_8$ were both heat-treated at 650°C for several days and did not melt, although they did result in relatively pure materials of the target compounds. However, the target goal was to melt the mixtures and fire them to both achieve phase-pure materials of the target composition and have particles large enough to size for chemical durability tests if they are sieved to isolate the larger particle sizes. Thus, high-temperature ($T > 900$°C) soaks were attempted prior to the lower temperature heat treatment for a long duration. These heat treatments did not always have the desired results; in some cases heat treatment at these higher temperatures resulted in a decrease of the target phase. For the $SnTe_3O_8$ and $TiTe_3O_8$ samples, the Rietveld refinements of the XRD data are presented in Figure 4.26.

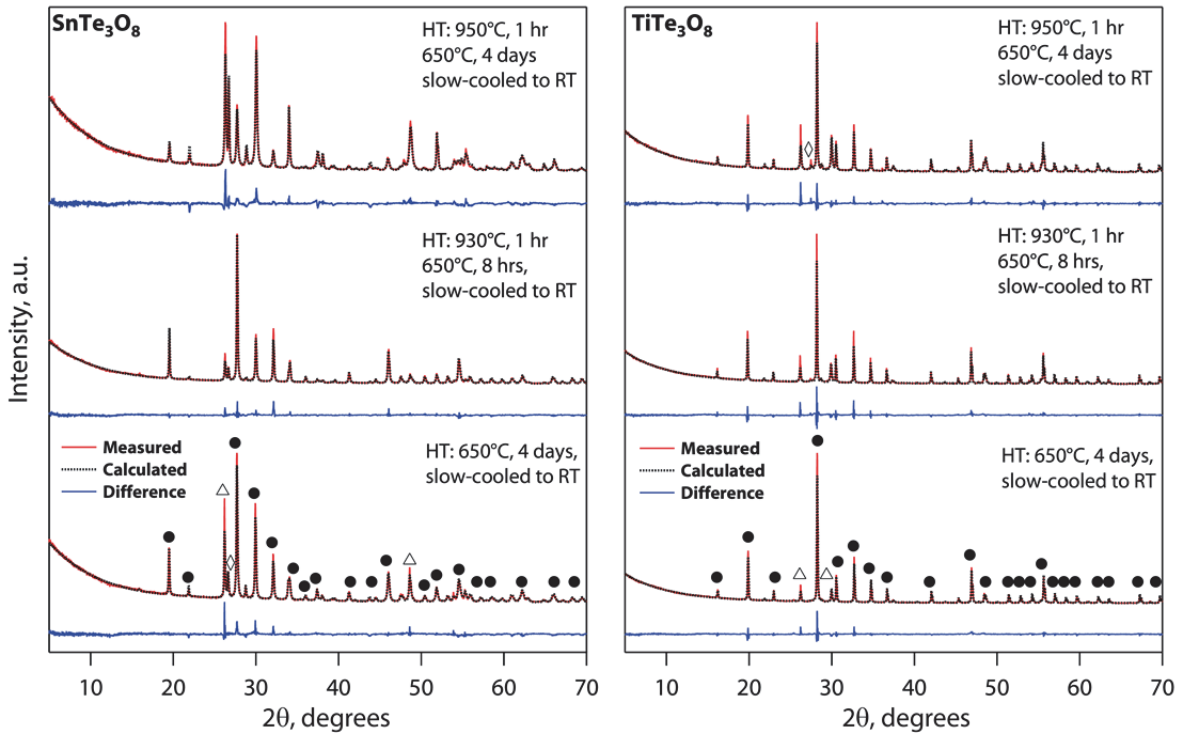

Figure 4.26. Rietveld refinement of XRD spectra for the $SnTe_3O_8$ (left) and $TiTe_3O_8$ (right) samples after various heat treatments. The samples were run sequentially from the bottom spectra toward the top spectra. Here, ● represents the target phases of $SnTe_3O_8$ (PDF#70-2440) and $TiTe_3O_8$ (PDF#70-2439), △ represents α-TeO_4 (PDF#42-1365), and ◊ represents the metal oxides of SnO_2 (PDF#70-6153) and TiO_2 (PDF#70-7347) in the corresponding figures (right and left, respectively) (see Table 4.12). The quantities of the constituents of these samples after each heat treatment are presented in Table 4.13.

Table 4.13. Mass% of components in $SnTe_3O_8$ and $TiTe_3O_8$ samples after Rietveld refinements. The phases correspond to phases in Table 4.12 with graphical representations in Figure 4.26. The temperatures correspond to the heat treatment temperatures.

	$SnTe_3O_8$			$TiTe_3O_8$		
Components	650°C	930°C	950°C	650°C	930°C	950°C
$SnTe_3O_8$	56.83	75.32	23.84	-	-	-
SnO_2	11.41	6.59	20.12	-	-	-
TeO_2	31.76	18.09	56.04	10.07	17.33	23.1
$TiTe_3O_8$	-	-	-	84.95	73.46	69.38
TiO_2	-	-	-	4.98	9.21	7.52

For the $ZrTe_3O_8$ sample, the single heat treatment at 950°C resulted in a very highly pure sample with only minor impurities of the unincorporated reactants. The Rietveld refinement of that sample is presented in Figure 4.27.

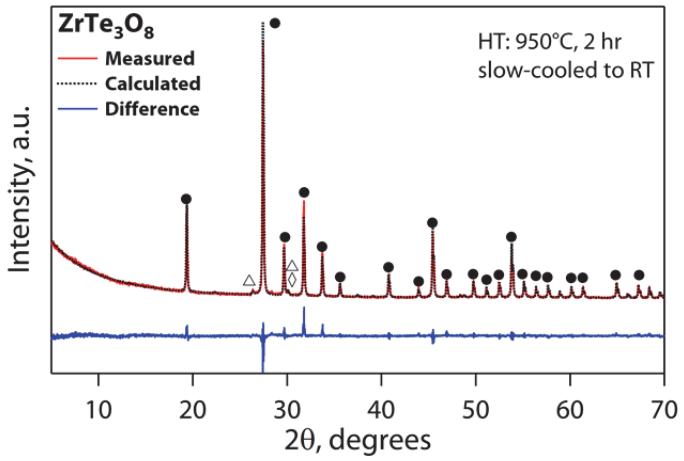

Figure 4.27. Rietveld refinement of XRD spectra for $ZrTe_3O_8$ after the 950°C heat treatment. Here, ● represents the target phase ($ZrTe_3O_8$, PDF#70-2442), △ represents α-TeO_4 (PDF#42-1365), and ◊ represents ZrO_2 (PDF#89-9069). Here, the $ZrTe_3O_8$ phase represents 97.21 mass% and TeO_2 represents 2.79 mass% of the crystalline content.

According to the results this far, it is apparent that it is possible to fabricate melted solids of highly pure tellurite crystals that can be used for chemical durability testing. This was a scoping test to see if it was possible to make solids of these crystals so they could be powdered after achieving phase-pure samples and then sized for chemical durability testing. These results show promise for further investigation in FY2012.

5 CONCLUSIONS

5.1 Tellurite Glasses

We performed several concurrent studies with the tellurite glass waste form in FY/CY2011. These studies included the following: 1) structural investigations on the P-series tellurite glasses from FY2010, 2) an expanded study on the lead-tellurite glasses that had high chemical durability in the FY2010 study, 3) a study on a series of glasses designed to reveal the glass-structural effects of anion/cation substitutions into the tellurite glass network, and 4) a study on the chemical durability of tellurite crystals with known crystal structure and tellurium-oxygen coordination.

Study 1 – *Compositional variation glasses*. In this study, which was the ground work for Study 2, we learned the various interpretations of the diverse set of Raman spectra observed in tellurite glasses. We measured the Raman spectra for all 10 of the P-series glasses that were analyzed with the PCT. The primary goal of the structural interrogation of the P-series glasses was to see whether we could find a correlation between the tellurium-oxygen coordination environment and the chemical durability, considering that the chemical durability of these glasses was so diverse. However, we failed to find a simple correlation.

Study 2 – *Lead-tellurite variation glasses*. A series of TeO_2-PbO glasses were fabricated with various amounts of a mixed chloride waste simulant (nonradioactive) intended to represent the EChem waste stream from the electrochemical process used for reprocessing of nuclear fuel. The structure of these glasses was studied with Raman spectroscopy and X-ray diffraction, and indicated that the medium-range order in the glass decreased and the tellurite network was depolymerized as the waste fraction was increased. It was apparent that glass network-breaking was predominantly caused by the additions of the waste cations and that the presence of chloride may have actually caused some repolymerization of the network by scavenging alkali and preventing it from acting as a network modifier. At the highest waste loadings the glass became phase-separated, resulting in a Te-rich phase and a alkali-chloride-rich phase, and some chloride-containing crystals were formed.

Study 3 – *Structural variation glasses*. A series of glasses were designed to investigate the glass structural effects when select species in the glasses from Study 1 and Study 2 were substituted for other species. The aim of these studies was to better understand the difference between the roles of the cations and anions from both the lead and the XCl_{20} components. We looked at (1) lead-tellurite glasses with K_2O or KCl, (2) a lead-tellurite glass in which XCl_{20} components were substituted for XO_{20} components ("X" cation ratios to Te and Pb retained from the TPb_5 glass), and (3) some lead-tellurite glasses in which $PbCl_2$ was substituted for PbO. Structural analysis on these glasses indicated that the chloride in XCl_{20} actually *repolymerizes* the tellurite network compared to the oxygen in the XO_{20} glass with the same modifier cations, by scavenging some of the alkali into a separate phase that is ultimately present as nano-phase-separated droplets at the highest XCl_{20}-loadings. This local removal of alkali from the role of network modifier of the tellurite network, even in the low waste loading glasses devoid of visible phase separation, is believed to be the mechanism responsible for preventing formation of some *tp* units indicative of depolymerization. The comparison of the K_2O and KCl glasses having the same relative amount of K compared to Te and Pb indicated the same trend, i.e., that the chloride-containing glass is slightly more polymerized than the one without chloride when both contain the same relative amount of alkali to the main glass formers.

Study 4 – *Tellurite crystals*. A study on tellurite crystals was identified in the literature as a potentially valuable contribution to our work. In this study, a wide range of binary and ternary Te-O crystals were made and categorized into groups in which the structures were composed of either TeO_3, TeO_{3+1}, α-TeO_4, or β-TeO_4 Te-O structural units. The primary goal of pursuing these was to make a few of the crystals in each "category" and test the chemical durability of the crystals. If one of these structural units is preferred for high chemical durability, then since the crystals are composed of a single structural unit throughout, crystals from certain categories may show better chemical durability than others. We

successfully made five crystals, some of them nearly phase-pure. We plan to continue to pursue this path and, hopefully, assess the chemical durability of these materials in CY2012.

5.2 Halide Minerals

In order to improve upon our results from past years on solution-derived sodalites, we made some changes to the process in FY/CY2011. These changes included the following: (1) replacing CS with TEOS as the silica source in the process, (2) replacing Si with Ge in the sodalite with germanium (IV) ethoxide, and (3) optimizing the sintering aid for low-temperature firing to reduce chloride volatility and maximize sodalite production.

Study 1 – *Organic silica source*. We replaced the CS with TEOS as the silica source in the process to see whether it altered the reaction rate, allowing for a higher concentration of sodalite in the dried product (90°C). The change was a noticeable improvement for the dried product from 76 mass% sodalite in the S5A specimens with CS to ≤96 mass% sodalite in the S5C specimen with TEOS.

Study 2 – *Organic germania source*. Here, we wanted to look at an organic source of germania as a replacement for silica, i.e., germanium (IV) ethoxide. The primary goal of this substitution was that we predicted that the germania-based gel, when pressed into pellets, would sinter at a lower temperature and that would reduce the Cl volatility and increase the density of the fired pellets for a higher volumetric waste loading. The drawback with exchanging Si for Ge is the increased costs associated with Ge. However, we wanted to explore this potential option. The high porosity in the initially fired pellets was a deterrent to pursuing this route any farther, though we did demonstrate a high germania-based sodalite concentration (82 mass%) in the as-made gel.

Study 3 – *Alternative sintering aids*. Here, we investigated alternative glass-binders to the NBS-1 glass. Since the viscosity of the NBS-1 glass is so high, the temperatures required for pellet densification were rather high (950°C) and that led to chloride volatility, evidenced by a decrease in the sodalite concentration. In order to reduce the sintering temperatures, six alternative sintering aids were fabricated and added to the solution during the process. These sintering aids included four sodium borosilicate formulations, a sodium aluminophosphate formulation, and a lead-tellurite glass formulation (TPb_0). These samples were dried, pressed into pellets, fired at different temperatures, and the phases quantified. The sodium borosilicate glasses proved to dramatically improve the densification, (up to 96% of theoretical density for sodalite), of the fired pellets at much-reduced temperatures of ~750°C, where rather large amounts of sodalite were still produced (71 mass%). We will continue to improve the process in CY2012.

In addition to adding a sintering aid to help consolidate the materials, we will be investigating alternative sintering techniques that include pressure control in order to maintain the stability of the sodalite structure. This will provide the ability to reduce porosity and increase density. We propose using spark-plasma sintering because it has high pressure capability plus the added benefit of voltage, which promotes grain bonding, resulting in reduced surface area. The spark-plasma sintering process is also rapid, <1 hr, compared to traditional sintering which takes 10 to 24 hrs and this reduced heat-treatment time is expected to reduce chloride volatility.

6 ACKNOWLEDGEMENTS

Authors would like to thank the U.S. Department of Energy, Office of Nuclear Energy for their support of this work under Contract Number DE-AC05-76RL01830. Authors thank Ashutosh Goel and Loni Peurrung for helpful review of this document, James Bresee (DOE Office of Nuclear Energy) and Terry Todd (Idaho National Laboratory) for project oversight. The authors greatly thank Laura Buchanan for her hard work in making sure that the schedule and performance of milestones and monthly reports were carefully tracked, Teresa Schott for administrative support, and Maura Zimmerschied for her help with the manuscript.

7 REFERENCES

Akagi, R, K Handa, N Ohtori, AC Hannon, M Tatsumisago, and N Umesaki. 1999. "High-temperature structure of K_2O-TeO_2 glasses." *Journal of Non-Crystalline Solids* 256&257:111-18.

Arnaudov, M and Y Dimitriev. 2001. "Study on the structural transition in binary tellurite glasses by means of reduced infrared spectra." *Physics and Chemistry of Glasses* 42(2):99-102.

Arnaudov, M, V Dimitrov, Y Dimitriev, and L Markova. 1982. "Infrared-spectral investigation of tellurites." *Materials Research Bulletin* 17(9):1121.

Ballirano, P and R Caminiti. 2001. "Rietveld refinements on laboratory energy dispersive X-ray diffraction (EDXD) data." *Journal of Applied Crystallography* 34(6):757-62.

Barrett, WT and WE Wallace. 1954. "Studies of NaCl-KCl solid solutions. I. Heats of formation, lattice spacings, densities, Schottky defects and mutual solubilities." *Journal of the American Chemical Society* 76(2):366-69.

Bateman, KJ, CJ Knight, and CW Solbrig. 2007. *Current Status of Ceramic Waste Form Development*. Report No. INL/INT-06-11736, Rev. 1, Idaho National Laboratory, Idaho Falls, ID.

Beagley, B, CMB Henderson, and D Taylor. 1982. "The crystal structures of aluminoslicate-sodalites: X-ray diffraction studies and computer modelling." *Mineralogical Magazine* 46:459-64.

Beyer, H. 1967. "Verfeinerung der kristallstruktur von tellurit, dem rhombischen TeO_2." *Kristallografiya* 124:228-38.

Bhat, MH, M Kandavel, M Ganguli, and KJ Rao. 2004. "Li^+ ion conductivities in boro-tellurite glasses." *Bulletin of Materials Science* 27(2):189-98.

Brady, GW. 1957. "Structure of tellurium oxide glass." *Journal of Chemical Physics* 27(1):300-03.

Brady, GW. 1956. "X-ray study of tellurium oxide glass." *Journal of Chemical Physics* 24(2):477-78.

Brow, RK, DR Tallant, and GL Turner. 1997. "Polyhedral arrangements in lanthanum aluminoborate glasses." *Journal of the American Ceramic Society* 80(5):1239-44.

Bürger, H, K Kneipp, H Hobert, W Vogel, V Kozhukharov, and S Neov. 1992. "Glass formation, properties and structure in the TeO_2-ZnO system." *Journal of Non-Crystalline Solids* 151:134-42.

Chowdari, BVR and PP Kumari. 1999. "Raman spectroscopic study of ternary silver tellurite glasses." *Materials Research Bulletin* 34(2):327-42.

Crum, JV, BJ Riley, SK Sundaram, SA Arreguin, J Matyas, MJ Schweiger, BT Rieck, and JD Vienna. 2009. *Alternative Waste Forms for Electro-Chemical Salt Waste*. Report No. AFCI-WAST-PMO-MI-DV-2009-000293, Pacific Northwest National Laboratory, Richland, WA.

Darriet, J and J Galy. 1973. *Acta Crystallographica* C2:237-43.

Darriet, J, G Guillaume, K-A Wilhelmi, and J Galy. 1972. "Etude des composés $MVTeO_5$ (M = Na, K, Rb, Ag). Structure cristalline de $NaVTeO_5$." *Acta Chemica Scandinavica* 26:59-70.

Dimitriev, Y, V Dimitrov, E Gatev, E Kashchieva, and H Petkov. 1987. "Effect of the mode formation on the structure of tellurite glasses." *Journal of Non-Crystalline Solids* 95-96(2):937-44.

Dimitriev, Y, E Kashchieva, I Ivanova, and D Khristova. 1983. "Liquation in three-component tellurite systems TeO_2-B_2O_3-M_nO_m. M_nO_m=Al_2O_3, Ga_2O_3, Cr_2O_3, CuO, Ag_2O, MoO_3, Sb_2O_3." *Stroit. Mater. Silikat. Prom.* 24(9):24.

Donald, IW, BL Metcalfe, SK Fong, LA Gerrard, DM Strachan, and RD Scheele. 2007. "A glass-encapsulated calcium phosphate wasteform for the immobilization of actinide-, fluoride-, and chloride-containing radioactive wastes from the pyrochemical reprocessing of plutonium metal." *Journal of Nuclear Materials* 361(1):78-93.

Dong, Z, TJ White, B Wei, and K Laursen. 2002. "Model apatite systems for the stabilization of toxic metals: I, calcium lead vanadate." *Journal of the American Ceramic Society* 85(10):2515-22.

Duverger, C, M Bouazaoui, and S Turrell. 1997. "Raman spectroscopic investigations of the effect of the doping metal on the structure of binary tellurium-oxide glasses." *Journal of Non-Crystalline Solids* 220(2-3):169-77.

Ebert, WL. 2005. *Testing to Evaluate the Suitability of Waste Forms Developed for Electrometallurgically-Treated Spend Sodium-Bonded Nuclear Fuel for Disposal in the Yucca Mountain Repository*. Report No. ANL-05/43, Argonne National Laboratory-East, Argonne, IL.

Ebert, WL and SF Wolf. 1999. *Round-Robin Testing of a Reference Glass for Low-Activity Waste Forms*. Report No. ANL-99/22, Argonne National Laboratory, Argonne, Illinois.

Ewing, RC, WJ Weber, and J Clinard, F.W. 1995. "Radiation effects in nuclear waste forms for high-level radioactive waste." *Progress in Nuclear Energy* 29(2):63-127.

Feger, CR, GL Schimek, and JW Kolis. 1999. "Hydrothermal synthesis and characterization of $M_2Te_3O_8$ (M=Mn, Co, Ni, Cu, Zn): a series of compounds with the spiroffite structure." *Journal of Solid State Chemistry* 143(2):246-53.

Fleet, ME. 1989. "Structures of sodium alumino-germanate sodalites [$Na_8(Al_6Ge_6O_{24})A_2$, A = Cl, Br, I]." *Acta Crystallographica* C45(6):843-47.

Folger, F. 1975a. "Die Kristallstruktur von $BaTeO_3$." *Journal of Inorganic and General Chemistry* 411(2):111-17.

Folger, F. 1975b. "Die Kristallstruktur von Li_2TeO_3." *Journal of Inorganic and General Chemistry* 411(2):103-10.

Foreman, N and DR Peacor. 1970. "Refinement of the nepheline structure at several temperatures." *Journal of Solid State - New Crystal Structures* 132(1-6):45-70.

Frit, B, B Holmberg, and J Galy. 1970. "Structure cristalline de l'oxychlorure de baryum, Ba_4OCl_6." *Acta Crystallographica* B26(1):16-19.

Hanke, K. 1966. "Die kristallstruktur von $Zn_2Te_3O_8$." *Naturwissenschaften* 53(11):273.

Hanke, K. 1967. "Zinktellurit: kristallstruktur und beziehungen zu einigen seleniten." *Naturwissenschaften* 54(8):199.

Hartenbach, I and T Schleid. 2001. "Zwei Chloridsilicate des Yttriums: $Y_3Cl(SiO_4)_2$ und $Y_6Cl_{10}(Si_4O_{12})$." *Journal of Inorganic and General Chemistry* 627(11):2493-98.

Haynes, WM, ed. Y-R Luo. 2011. *CRC Handbook of Chemistry and Physics*. 91st Ed., CRC Press/Taylor and Francis, Boca Raton, FL.

Heo, J, D Lam, GH Sigel, EA Mendoza, and DA Hensley. 1992. "Spectroscopic analysis of the structure and properties of alkali tellurite glasses." *Journal of the American Ceramic Society* 75(2):277-81.

Hesse, K-F. 1977. "Refinement of the crystal structure of lithium polysilicate." *Acta Crystallographica* B33(3):901-02.

Himei, Y, A Osaka, T Nanba, and Y Miura. 1994. "Coordination change of Te atoms in binary tellurite glasses." *Journal of Non-Crystalline Solids* 177:164-69.

Hocdé, S, SB Jiang, X Peng, N Peyghambarian, T Luo, and M Morrell. 2004. "Er^{3+} doped boro-tellurite glasses for 1.5 µm broadband amplification." *Optical Materials* 25(2):149-56.

Hruby, A. 1972. "Evaluation of glass-forming tendency by means of DTA." *Czechoslovak Journal of Physics, Section B* 22(11):1187-93.

Iwadate, Y, H Kenmotsu, T Hattori, S Nishiyama, K Fukushima, N Umesaki, T Nakazawa, and K Noda. 2000. "X-ray diffraction study of the short-range structure of LiCl-Li_2O-TeO_2 glasses." *Journal of Alloys and Compounds* 305:130-35.

Jacobson, AJ, BC Tofield, and BEF Fender. 1972. "The structures of $BaCeO_3$, $BaPrO_3$ and $BaTbO_3$ by neutron diffraction: lattice parameter relations and ionic radii in *O*-perovskites." *Acta Crystallographica* B28(3):956-61.

Kashchieva, E. 1984. "Phase separation in tellurite systems." Sofia University, Sofia, Bulgaria: Thesis.

Kendrick, E and S Dann. 2004. "Synthesis, properties and structure of ion exchanged hydrosodalite." *Journal of Solid State Chemistry* 177(4-5):1513-19.

Khatir, S, F Romain, J Portier, S Rossignol, B Tanguy, JJ Videau, and S Turrell. 1993. "Raman studies of recrystallized glasses in the binary TeO_2-PbO system." *Journal of Molecular Structure* 298:13-16.

Kim, Y-I, M-J Jung, and KH Kim. 2000. "Application of inverse pole figure to Rietveld refinement: III. Rietveld refinement of SnO_2 thin film using X-ray diffraction data." *Korean Journal of Ceramics* 6(4):354-58.

Knop, O and G Demazeau. 1981. "The 1-6 weberite $Na_2Te_2O_7$ and some observations on compounds with the weberite structure." *Journal of Solid State Chemistry* 39(1):94-99.

Kondratyuk, IP, LA Muradyan, YV Pisarevskii, and VI Simonov. 1987. "Precision X-ray structure investigation of acoustooptical single crystals of α-TeO_2." *Kristallografiya* 32(3):354-59.

Kozhukharov, V, H Burger, S Neov, and B Sidzhimov. 1986. "Atomic arrangement of a zinc-tellurite glass." *Polyhedron* 5(3):771-77.

Kozhukharov, VS, MR Marinov, and JN Pavlova. 1978. "Phase equilibria and immiscibility in the TeO_2-P_2O_5 system." *Journal of Materials Science* 13(5):997-1005.

Kulcu, N. 1987. "Some new metastable compounds with a defect-type calcium fluoride (CaF_2) structure." *Doga: Turk Kimya Dergisi* 11(1):27-31.

Lacks, DJ and RG Gordon. 1993. "Crystal-structure calculations with distorted ions." *Physical Review B* 48(5):2889-908.

Leciejewicz, J. 1961. "The crystal structure of tellurium dioxide. A redetermination by neutron diffraction." *Journal of Solid State - New Crystal Structures* 116(3-6):345-53.

Levenberg, K. 1944. "A method for the solution of certain problems in least squares." *Quart. Appl. Math* 2:164-68.

Li, H, P Hrma, JD Vienna, M Qian, Y Su, and DE Smith. 2003. "Effects of Al_2O_3, B_2O_3, Na_2O, and SiO_2 on nepheline formation in borosilicate glasses: chemical and physical correlations." *Journal of Non-Crystalline Solids* 331(1-3):202-16.

Lindner, G-G, W Massa, and D Reinen. 1995. "Structure and properties of hydrothermally synthesized thiosulfate cancrinite." *Journal of Solid State Chemistry* 117(2):386-91.

Lindqvist, O. 1968. "Refinement of the structure of α-TeO_2." *Acta Chemica Scandinavica* 22:977-82.

Liu, Q, A Navrotsky, CF Jove-Colon, and F Bonhomme. 2007. "Energetics of cancrinite: effect of salt inclusion." *Microporous and Mesoporous Materials* 98(1-3):227-33.

Loopstra, BO and K Goubitz. 1986. "The structures of four caesium tellurates." *Acta Crystallographica* C42(5):520-23.

Mazzuca, M, J Portier, B Tanguy, F Romain, A Fadli, and S Turrell. 1995. "Raman scattering in tellurium-metal oxyde glasses." *Journal of Molecular Structure* 349:413-16.

McCarthy, GJ and JM Welton. 1989. "X-Ray diffraction data for SnO_2. An illustration of the new powder data evaluation methods." *Powder Diffraction* 4(3):156-59.

Meier, WM. 1973. "Symmetry Aspects of Zeolite Frameworks." In *Molecular Sieves: Pt. 1 (Advances in Chemistry Series)*, eds. WM Meier and JB Uytterhoeven, Vol 121, pp. 39-51. Schweizerische Chemische Gesellschaft, Bern, Switzerland.

Meunier, G and J Galy. 1971. "Sur une déformation inédite du reseau de type fluorine. Structure cristalline des phases $M Te_3O_8$ (M = Ti, Sn, Hf, Zr)." *Acta Crystallographica* B27:602-08.

Meyer, G, J Soose, A Moritz, V Vitt, and TH Holljes. 1985. "Ternaere Halogenide der seltenen Erden vom Typ A_2MX_5. (A=K, In, NH_4, Rb, Cs; X=Cl, Br, I)." *Journal of Inorganic and General Chemistry* 521:161-72.

Mineralogy Database. 2011. Accessed 2009-2011 at http://www.webmineral.com/ (last updated 10/01/2011).

Moller, CK. 1957. "A phase transition in caesium plumbochloride." *Nature* 180(4593):981-82.

Murugan, GS, T Suzuki, and Y Ohishi. 2005. "Phospho-tellurite glasses containing heavy metal oxides for ultrabroad band fiber Raman amplifiers." *Applied Physics Letters* 86(22):221109-1-3.

Murugan, GS, T Suzuki, and Y Ohishi. 2006. "Raman characteristics and nonlinear optical properties of tellurite and phosphotellurite glasses containing heavy metal oxides with ultrabroad Raman bands." *Journal of Applied Physics* 100(2):023107-1 - 07-6.

Neov, S, I Gerassimova, K Krezhov, B Sydzhimov, and V Kozhukharov. 1978. "Atomic arrangement in tellurite glasses studied by neutron diffraction." *physica status solidi (a)* 47(2):743-50.

Neov, S, V Kozhukharov, I Gerasimova, K Krezhov, and B Sidzhimov. 1979. "A model for structural recombination in tellurite glasses." *Journal of Physics C: Solid State Physics* 12(13):2475-85.

Nishida, T, M Yamada, H Ide, and Y Takashima. 1990. "Correlation between the structure and glass transition temperature of potassium, magnesium and barium tellurite glasses." *Journal of Materials Science* 25(8):3546-50.

Ocanto, F, R Alvarez, CU de Navarro, A Lieb, and CF Linares. 2008. "Influence of the alkalinity and NO_3^-/Cl^- anionic composition on the synthesis of the cancrinite-sodalite system." *Microporous and Mesoporous Materials* 116(1-3):318-22.

Ocanto, F, E Figueredo, M Brikgi, CUd Navarro, and CF Linares. 2009. "Oxidation-reduction reactions: a novel method in the synthesis of nitrate cancrinite-type zeolites." *Materials Letters* 63(1):11-14.

Ott, H. 1923. "Die raumgitter der lithiumhalogenide." *Physikalische Zeitschrift* 24:209-13.

Park, H-S, I-T Kim, H-Y Kim, K-S Lee, S-K Ryu, and J-H Kim. 2002. "Application of Apatite Waste Form for the Treatment of Water-Soluble Wastes Containing Radioactive Elements. Part I: Investigation on the Possibility." *Journal of Industrial and Engineering Chemistry* 8(4):318-27.

Patnaik, P. 2003. *Handbook of Inorganic Chemicals*, McGraw-Hill, New York.

Rada, S, M Culea, and E Culea. 2008. "Structure of TeO_2-B_2O_3 glasses inferred from infrared spectroscopy and DFT calculations." *Journal of Non-Crystalline Solids* 354(52-54):5491-95.

Rao, KJ and MH Bhat. 2001. "Investigation of lithium chloride-lithium borate-tellurium dioxide glasses: an example of complex anionic speciation." *Physics and Chemistry of Glasses - European Journal of Glass Science and Technology Part B* 42(3):255-64.

Riley, BJ, BT Rieck, JV Crum, J Matyas, J McCloy, SK Sundaram, and JD Vienna. 2010. *Alternative Electrochemical Salt Waste Forms, Summary of FY2010 Results*. Report No. FCRD-WAST-2010-000129, Pacific Northwest National Laboratory, Richland, WA.

Rojo, JM, J Sanz, JM Reau, and B Tanguy. 1990. "Influence of ion distribution on the ionic conductivity of lithium tellurite glasses (Li_2O-TeO_2 and LiF-TeO_2)." *Journal of Non-Crystalline Solids* 116(2-3):167-74.

Rong, QJ, A Osaka, T Nanba, J Takada, and Y Miura. 1992. "Infrared and Raman spectra of binary tellurite glasses containing boron and indium oxides." *Journal of Materials Science* 27(14):3793-98.

Sakida, S, S Hayakawa, and T Yoko. 2001. "^{125}Te, ^{27}Al, and ^{71}Ga NMR Study of M_2O_3–TeO_2 (M = Al and Ga) Glasses." *Journal of the American Ceramic Society* 84(4):836-42.

Sakida, S, S Hayakawa, and T Yoko. 1999a. "Part 1. ^{125}Te NMR study of tellurite crystals." *Journal of Non-Crystalline Solids* 243(1):1-12.

Sakida, S, S Hayakawa, and T Yoko. 1999b. "Part 2. ^{125}Te NMR study of M_2O-TeO_2 (M = Li, Na, K, Rb and Cs) glasses." *Journal of Non-Crystalline Solids* 243(1):13-25.

Sciau, P, J Lapasset, and J Moret. 1986. "Structure de la phase quadratique de $PbTeO_3$." *Acta Crystallographica* C42(12):1688-90.

Seemann, H. 1956. "Die kristallstruktur des lithiummetasilikates, $(Li_2SiO_3)_x$." *Acta Crystallographica* 9(3):251-52.

Sekiya, T, N Mochida, and S Ogawa. 1994a. "Structural study of WO_3-TeO_2 glasses." *Journal of Non-Crystalline Solids* 176(2-3):105-15.

Sekiya, T, N Mochida, and A Ohtsuka. 1994b. "Raman spectra of MO-TeO_2 (M = Mg, Sr, Ba and Zn) glasses." *Journal of Non-Crystalline Solids* 168(1-2):106-14.

Sekiya, T, N Mochida, A Ohtsuka, and A Soejima. 1992a. "Raman spectra of $BO_{3/2}$-TeO_2 glasses." *Journal of Non-Crystalline Solids* 151(3):222-28.

Sekiya, T, N Mochida, A Ohtsuka, and M Tonokawa. 1992b. "Raman spectra of $MO_{1/2}TeO_2$ (M = Li, Na, K, Rb, Cs and Tl) glasses." *Journal of Non-Crystalline Solids* 144:128-44.

Shimizugawa, Y, T Maeseto, S Suehara, S Inoue, and A Nukui. 1995. "EXAFS and RDF studies of TeO_2-Li_2O glasses." *Journal of Materials Research* 10(2):405-10.

Silva, MAP, Y Messaddeq, SJL Ribeiro, M Poulain, F Villain, and V Briois. 2001. "Structural studies on TeO_2-PbO glasses." *Journal of Physics and Chemistry of Solids* 62(6):1055-60.

Standard density and volumetric tables. 1924. 6th ed., United States National Bureau of Standards Government Printing Office, Washington.

ASTM C 1285-02. 2002. *Standard Test Methods for Determining Chemical Durability of Nuclear, Hazardous, and Mixed Waste Glasses and Multiphase Glass Ceramics: The Product Consistency Test (PCT)*, American Society for Testing and Materials International, West Conshohocken, PA.

Tanaka, K, T Yoko, H Yamada, and K Kamiya. 1988a. "Structure and ionic conductivity of LiCl-Li_2O-TeO_2 glasses." *Journal of Non-Crystalline Solids* 103:250-56.

Tanaka, K, T Yoko, H Yamada, and K Kamiya. 1988b. "Structure and ionic conductivity of LiCl-Li_2O-TeO_2 glasses." *Journal of Non-Crystalline Solids* 103(2-3):250-56.

Tatar, D, G Özen, FB Erim, and ML Öveçoğlu. 2010. "Raman characterizations and structural properties of the binary TeO_2-WO_3, TeO_2-CdF_2 and ternary TeO_2-CdF_2-WO_3 glasses." *Journal of Raman Spectroscopy* 41(7):797-807.

Tatsumisago, M, S-K Lee, T Minami, and Y Kowada. 1994. "Raman spectra of TeO_2-based glasses and glassy liquids: local structure change with temperature in relation to fragility of liquid." *Journal of Non-Crystalline Solids* 177(1):154-63.

Thompson, JG, RL Withers, A Melnitchenko, and SR Palethorpe. 1998. "Cristobalite-related phases in the $NaAlO_2$-$NaAlSiO_4$ system. I. Two tetragonal and two orthorhombic structures." *Acta Crystallographica* B54(5):531-46.

Tromel, M and H Ziethen-Reichnach. 1970. "Magnesiumtellurite." *Journal of Inorganic and General Chemistry* 378(3):238-44.

Vienna, J. 2010. "Nuclear waste vitrification in the United States: recent developments and future options." *Inernational Journal of Applied Glass Science* 1(3):309-231.

Vienna, JD, J Luey, PR Hrma, DE Smith, RD Scheele, HL Wigent, and JV Crum. 1998. Glass frit development for encapsulation of rocky flats ash. Presented at *Environmental Issues and Waste Management Technologies in the Ceramic and Nuclear Industries IV*, Vol. 93, 399-407 pp., The American Ceramics Society, Westerville, OH.

Vogel, W, H Burger, G Zerge, B Muller, K Forkel, G Winterstein, A Boxberger, and H Romhild. 1974. "Halogenid- und sulfathaltige telluritglaser." *Silikattechnik* 25(6):207-08.

Wang, D-N, Y-Q Guo, K-M Liang, and K Tao. 1999. "Crystal structure of zirconia by Rietveld refinement." *Science in China - Series A: Mathematics, Physics, Astronomy & Technological Sciences* 42(1):80-86.

Wang, JS, EM Vogel, and E Snitzer. 1994. "Tellurite glass: a new candidate for fiber devices." *Optical Materials* 3(3):187-203.

Weber, WJ, RP Turcotte, LR Bunnell, FP Roberts, and JH Westsik. 1979. "Radiation effects in vitreous and devitrified smulated waste glass." In *Ceramics in Nuclear Waste Management*, eds. TD Chikalla and JE Mendel, pp. 294-99. National Technical Information Service, Springfield, VA.

Withers, RL and JG Thompson. 1993. "Modulation wave approach to the structural parameterization and Rietveld refinement of low carnegieite." *Acta Crystallographica* B49(4):614-26.

Yakhkind, AK and SA Chebotarev. 1980. "Glass formation, crystallization ability, density and thermal expansion of glasses in ternary tellurite halogen systems." *Fizika i Khimiya Stekla* 6(2):164-69.

Yamamoto, H, H Nasu, J Matsuoka, and K Kamiya. 1994. "X-ray absorption fine structure (XAFS) study on the coordination of Te in PbO-TiO_2-TeO_2 glasses with high third-order optical non-linearity " *Journal of Non-Crystalline Solids* 170(1):87-96.

Yoo, TS. 2009. "Personal Communication by electronic mail."

Zachariasen, WH. 1929. "The crystal structure of sodium chlorate." *Journal of Solid State - New Crystal Structures* 71(5-6):517-29.

Zaslavsky, AI, D Kondrashev, and S Tolkachev. 1950. "The new modification of lead dioxide and the texture of anode sediments." *Doklady Akademii Nauk SSSR* 75:559-61.

Appendix A: Comparison of XCl_y Used for Tellurite Glass Al/B+Cl (P-2)

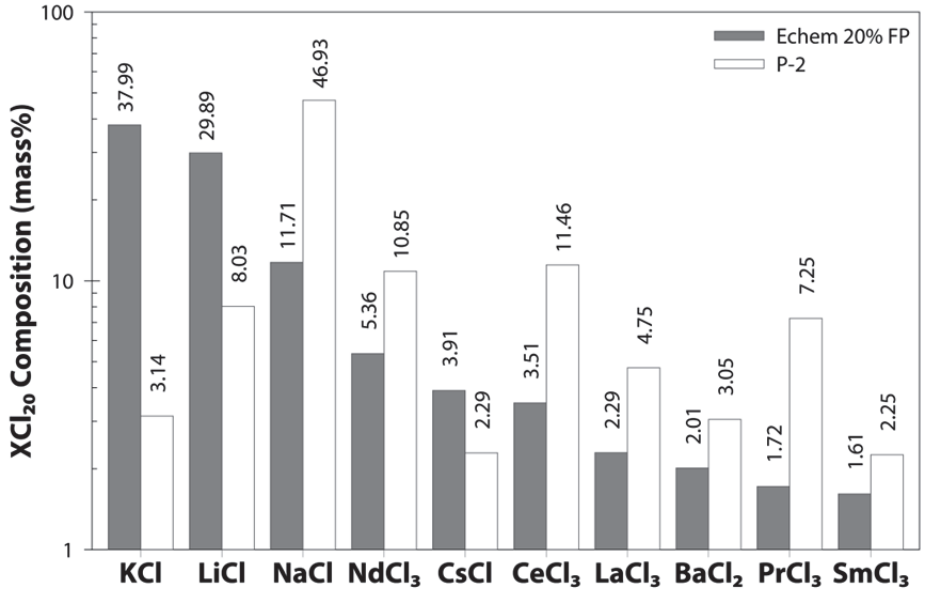

Figure A.1. Comparative plot showing the difference between the correct ("Echem 20% FP" or XCl_{20}) (dark bars) and incorrect ("P-2") waste stream (light bars) used for batching Glass P-2, the Al_2O_3-B_2O_3 glass with 10% mixed chlorides (XCl_y).

Appendix B: Peak Fits and Rietveld Refinements for Sodalite Samples

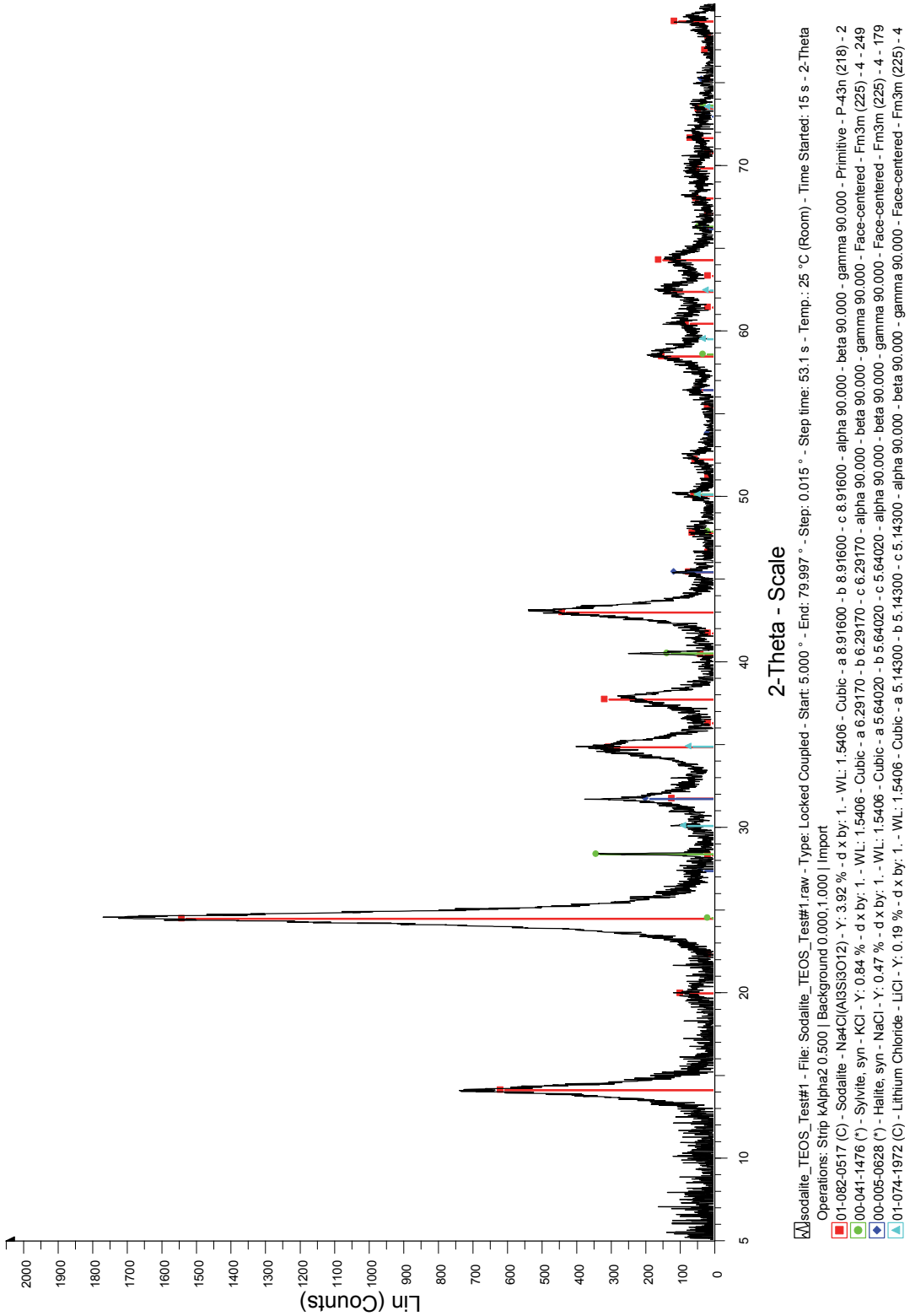

Figure B.1. Peak fitting for S5C (TEOS), unfired.

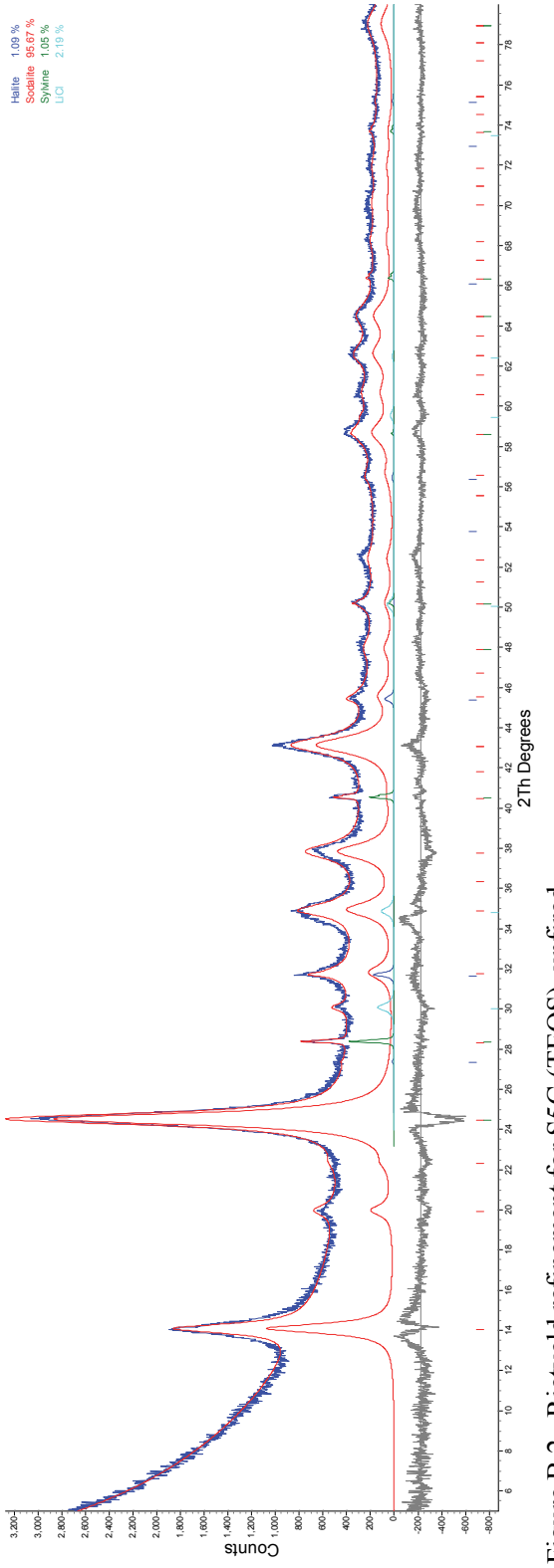

Figure B.2. Rietveld refinement for S5C (TEOS), unfired.

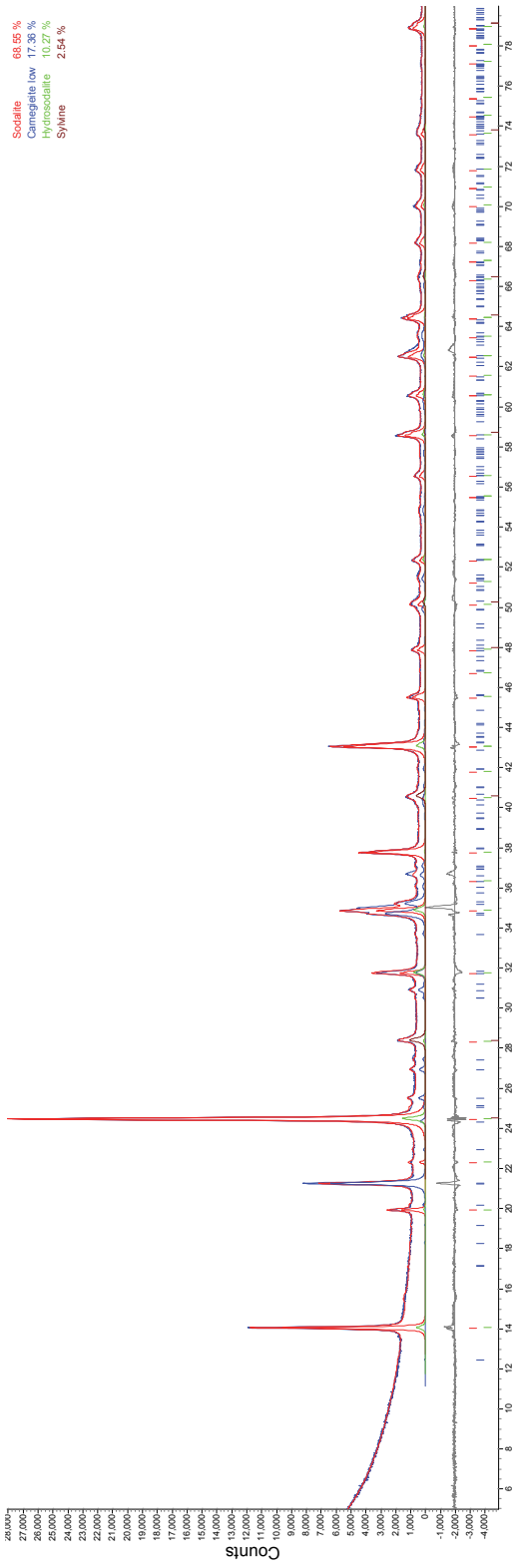

Figure B.3. Rietveld refinement for S5C (TEOS), fired at 750°C for 8 hrs.

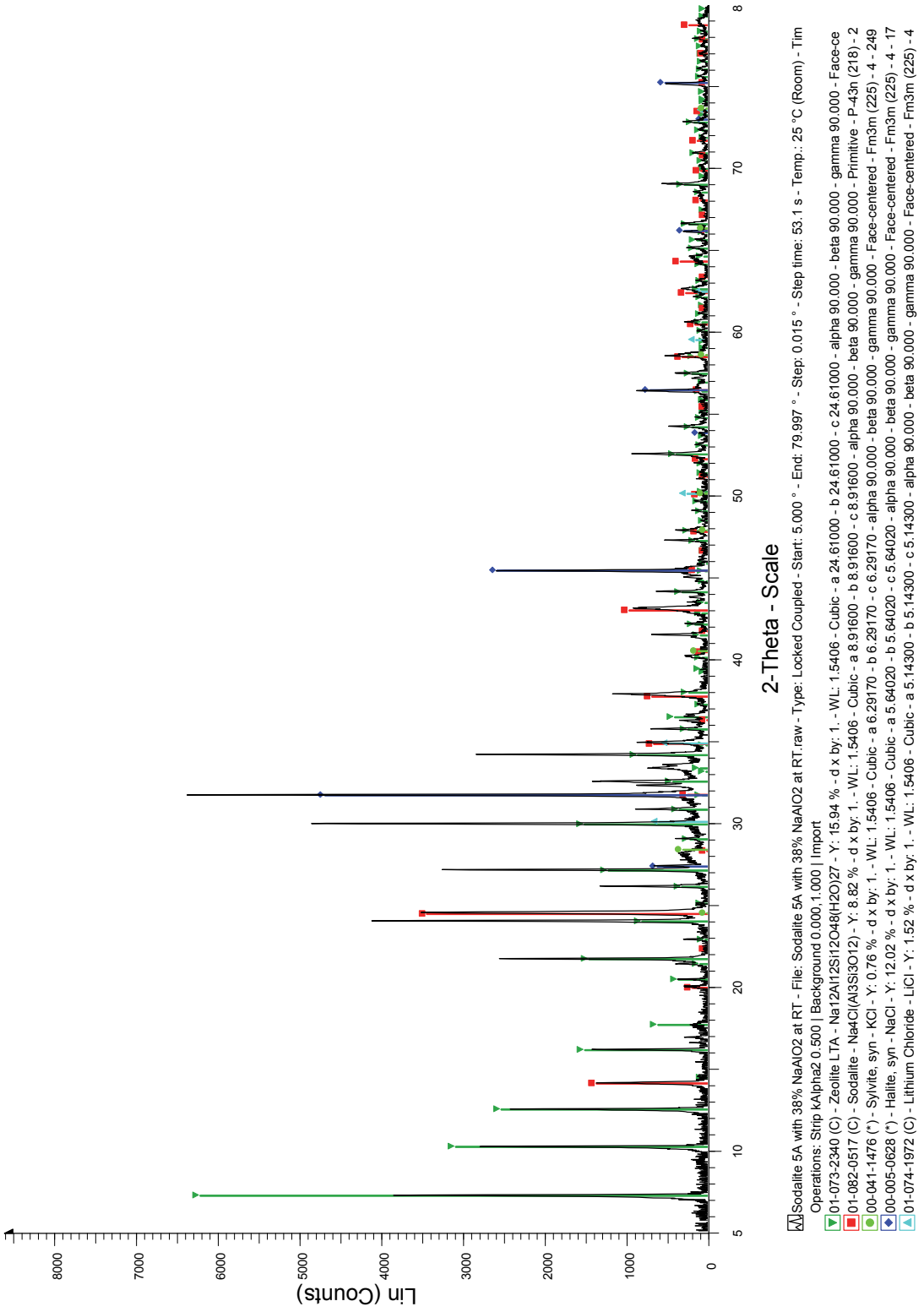

Figure B.4. Peak fitting for S5A with 38% $NaAlO_2$, unfired.

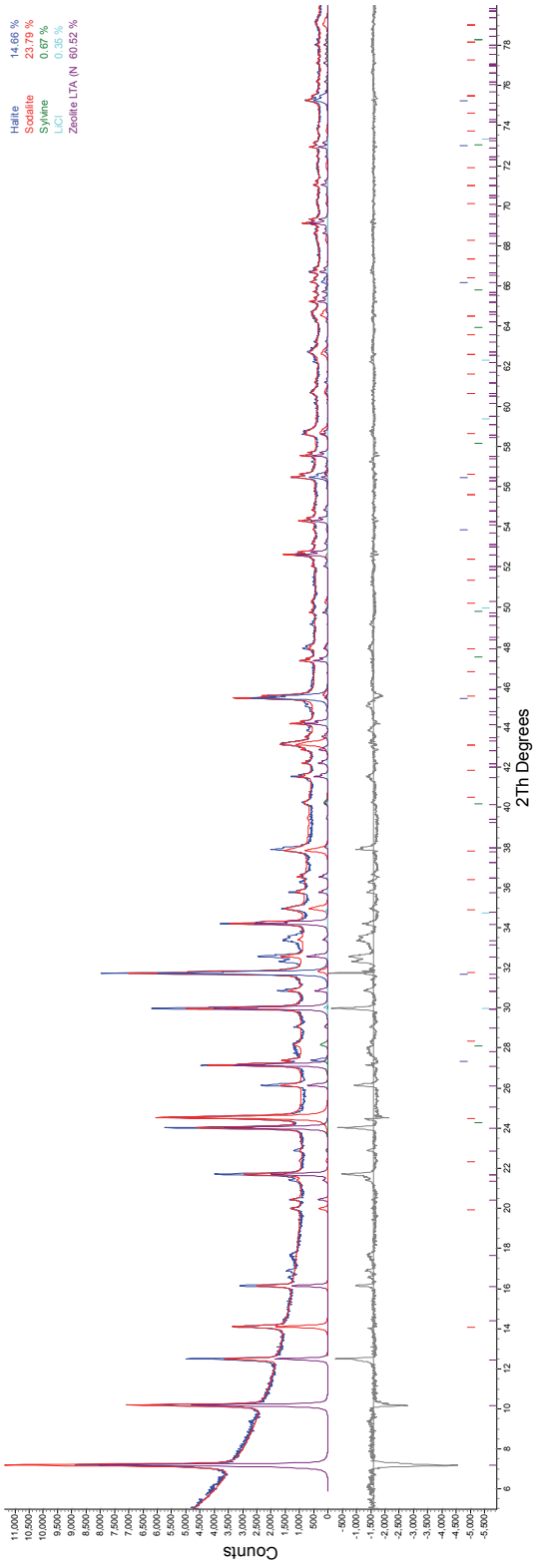

Figure B.5. Rietveld refinement for S5A with 38% $NaAlO_2$, unfired.

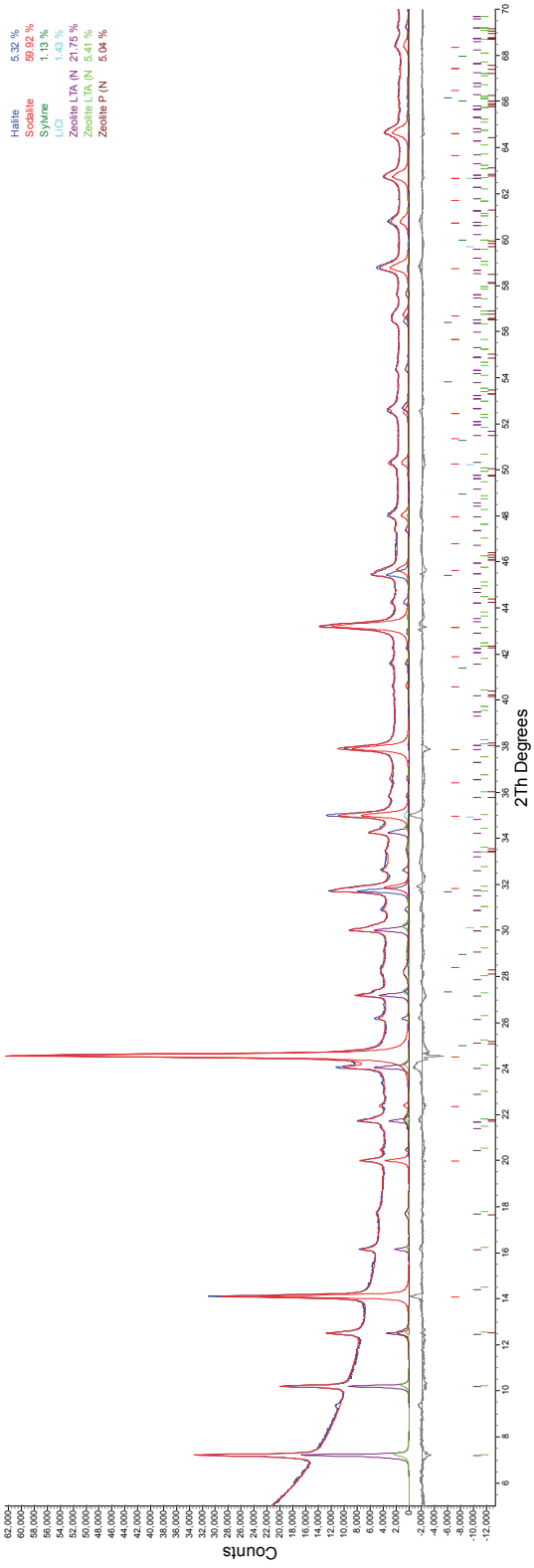

Figure B.6. Rietveld refinement for S5A with 38% $NaAlO_2$, fired at 550°C for 8 hrs.

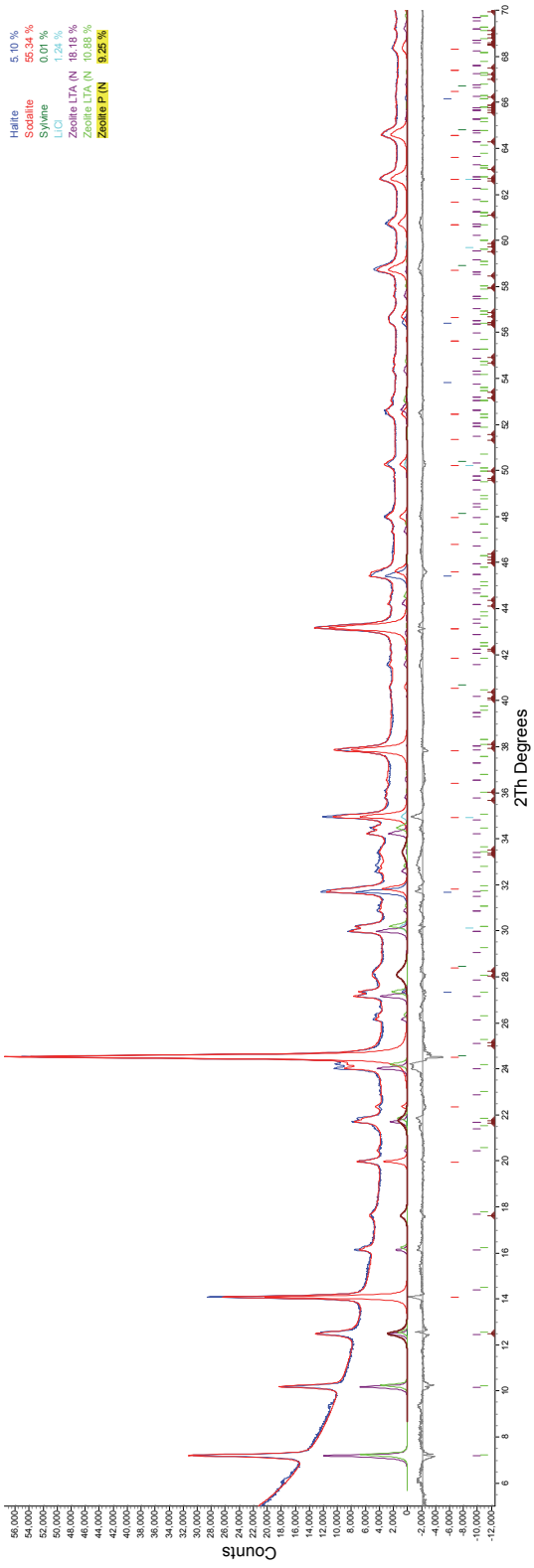

Figure B.7. Rietveld refinement for S5A with 38% $NaAlO_2$, fired at 650°C for 8 hrs.

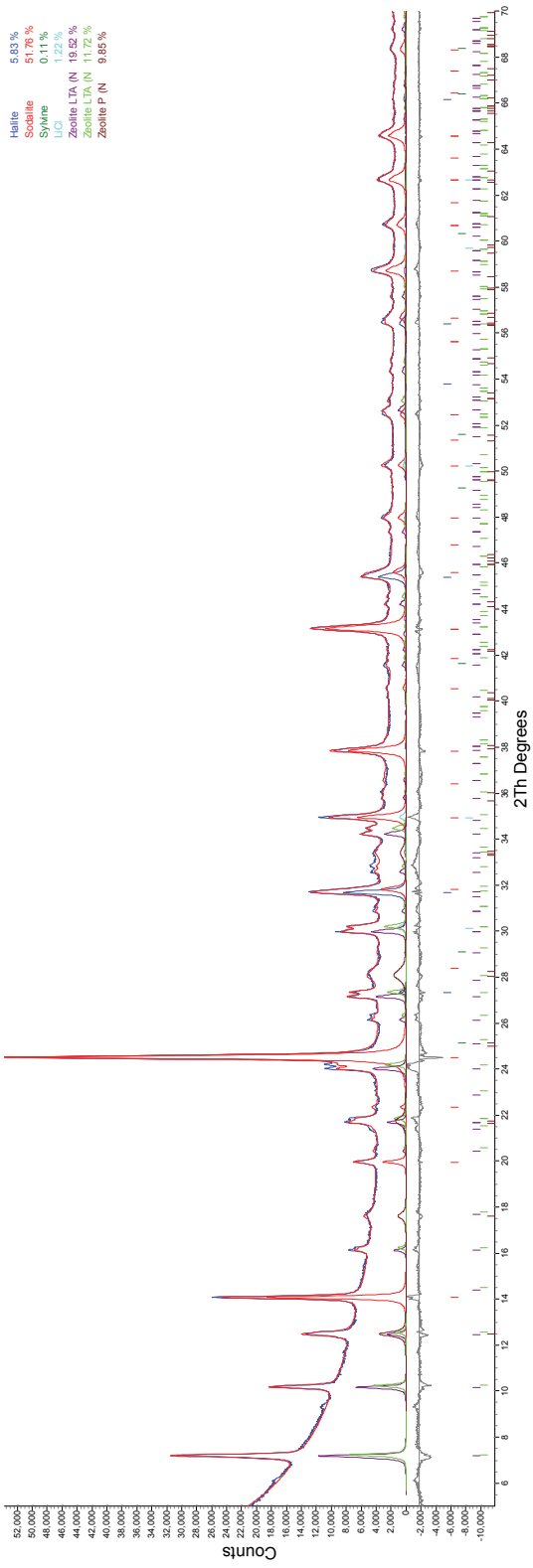

Figure B.8. Rietveld refinement for S5A with 38% $NaAlO_2$, fired at 750°C for 8 hrs.

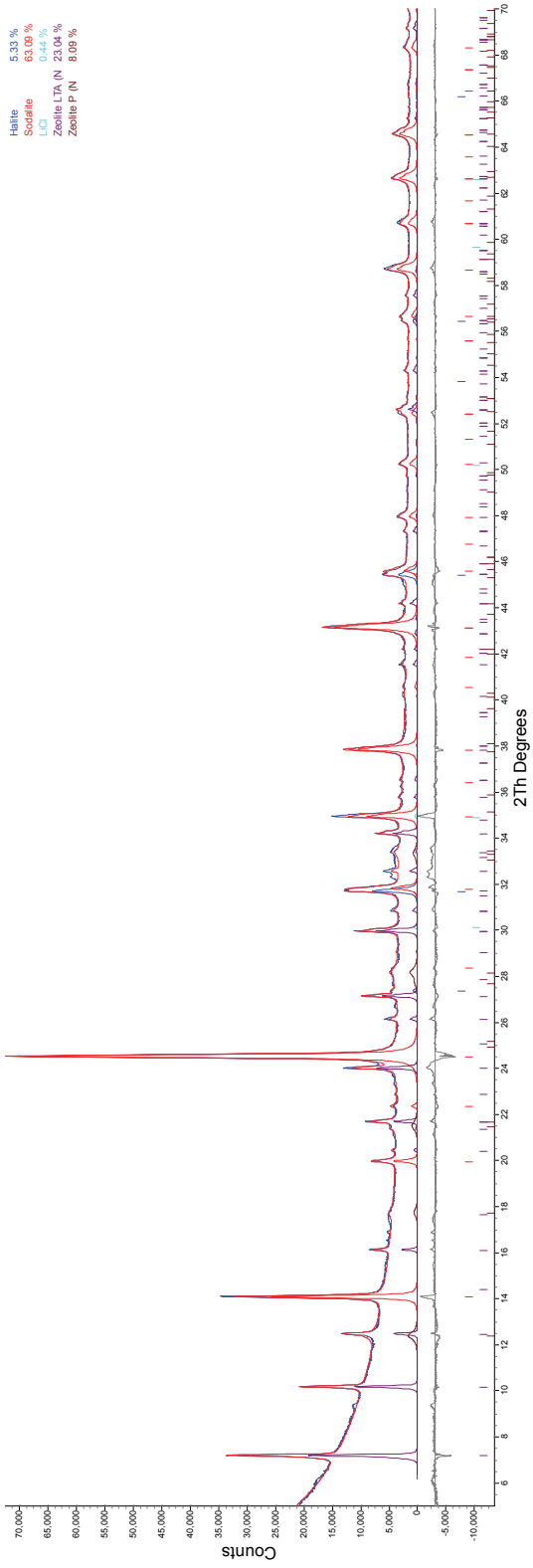

Figure B.9. Rietveld refinement for S5A with 38% $NaAlO_2$, fired at 850°C for 8 hrs.

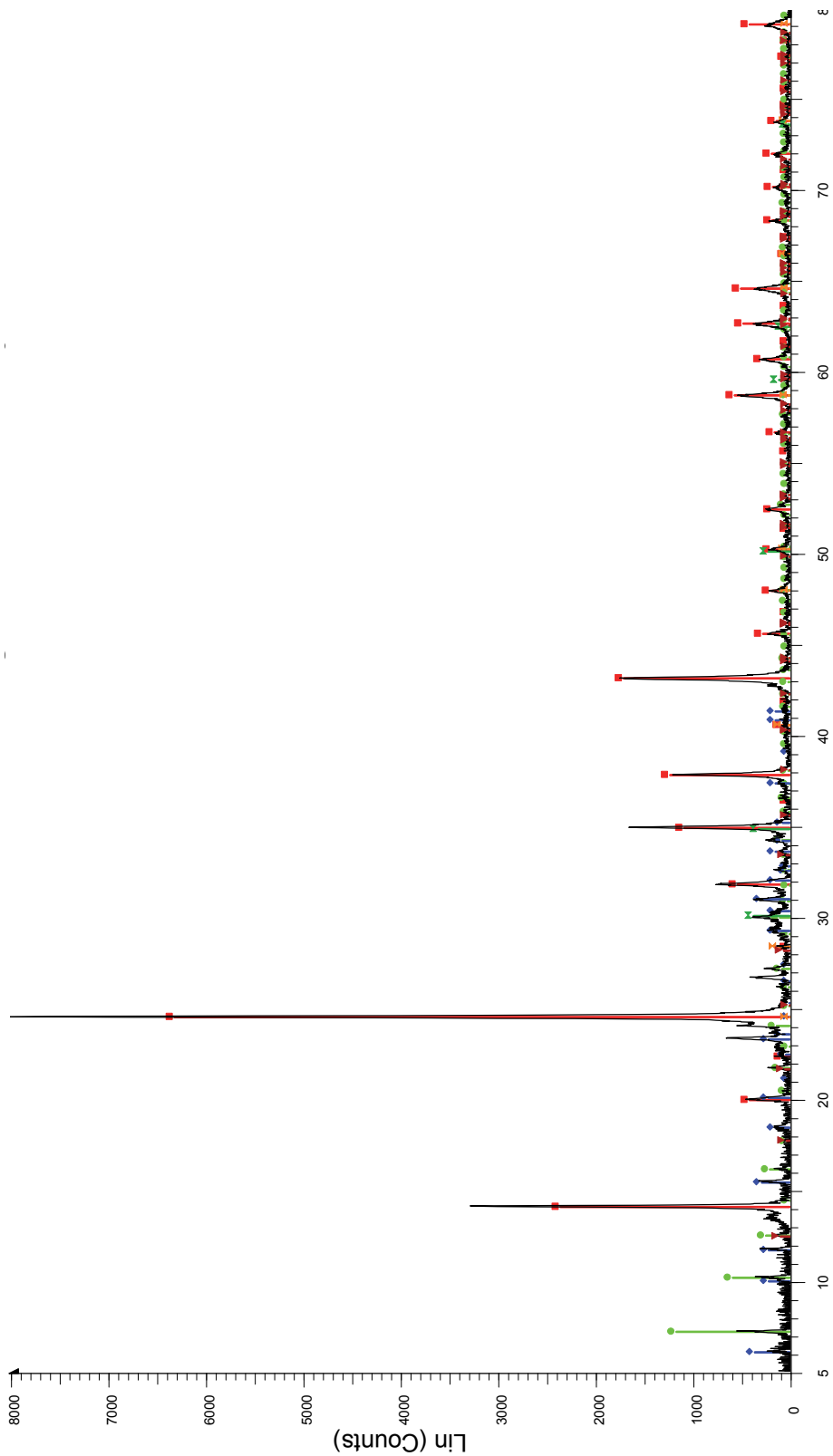

Figure B.10. Peak fitting for S5A made by stirring for two days and drying for five days, unfired.

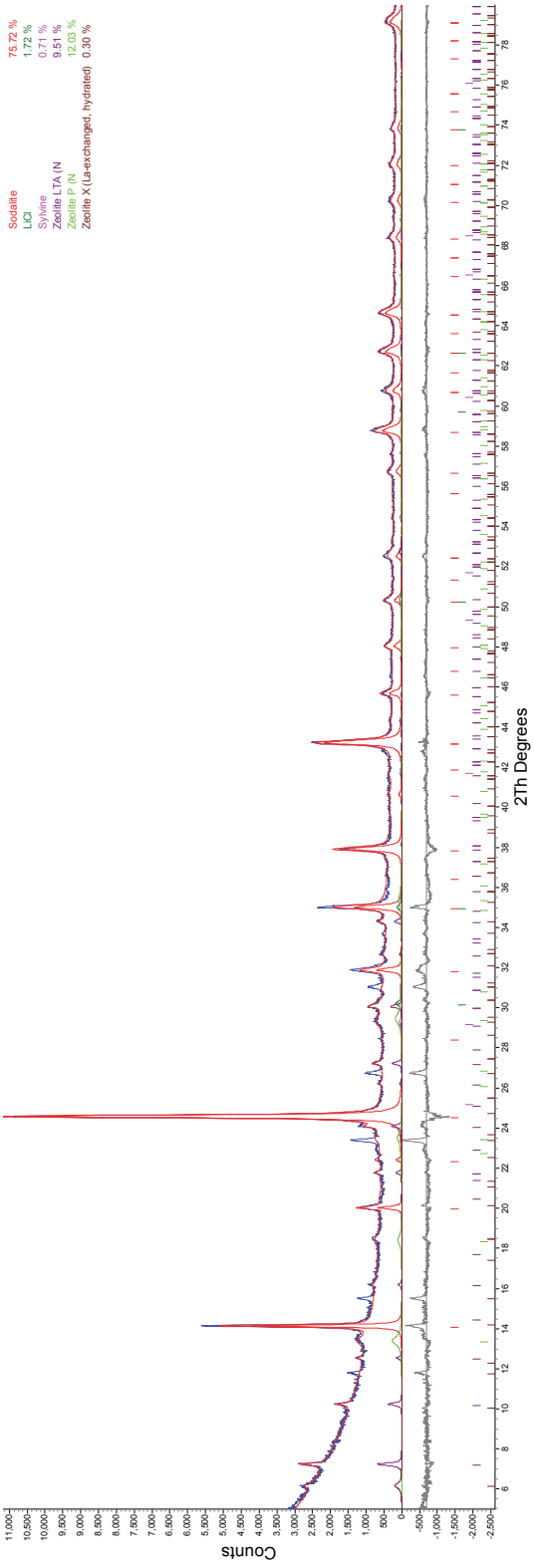

Figure B.11. Rietveld refinement for S5A made by stirring for two days and drying for five days, unfired.

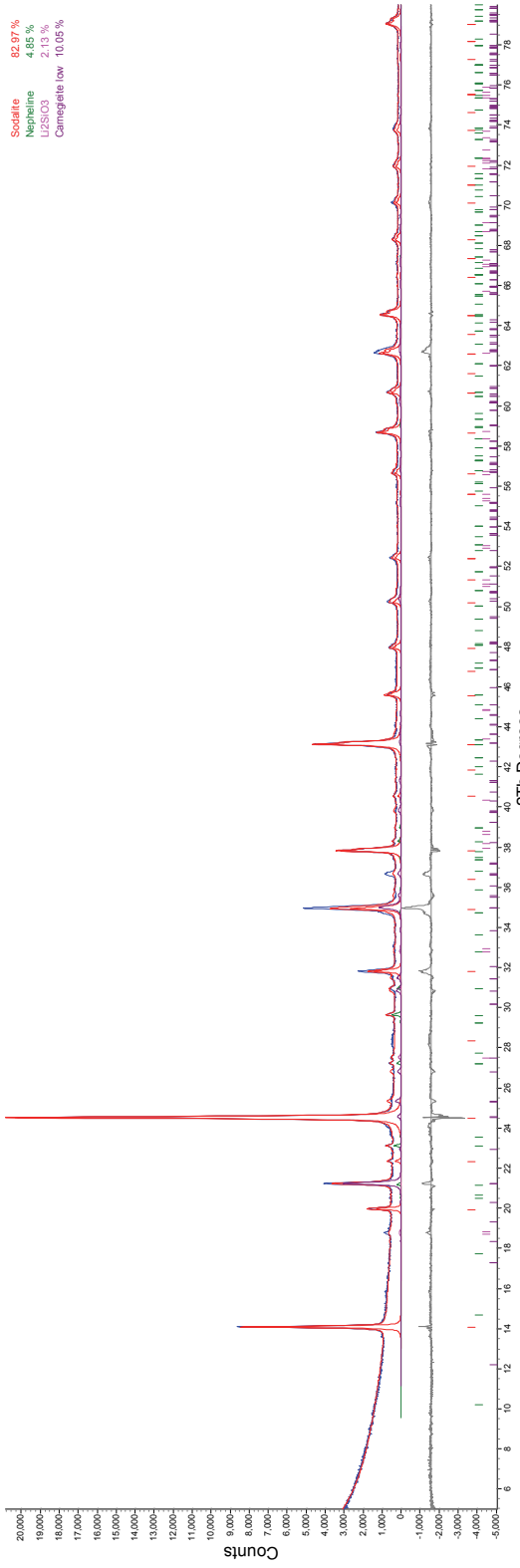

Figure B.12. Rietveld refinement for S5A made by stirring for two days and drying for five days, fired at 750°C for 8 hrs.

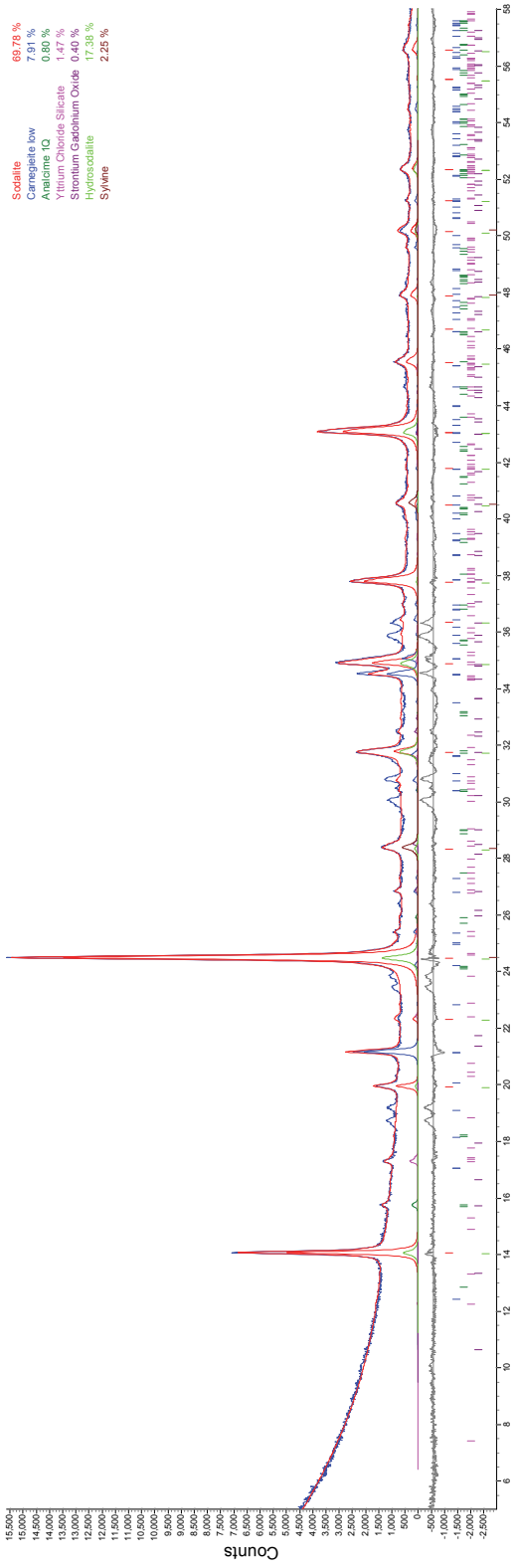

Figure B.13. Rietveld refinement for S5C (TEOS) with 5 mass% SA-700, fired at 550°C for 8 hrs.

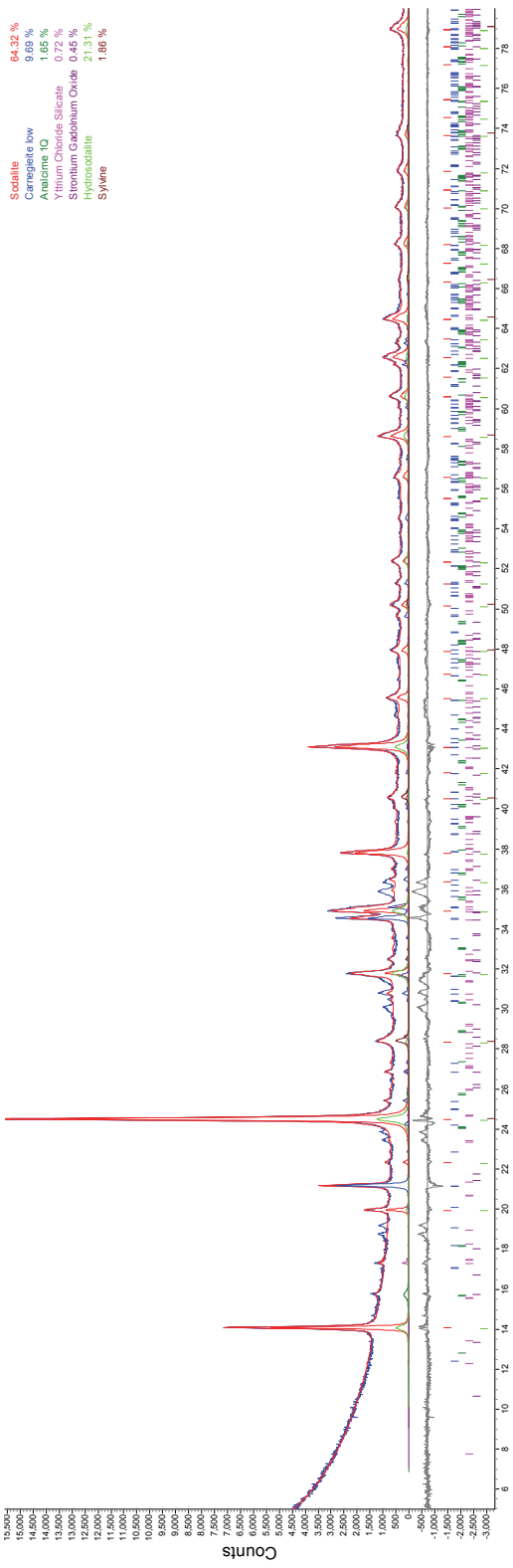

Figure B.14. Rietveld refinement for S5C (TEOS) with 5 mass% SA-700, fired at 600°C for 8 hrs.

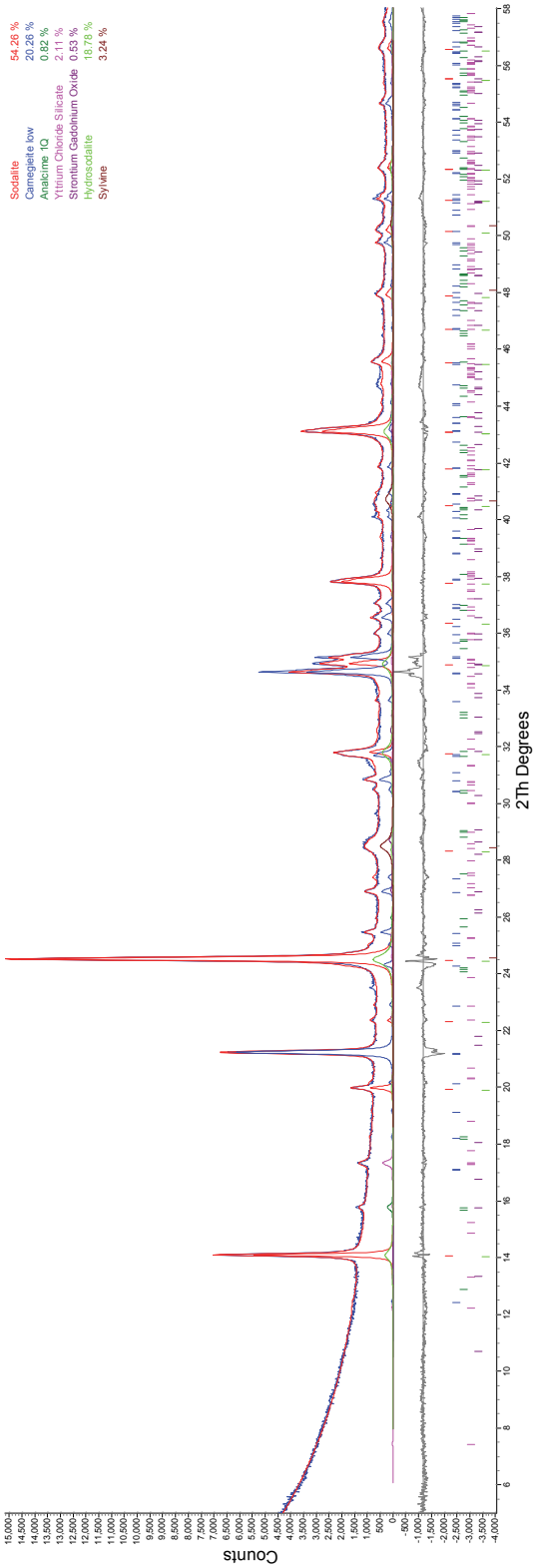

Figure B.15. Rietveld refinement for S5C (TEOS) with 5 mass% SA-700, fired at 650°C for 8 hrs.

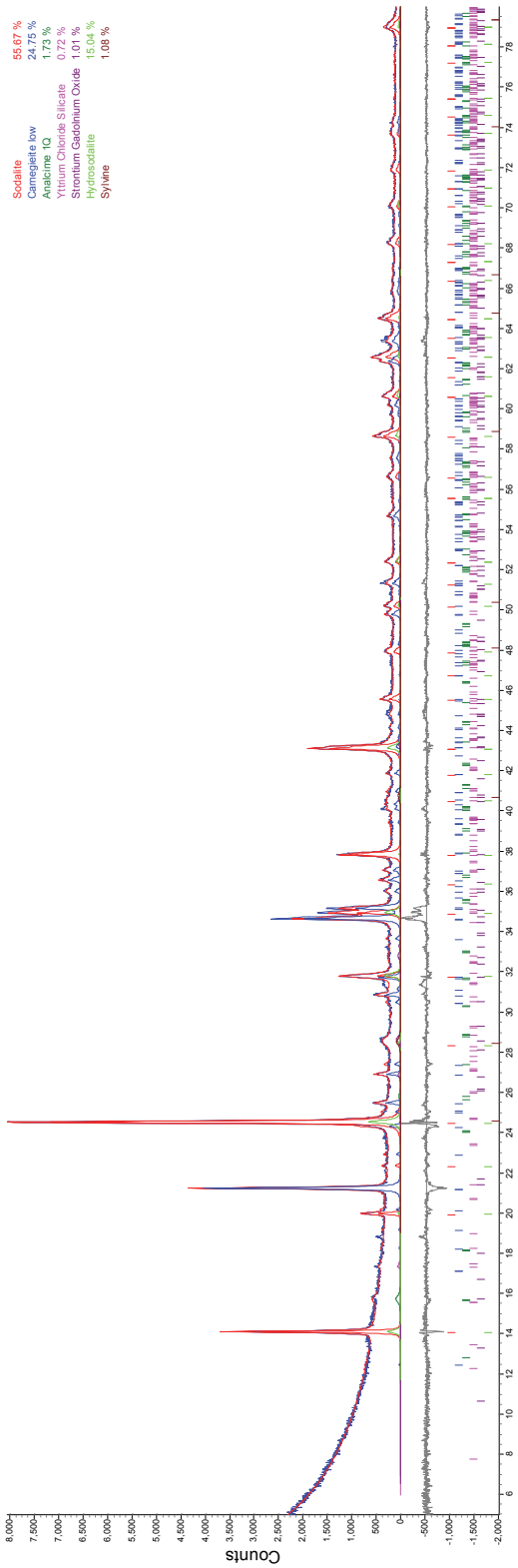

Figure B.16. Rietveld refinement for S5C (TEOS) with 5 mass% SA-700, fired at 750°C for 8 hrs.

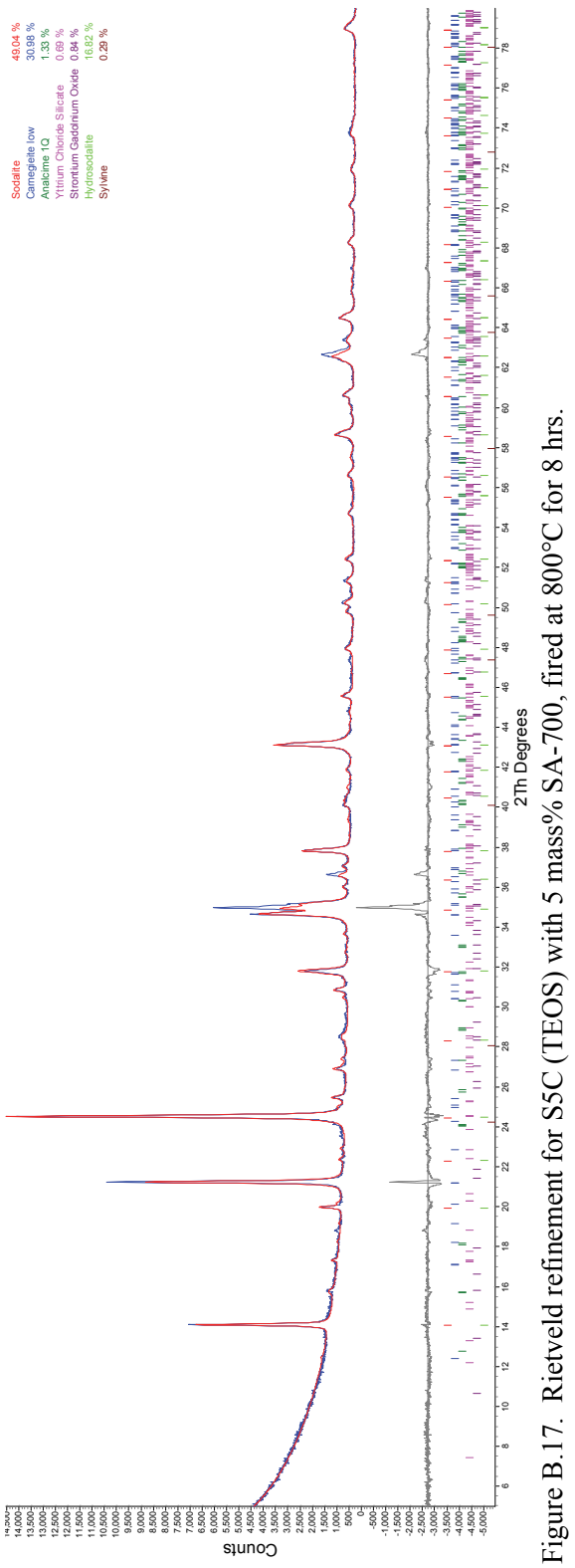

Figure B.17. Rietveld refinement for S5C (TEOS) with 5 mass% SA-700, fired at 800°C for 8 hrs.

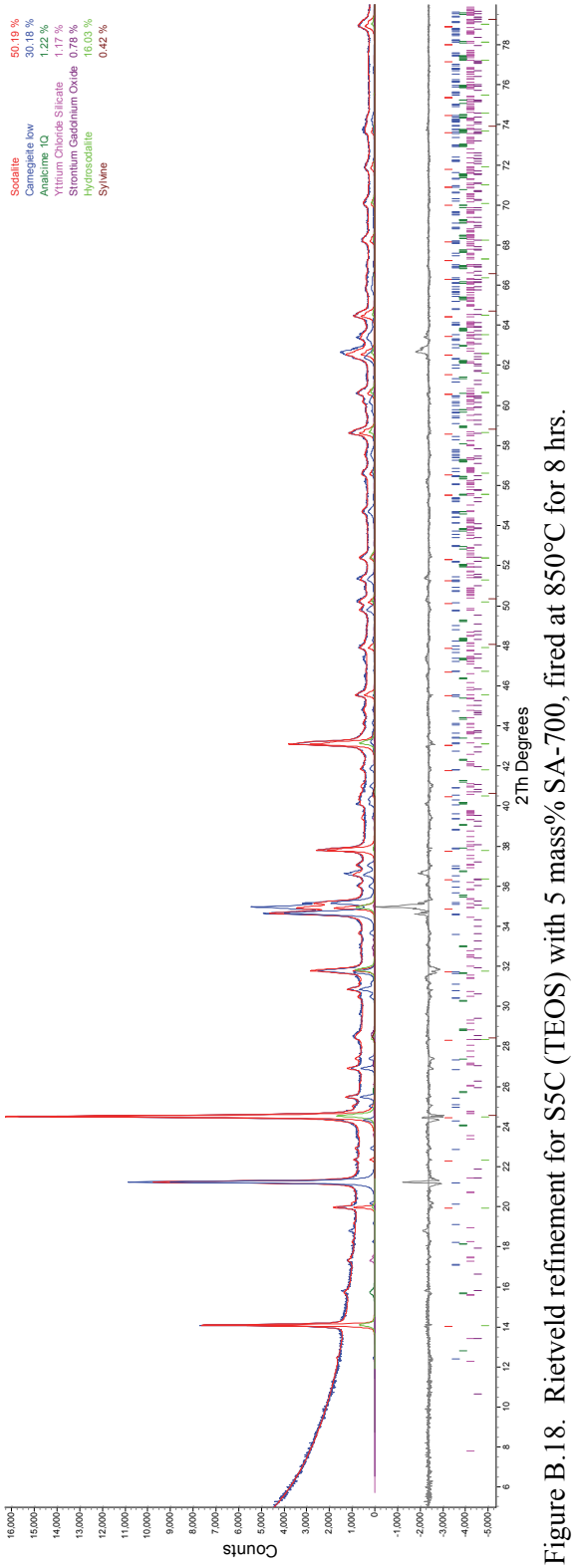

Figure B.18. Rietveld refinement for S5C (TEOS) with 5 mass% SA-700, fired at 850°C for 8 hrs.

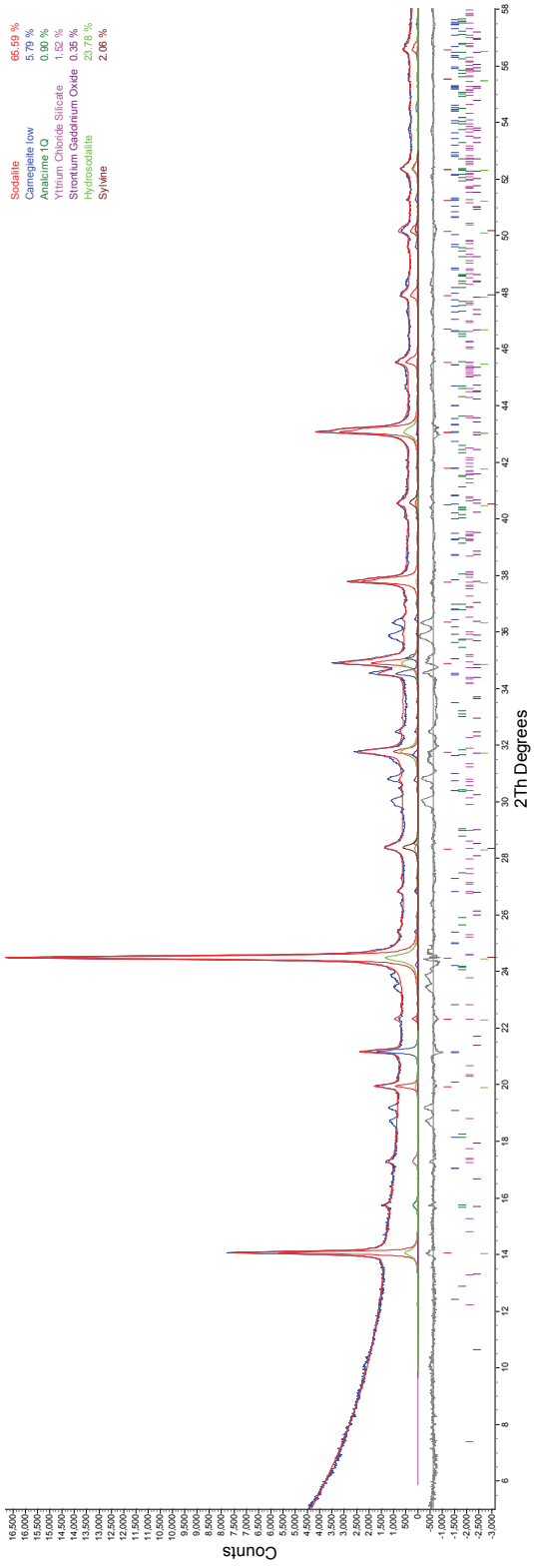

Figure B.19. Rietveld refinement for S5C (TEOS) with 5 mass% SA-750, fired at 550°C for 8 hrs.

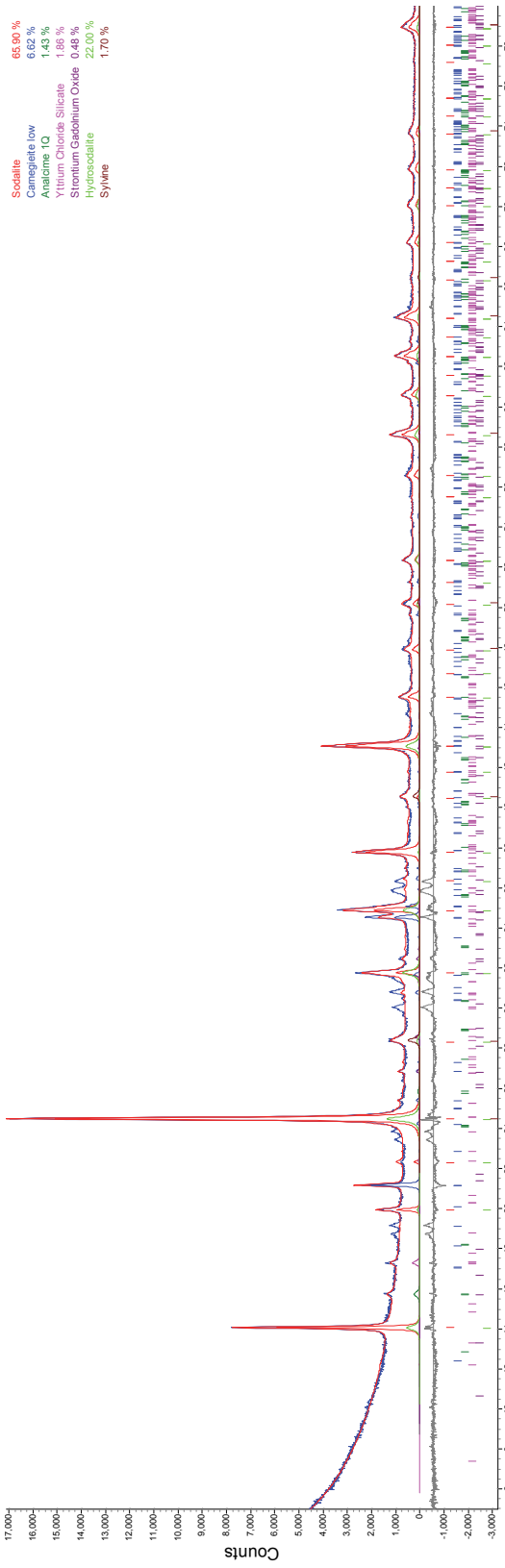

Figure B.20. Rietveld refinement for S5C (TEOS) with 5 mass% SA-750, fired at 600°C for 8 hrs.

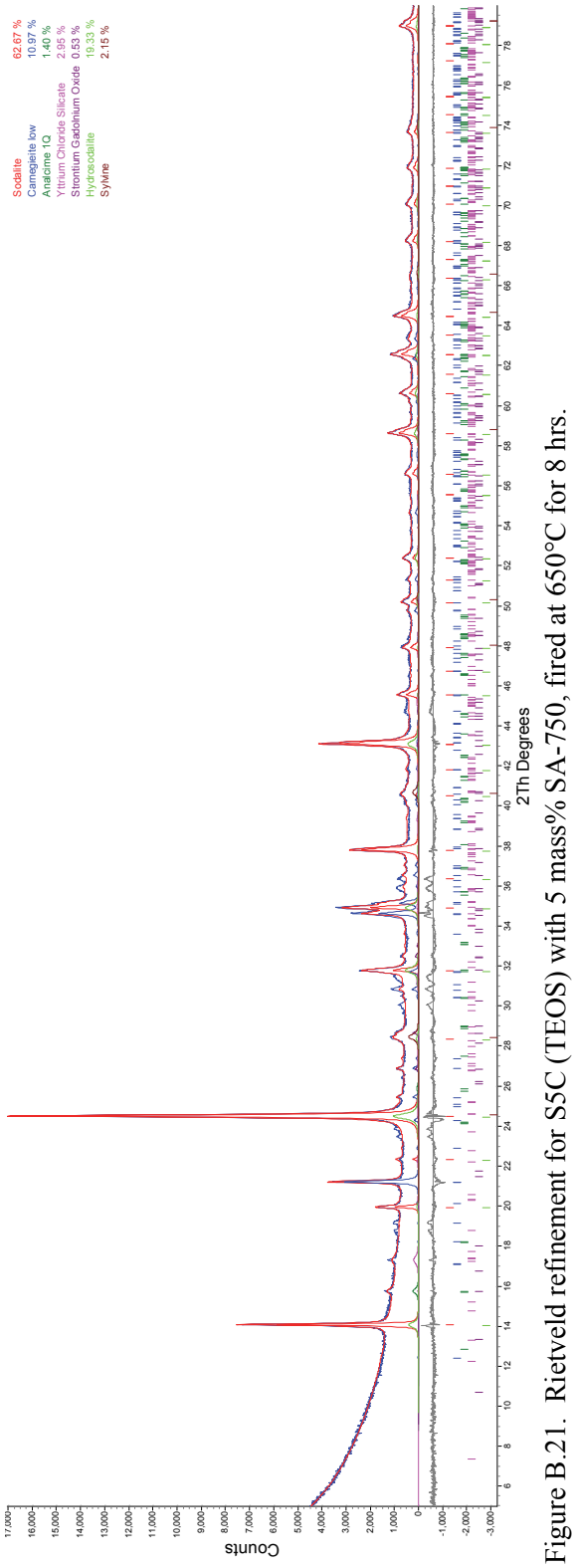

Figure B.21. Rietveld refinement for S5C (TEOS) with 5 mass% SA-750, fired at 650°C for 8 hrs.

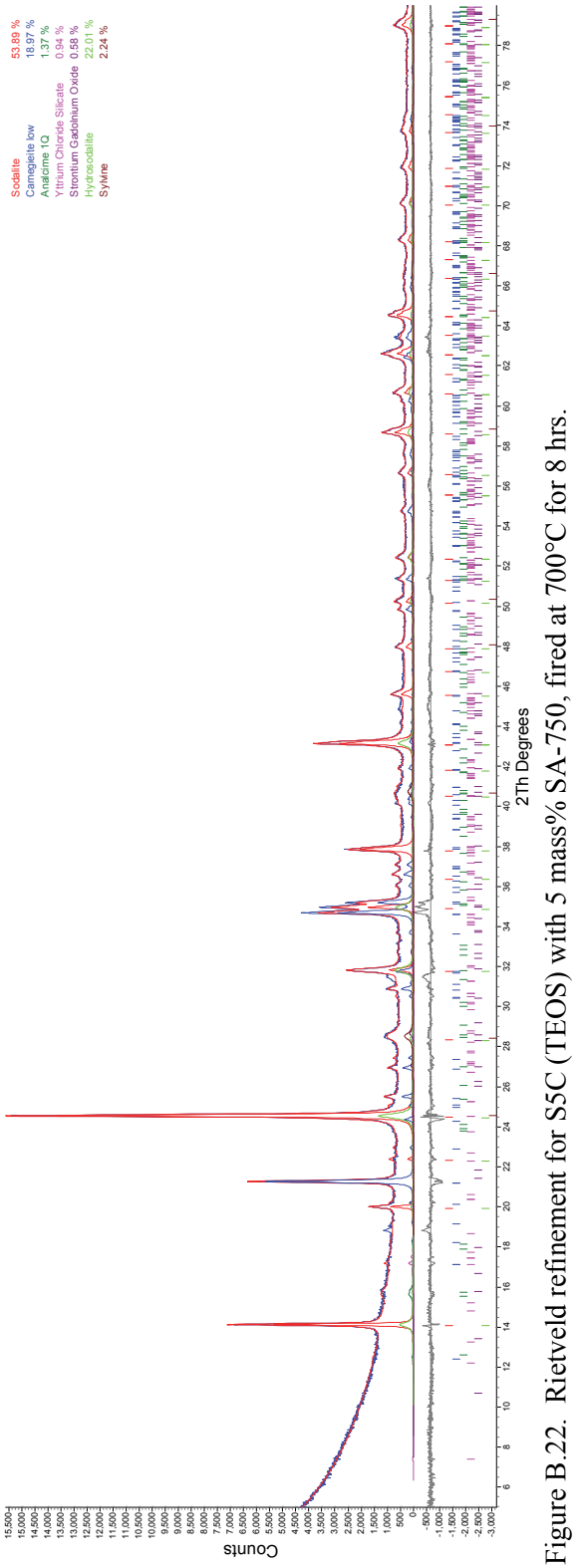

Figure B.22. Rietveld refinement for S5C (TEOS) with 5 mass% SA-750, fired at 700°C for 8 hrs.

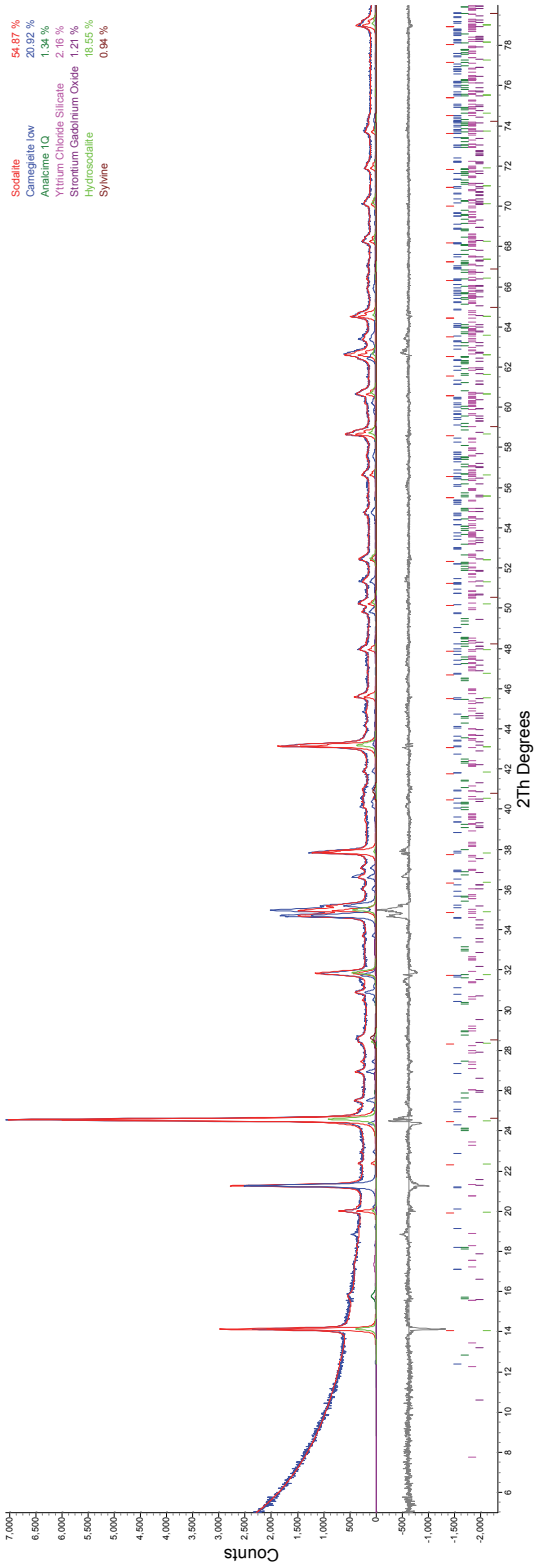

Figure B.23. Rietveld refinement for S5C (TEOS) with 5 mass% SA-750, fired at 750°C for 8 hrs.

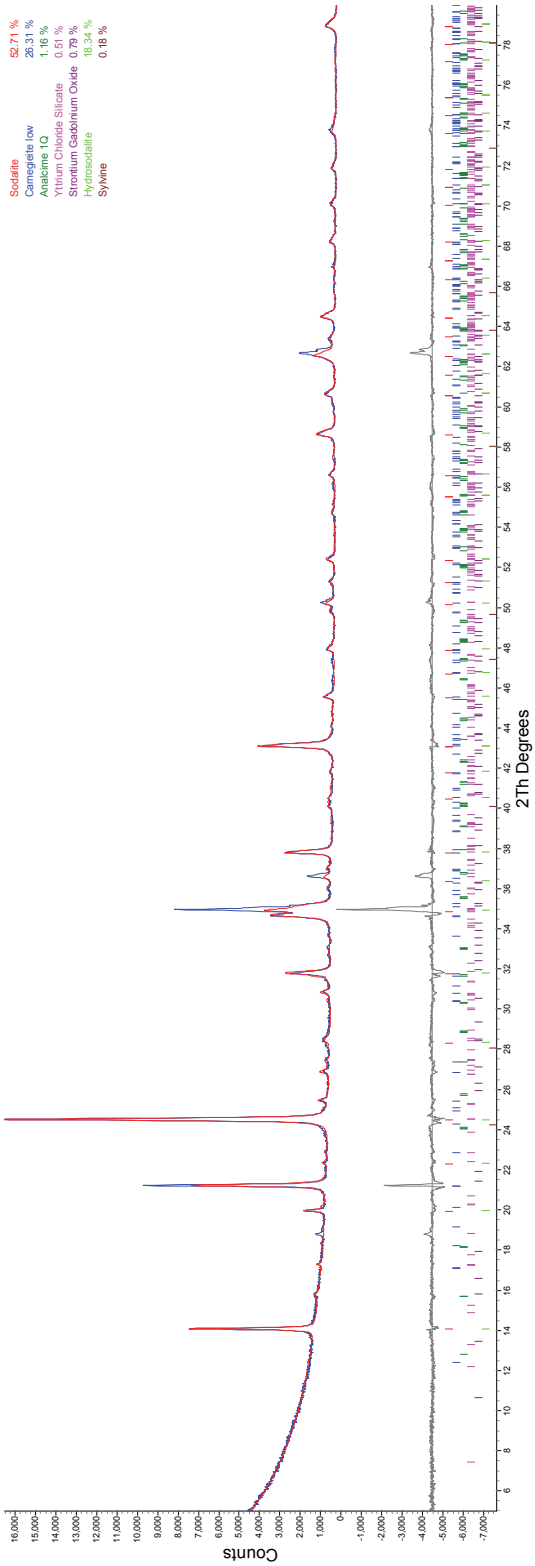

Figure B.24. Rietveld refinement for S5C (TEOS) with 5 mass% SA-750, fired at 800°C for 8 hrs.

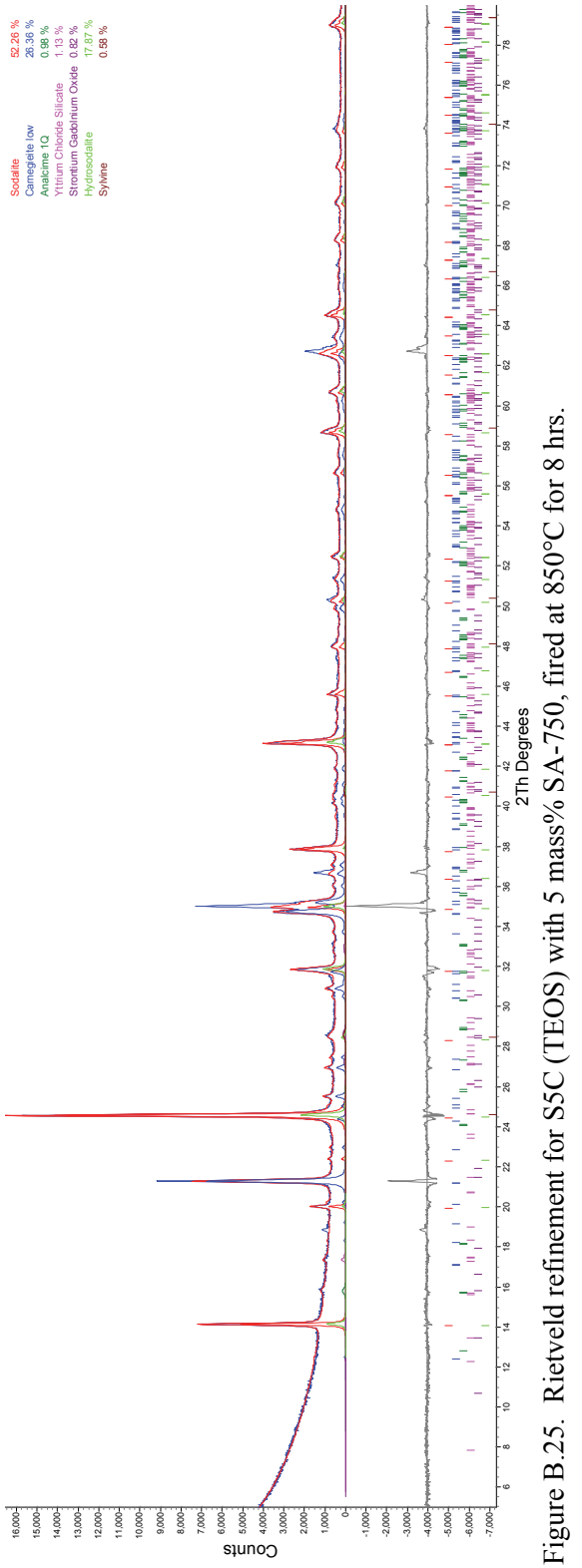

Figure B.25. Rietveld refinement for S5C (TEOS) with 5 mass% SA-750, fired at 850°C for 8 hrs.

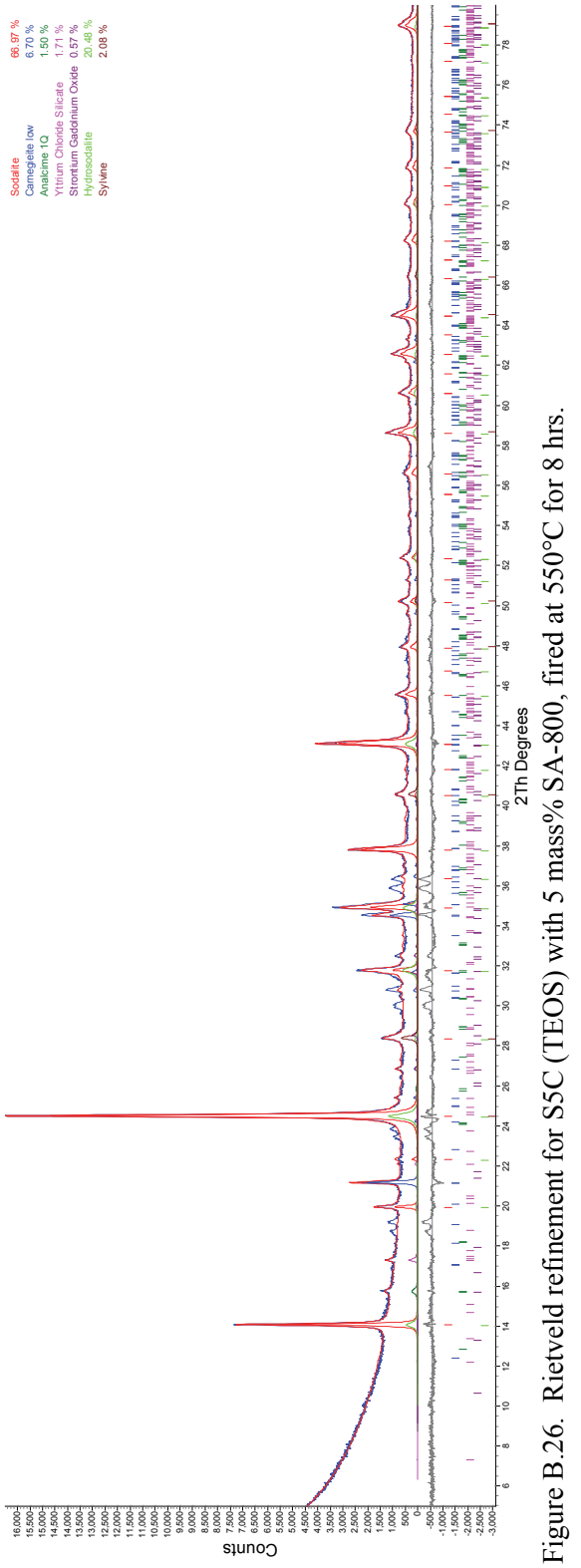

Figure B.26. Rietveld refinement for S5C (TEOS) with 5 mass% SA-800, fired at 550°C for 8 hrs.

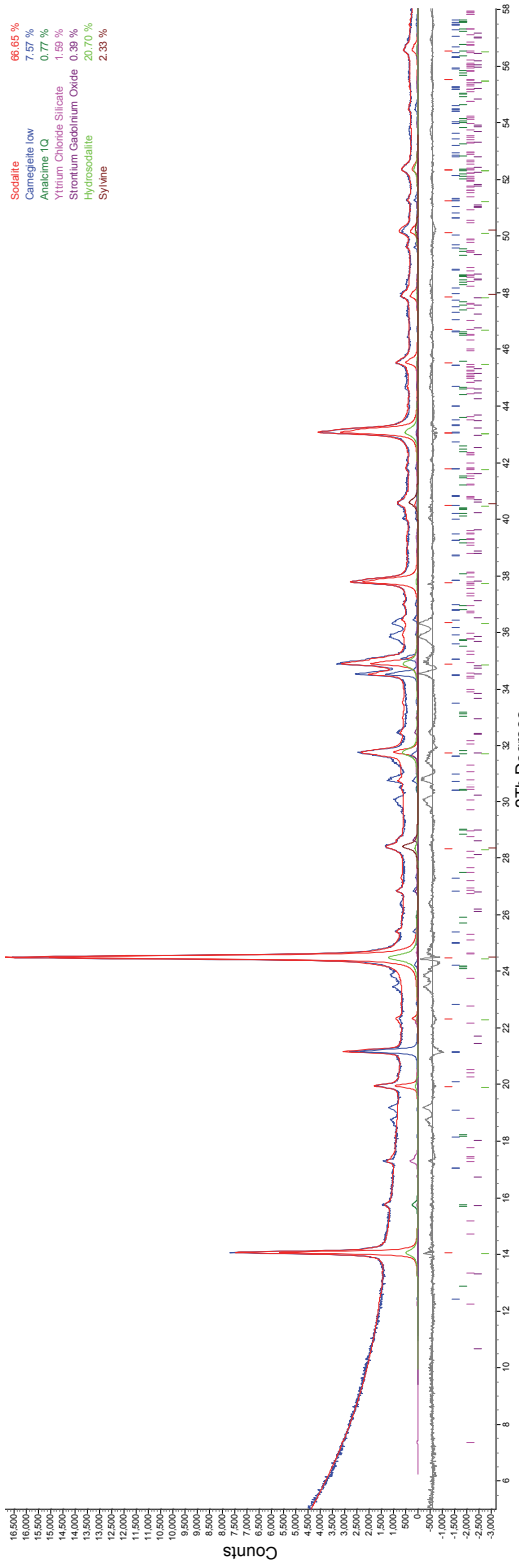

Figure B.27. Rietveld refinement for S5C (TEOS) with 5 mass% SA-800, fired at 600°C for 8 hrs.

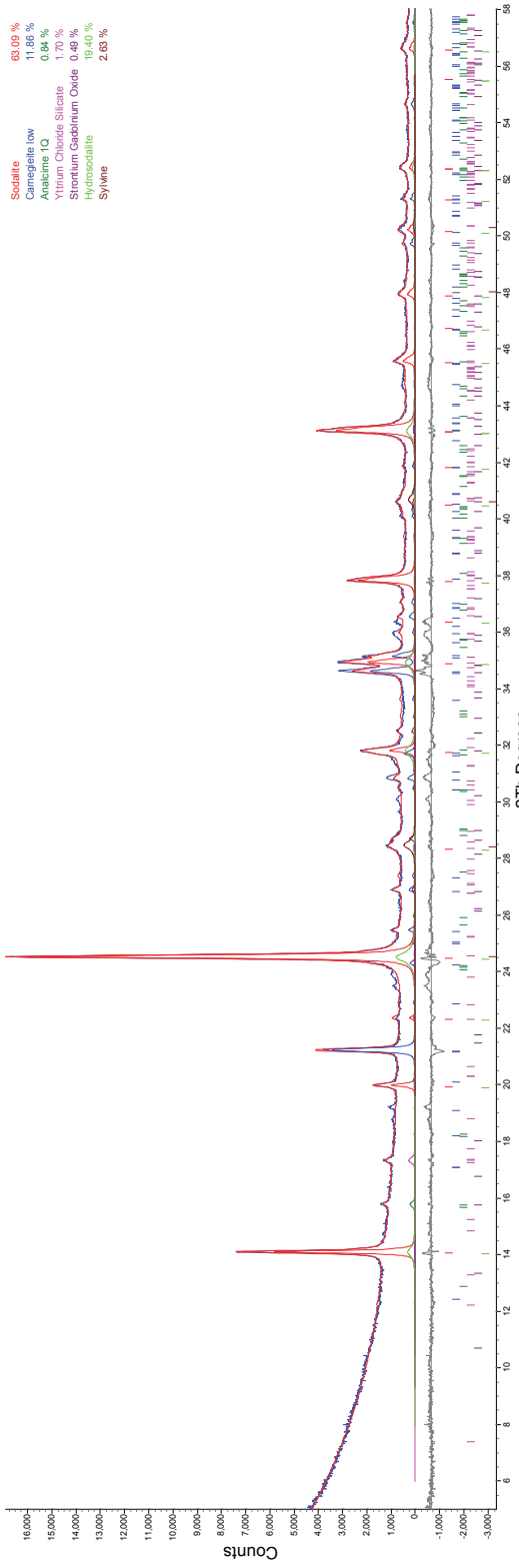

Figure B.28. Rietveld refinement for S5C (TEOS) with 5 mass% SA-800, fired at 650°C for 8 hrs.

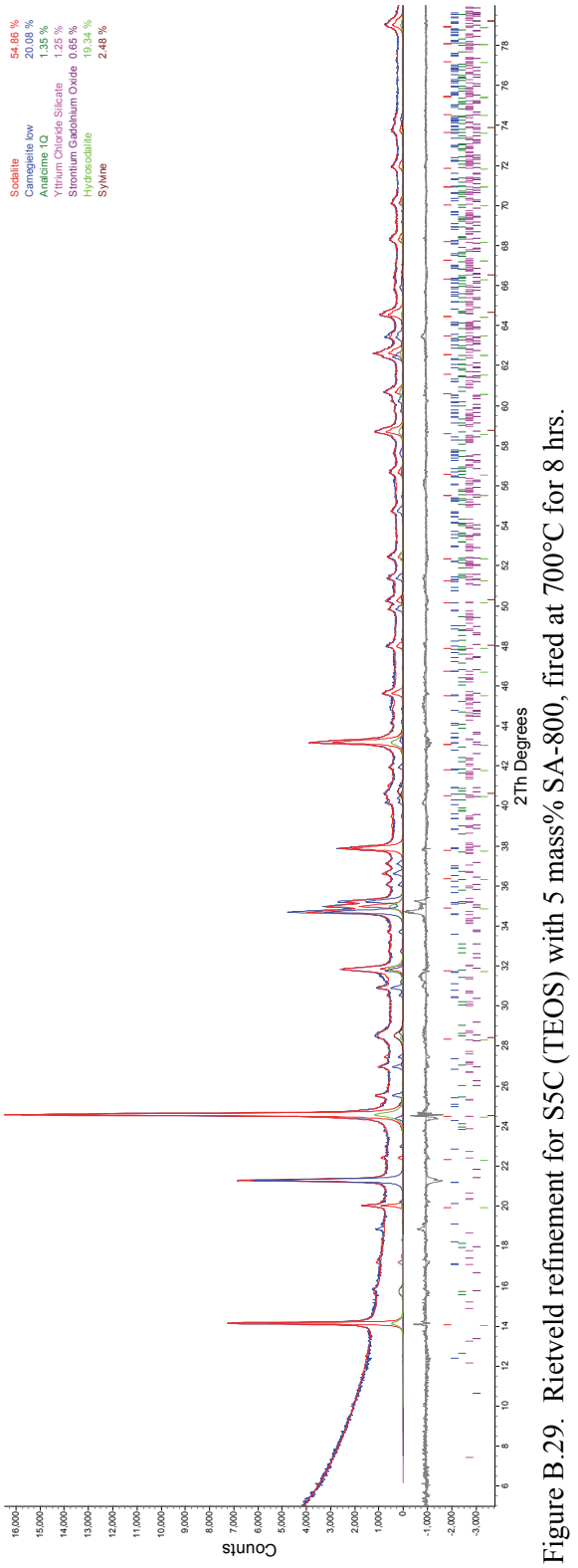

Figure B.29. Rietveld refinement for S5C (TEOS) with 5 mass% SA-800, fired at 700°C for 8 hrs.

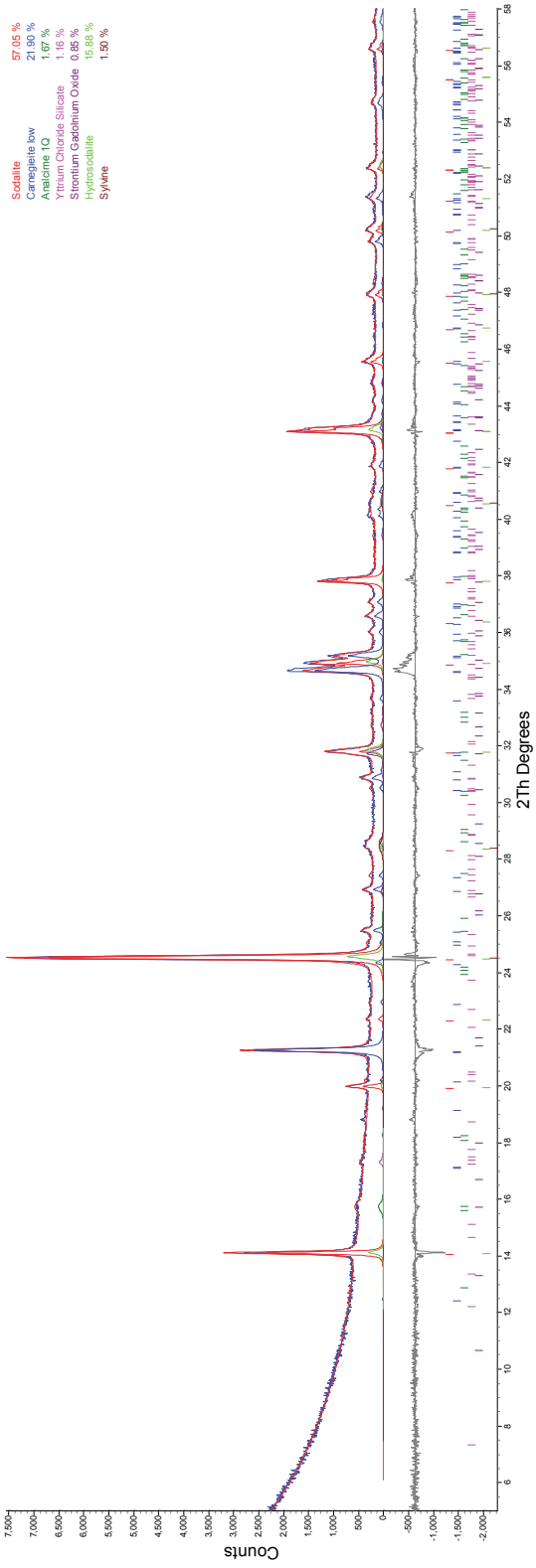

Figure B.30. Rietveld refinement for S5C (TEOS) with 5 mass% SA-800, fired at 750°C for 8 hrs.

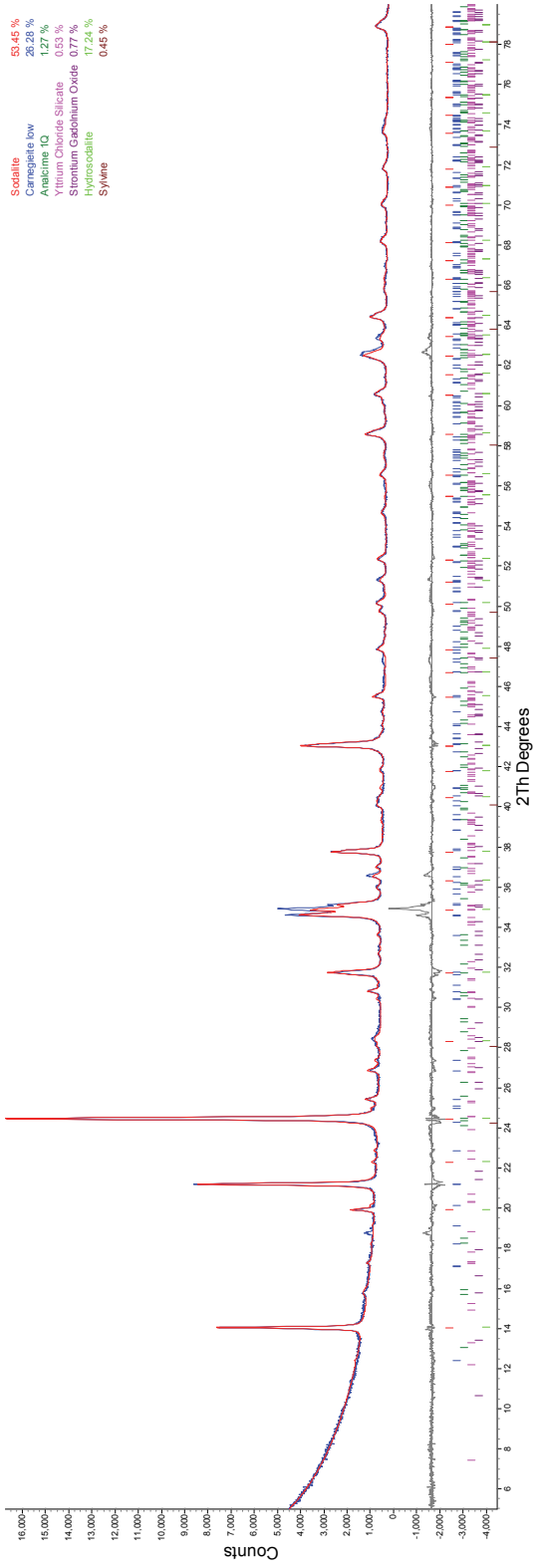

Figure B.31. Rietveld refinement for S5C (TEOS) with 5 mass% SA-800, fired at 800°C for 8 hrs.

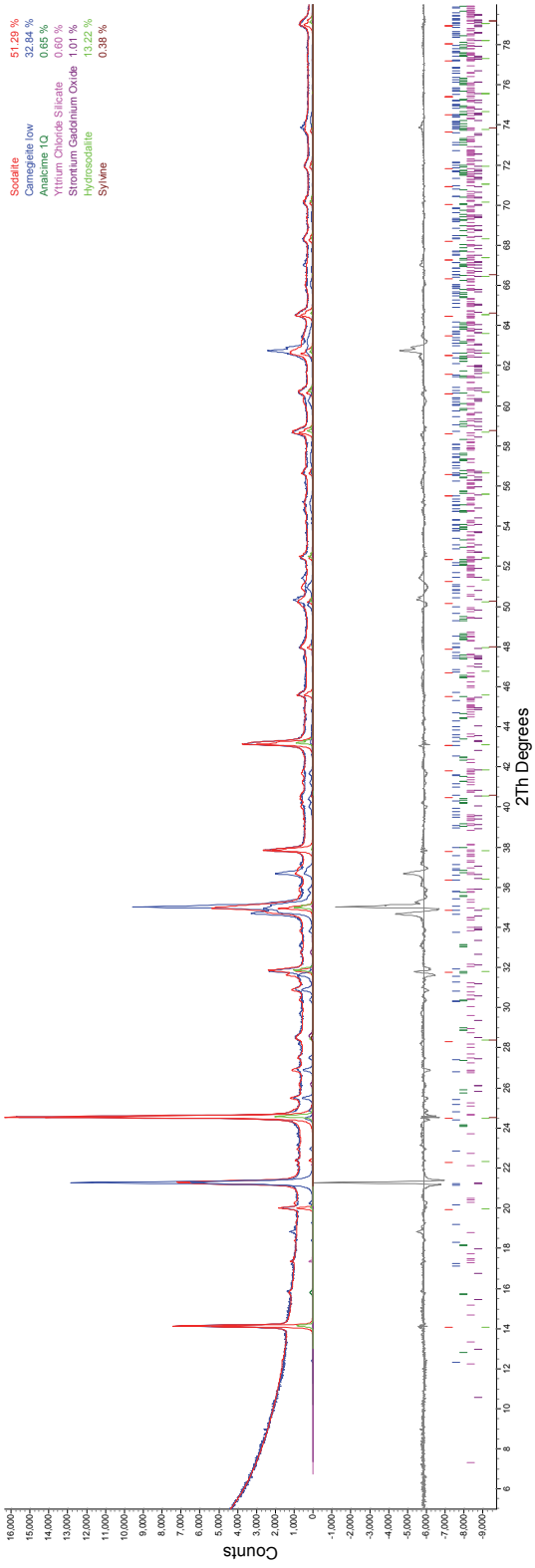

Figure B.32. Rietveld refinement for S5C (TEOS) with 5 mass% SA-800, fired at 850°C for 8 hrs.

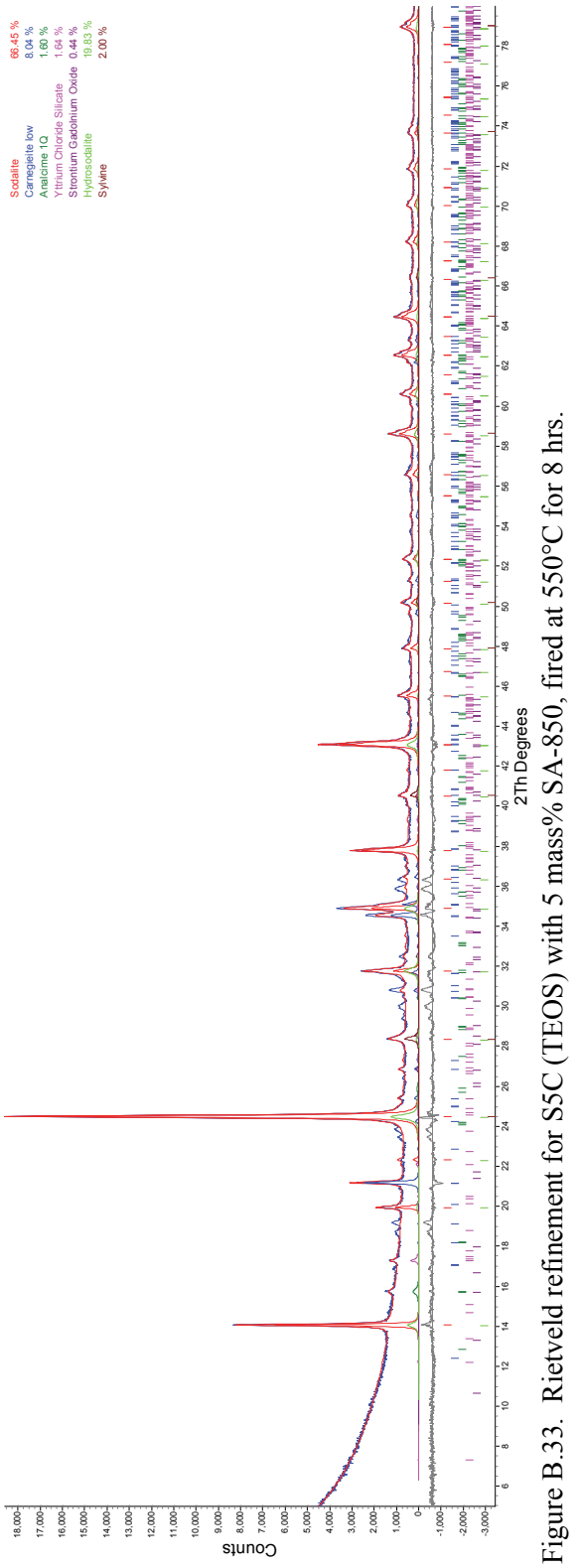

Figure B.33. Rietveld refinement for S5C (TEOS) with 5 mass% SA-850, fired at 550°C for 8 hrs.

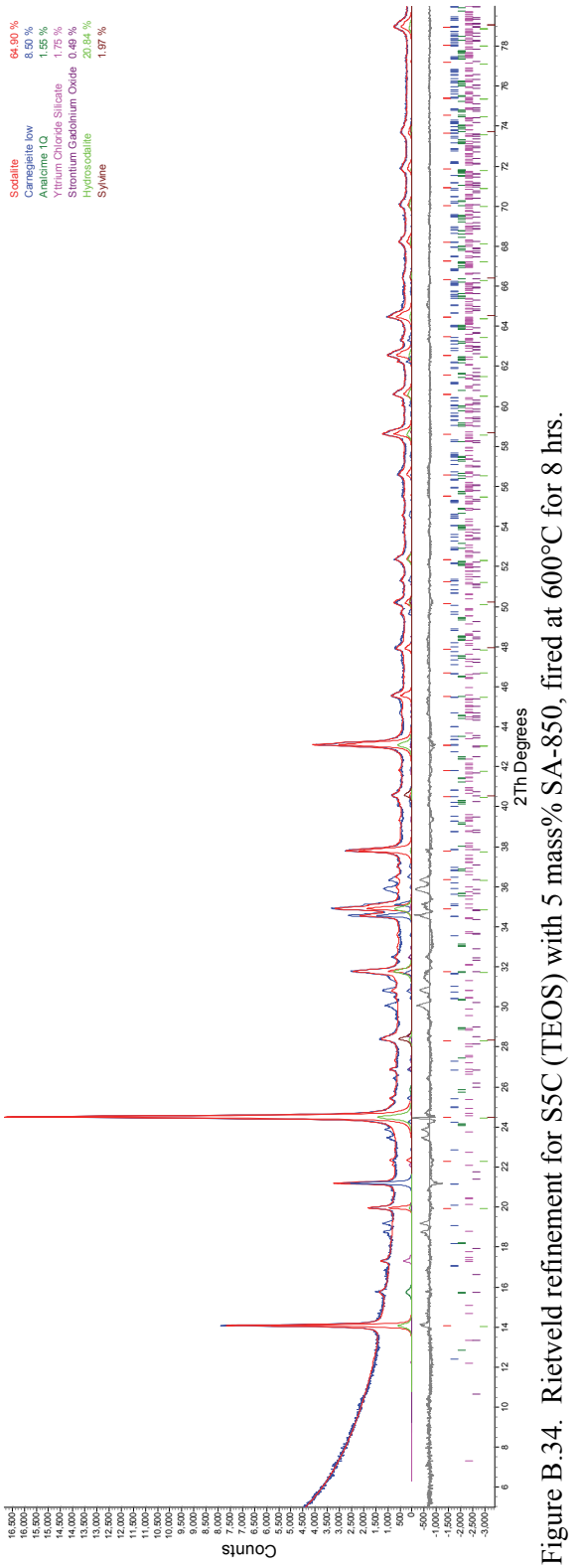

Figure B.34. Rietveld refinement for S5C (TEOS) with 5 mass% SA-850, fired at 600°C for 8 hrs.

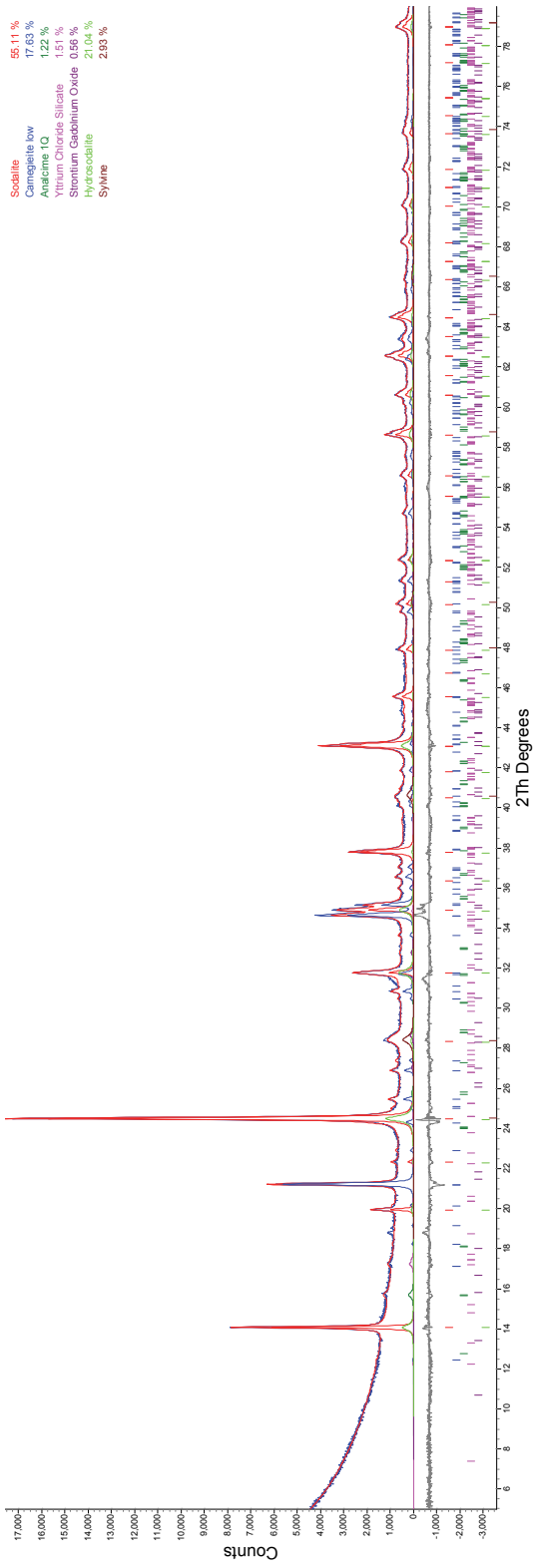

Figure B.35. Rietveld refinement for S5C (TEOS) with 5 mass% SA-850, fired at 650°C for 8 hrs.

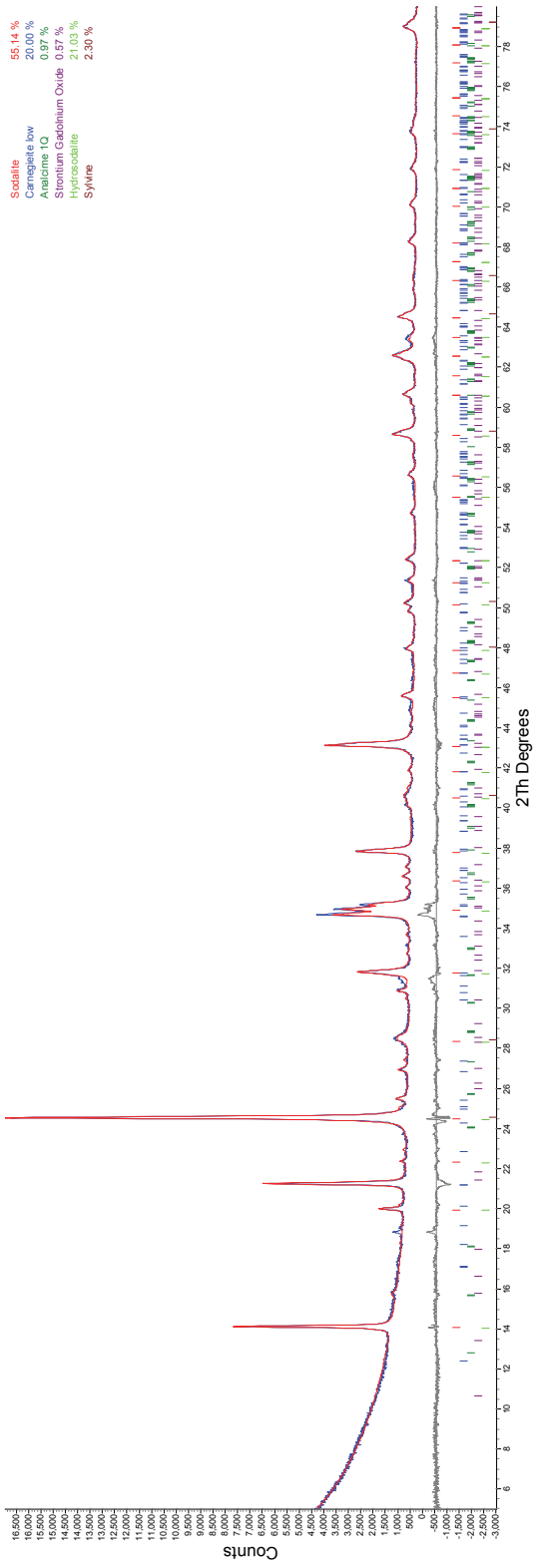

Figure B.36. Rietveld refinement for S5C (TEOS) with 5 mass% SA-850, fired at 700°C for 8 hrs.

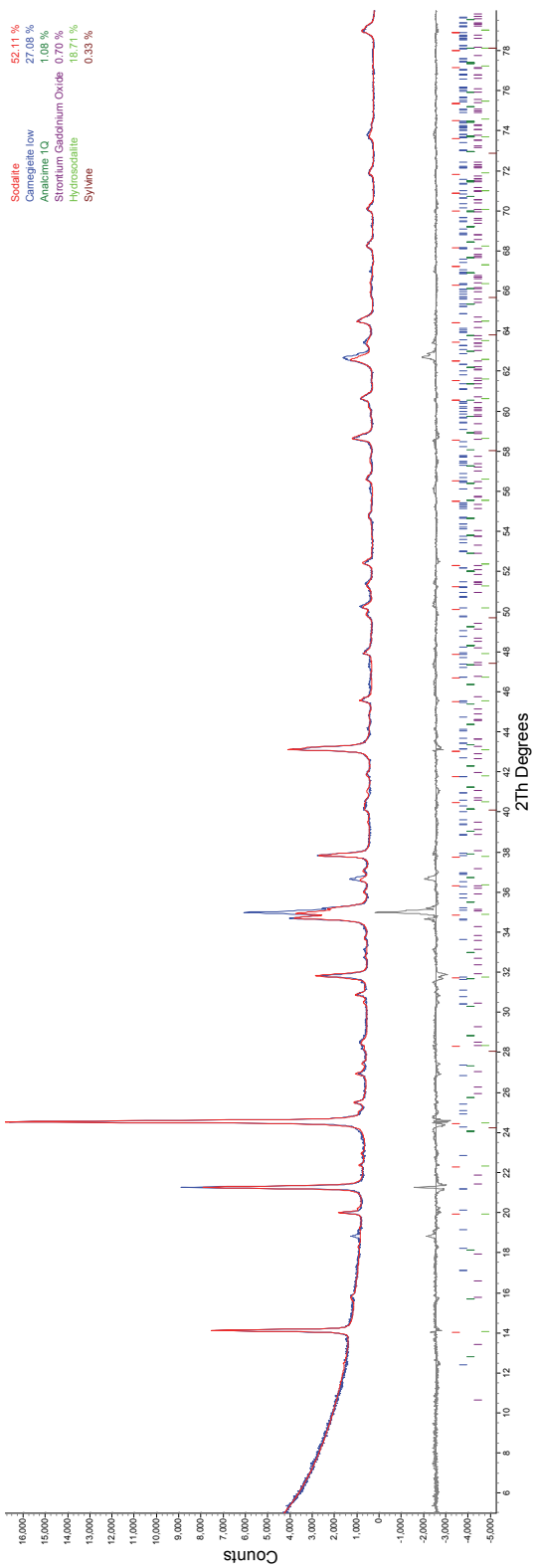

Figure B.37. Rietveld refinement for S5C (TEOS) with 5 mass% SA-850, fired at 800°C for 8 hrs.

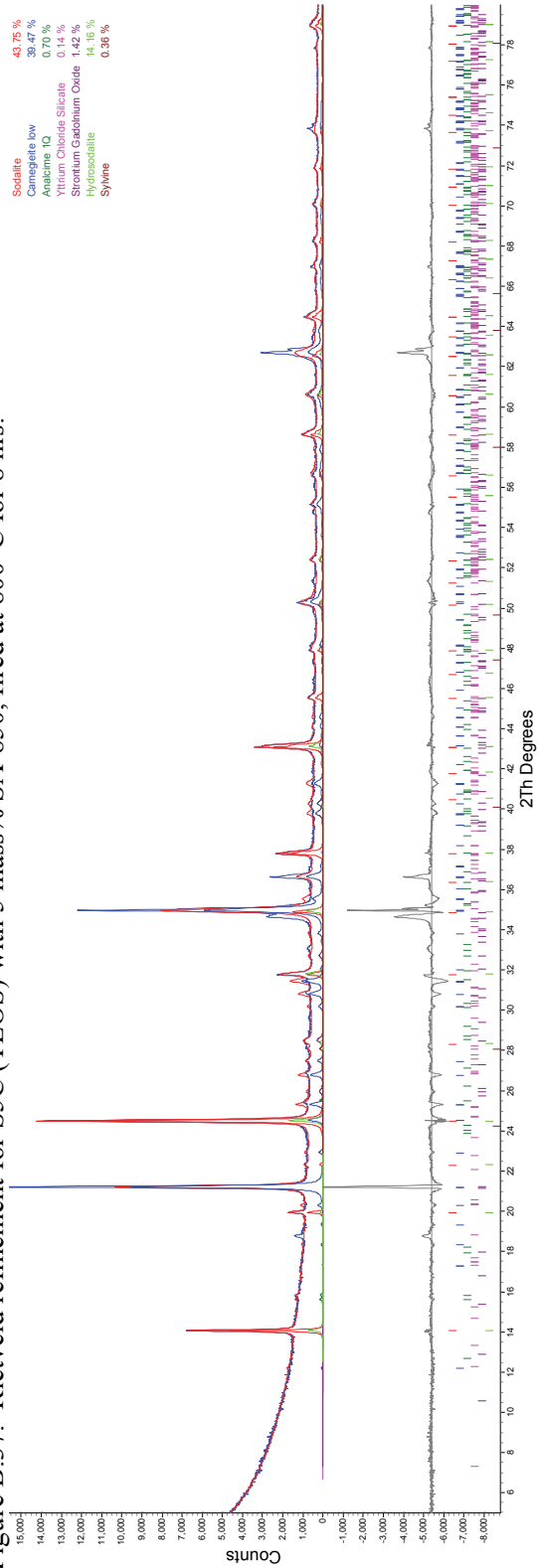

Figure B.38. Rietveld refinement for S5C (TEOS) with 5 mass% SA-850, fired at 850°C for 8 hrs.

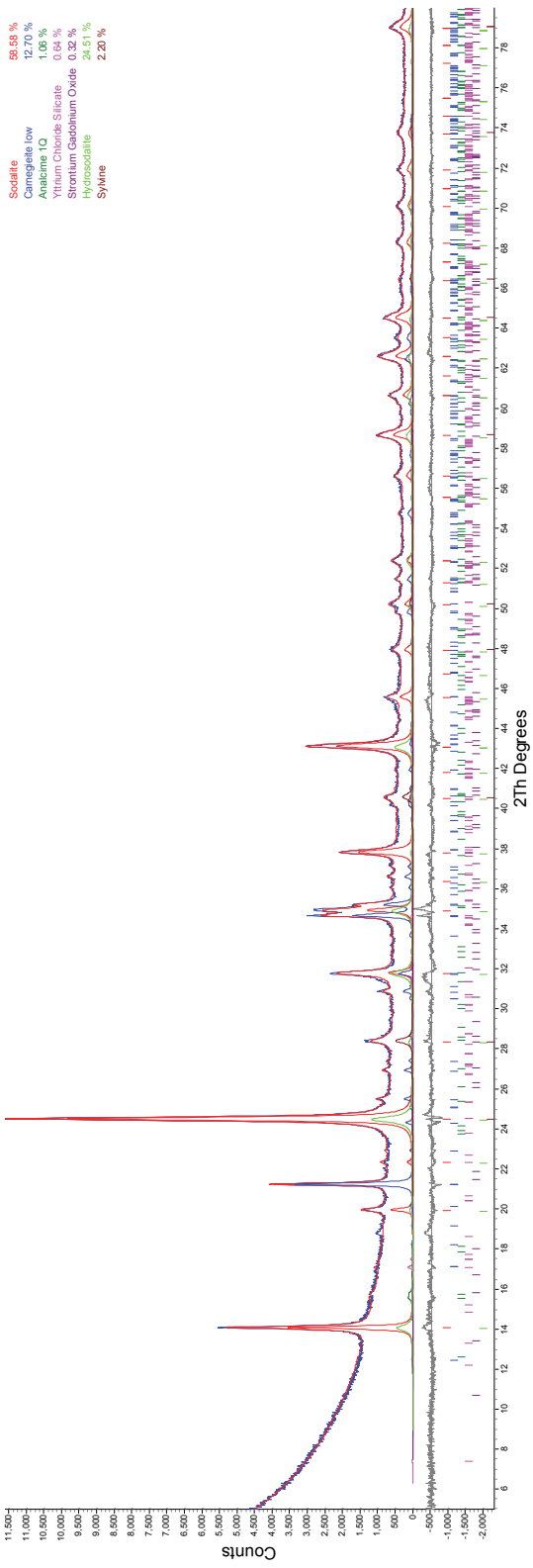

Figure B.39. Rietveld refinement for S5C (TEOS) with 5 mass% NBS-1, fired at 550°C for 8 hrs.

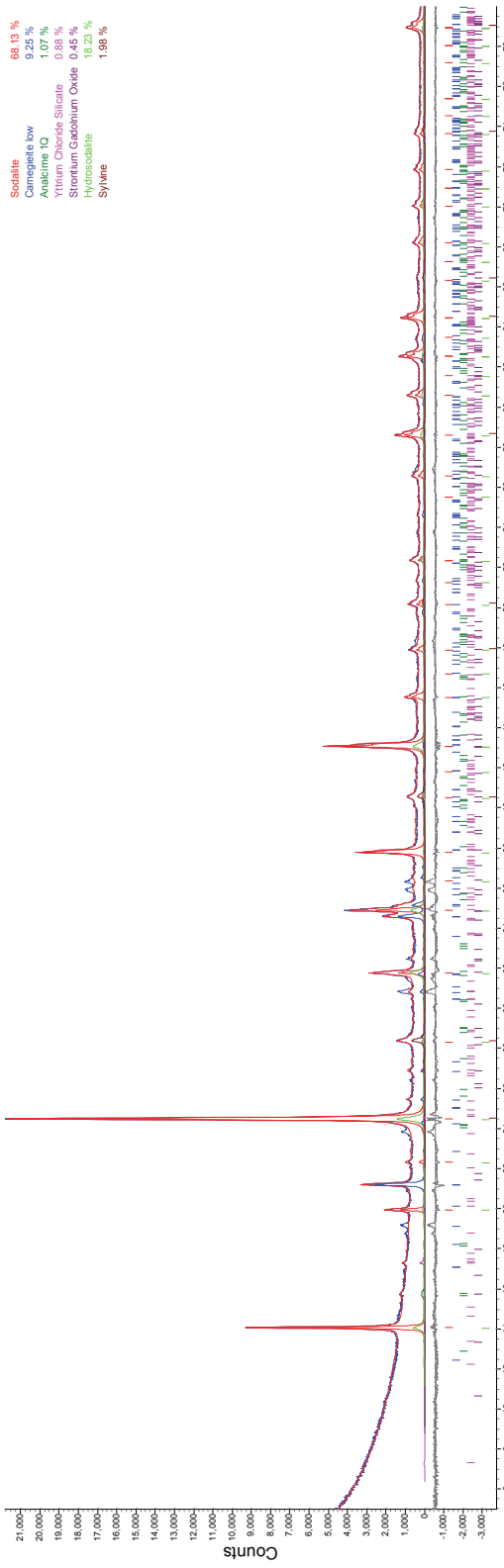

Figure B.40. Rietveld refinement for S5C (TEOS) with 5 mass% NBS-1, fired at 550°C for 8 hrs.

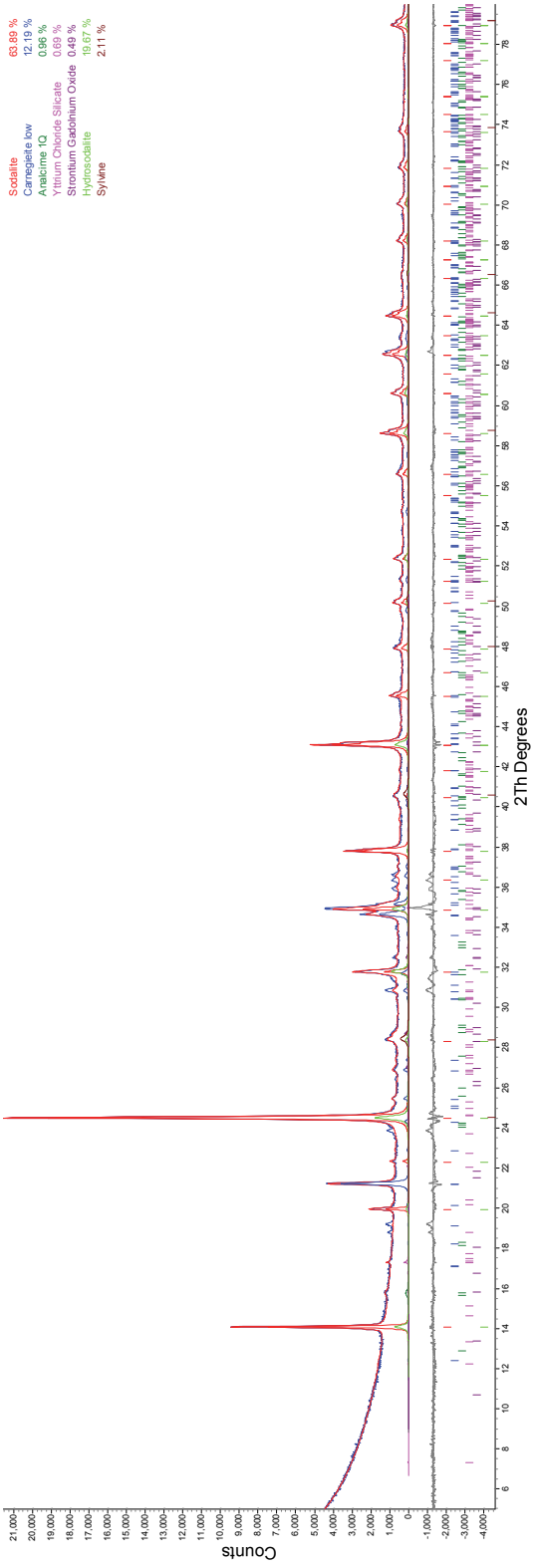

Figure B.41. Rietveld refinement for S5C (TEOS) with 5 mass% NBS-1, fired at 550°C for 8 hrs.

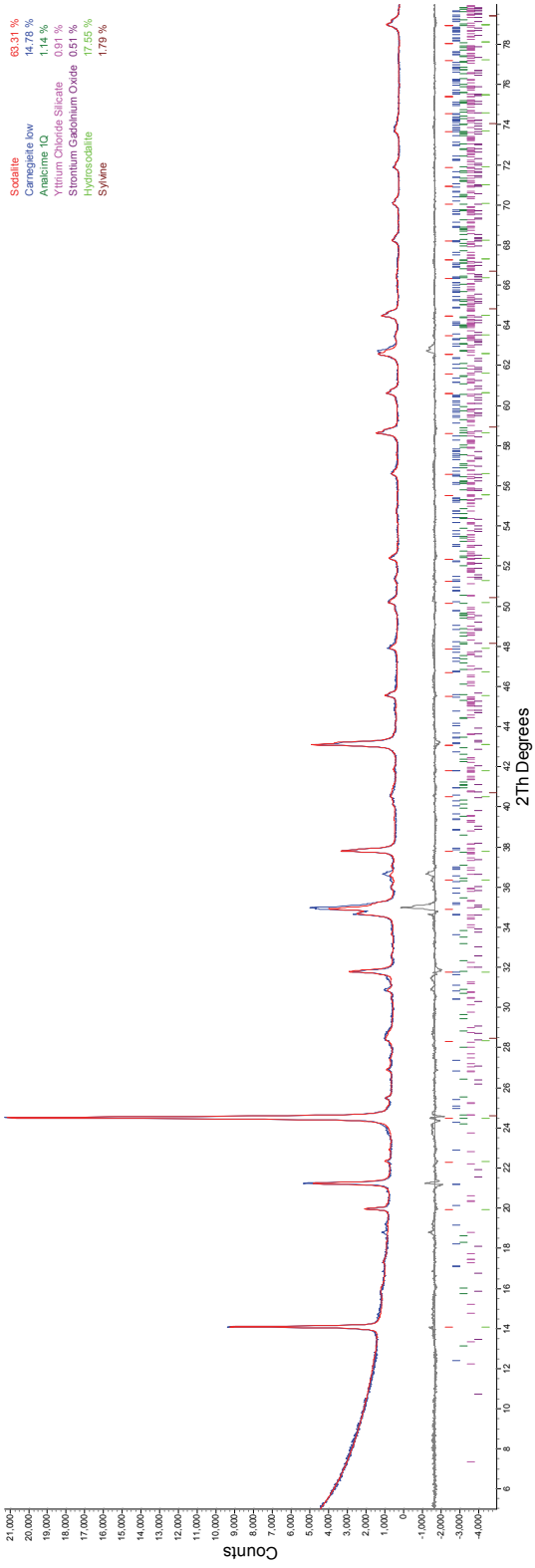

Figure B.42. Rietveld refinement for S5C (TEOS) with 5 mass% NBS-1, fired at 550°C for 8 hrs.

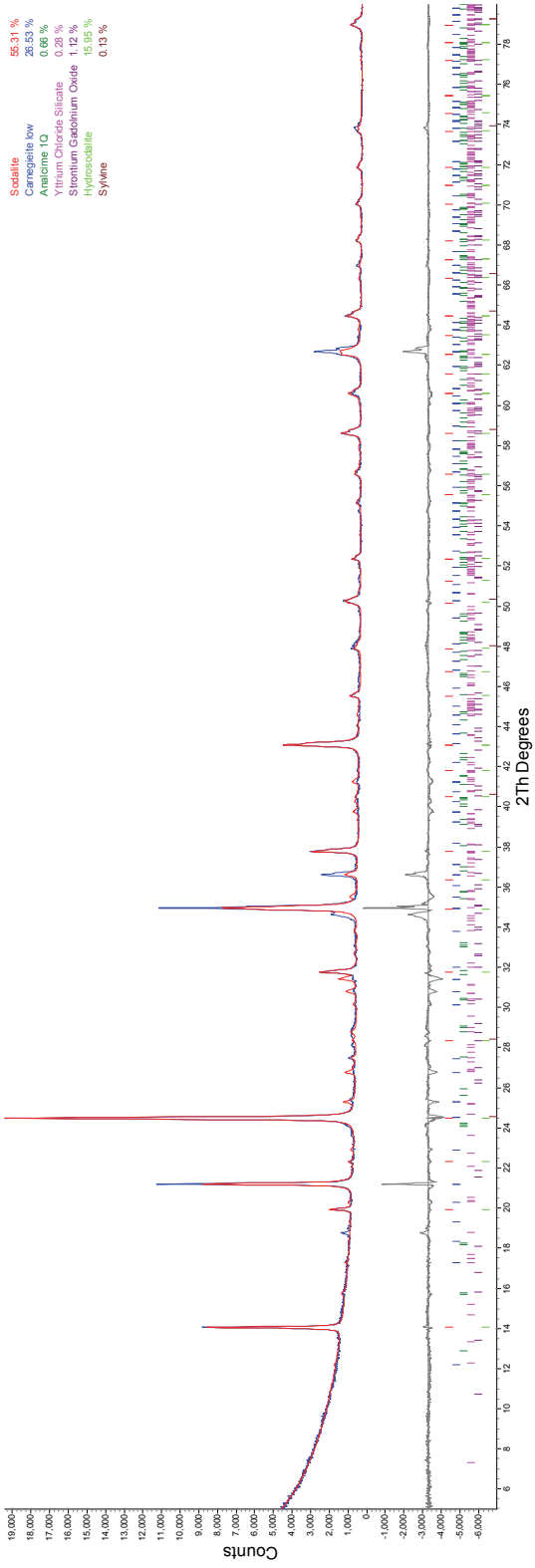

Figure B.43. Rietveld refinement for S5C (TEOS) with 5 mass% NBS-1, fired at 550°C for 8 hrs.

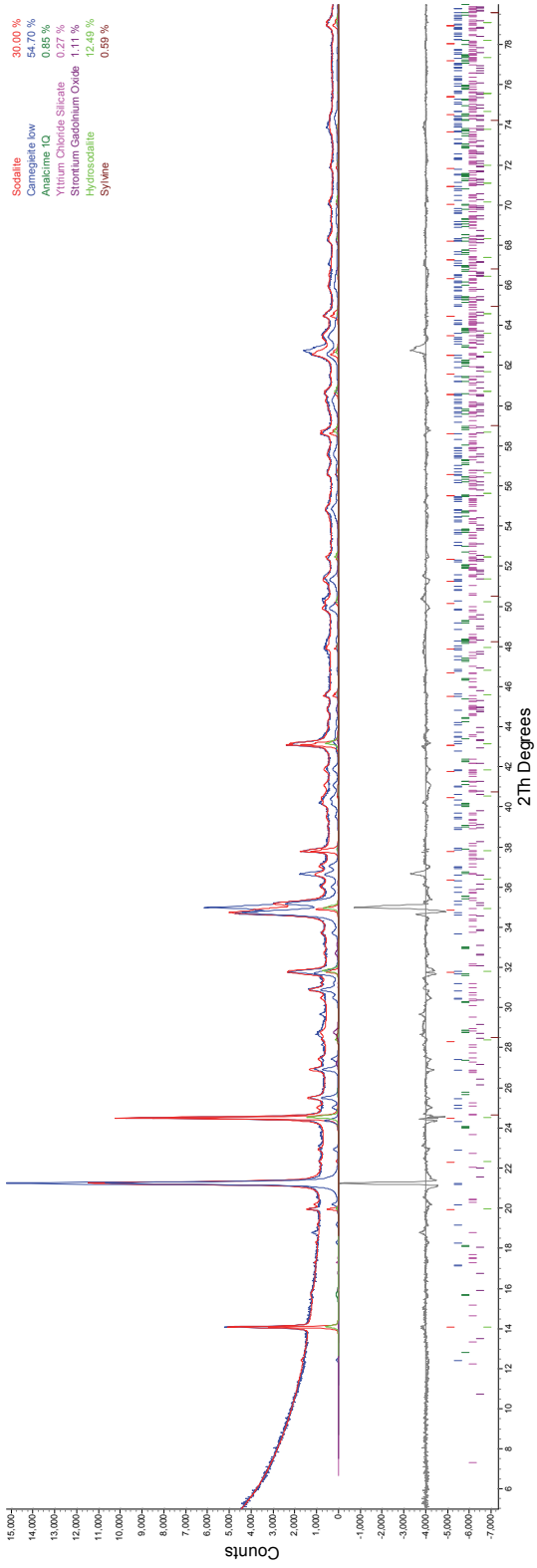

Figure B.44. Rietveld refinement for S5C (TEOS) with 5 mass% NBS-1, fired at 550°C for 8 hrs.

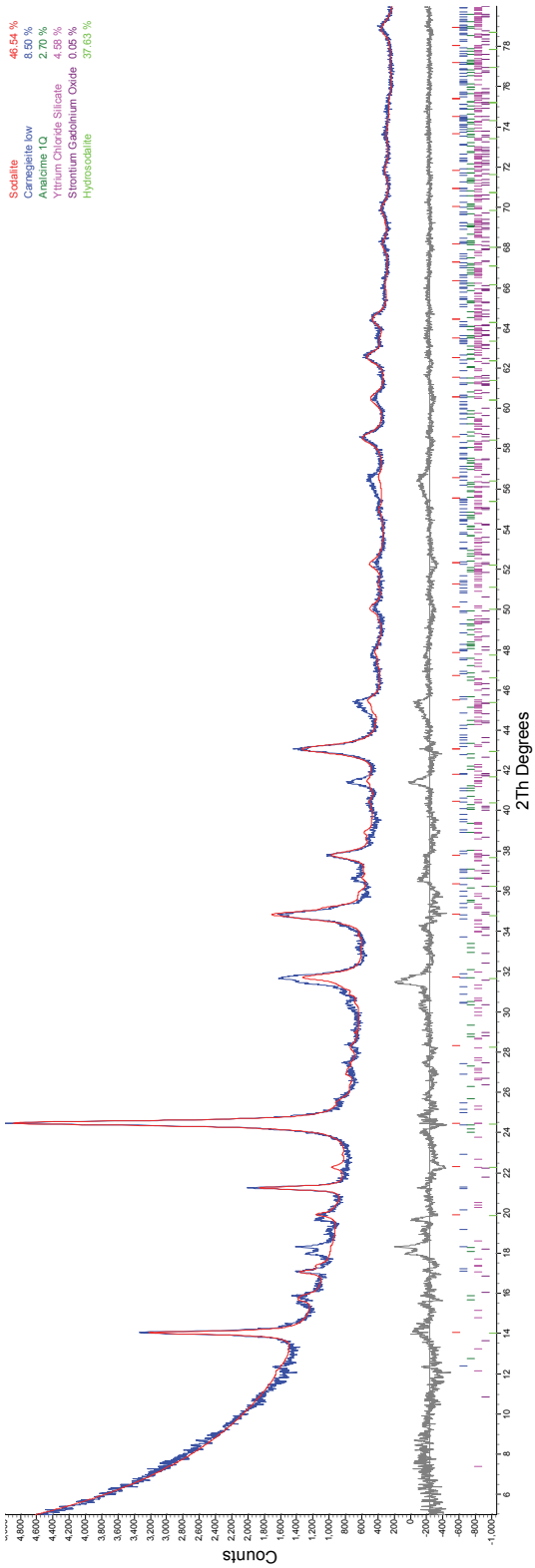

Figure B.45. Rietveld refinement for S5C (TEOS) with 5 mass% TePbO, fired at 550°C for 8 hrs.

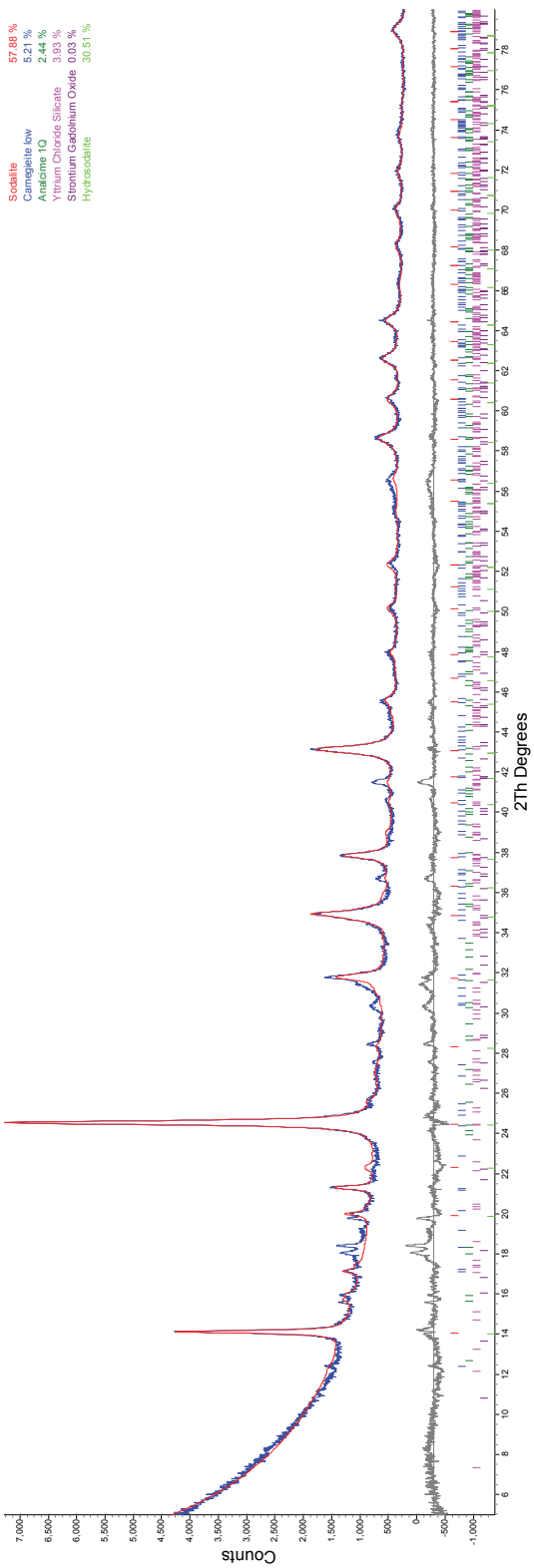

Figure B.46. Rietveld refinement for S5C (TEOS) with 5 mass% TePbO, fired at 600°C for 8 hrs.

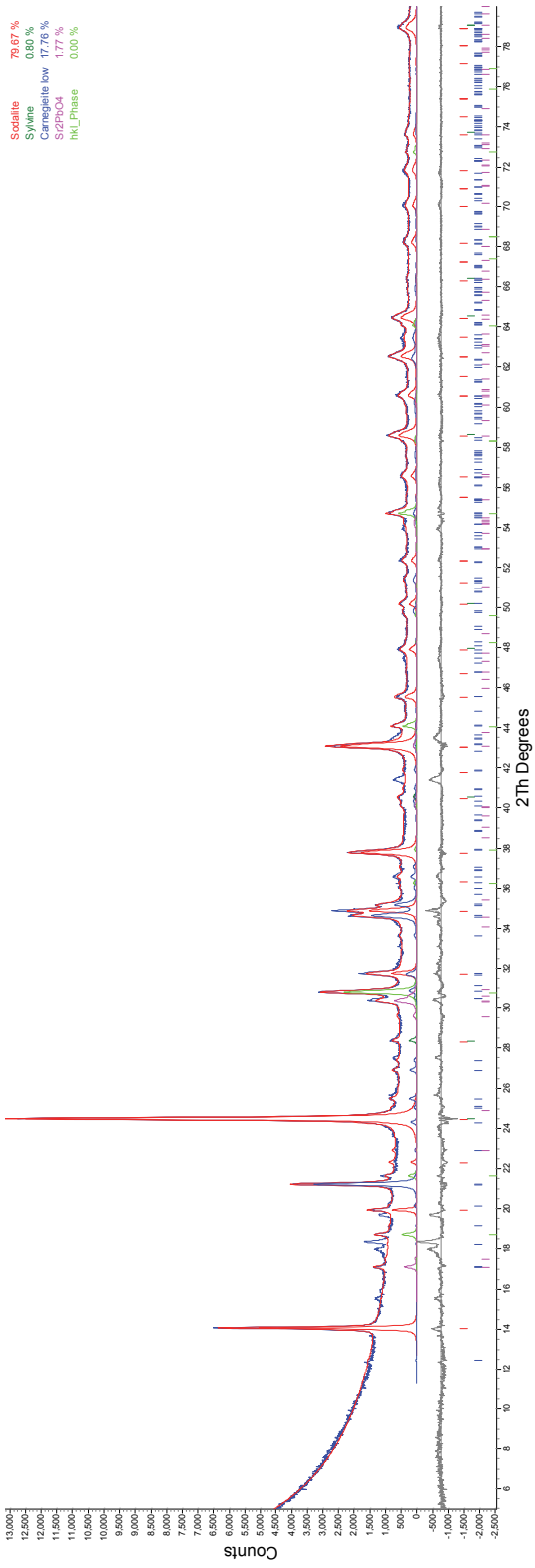

Figure B.47. Rietveld refinement for S5C (TEOS) with 5 mass% TePbO, fired at 750°C for 8 hrs.

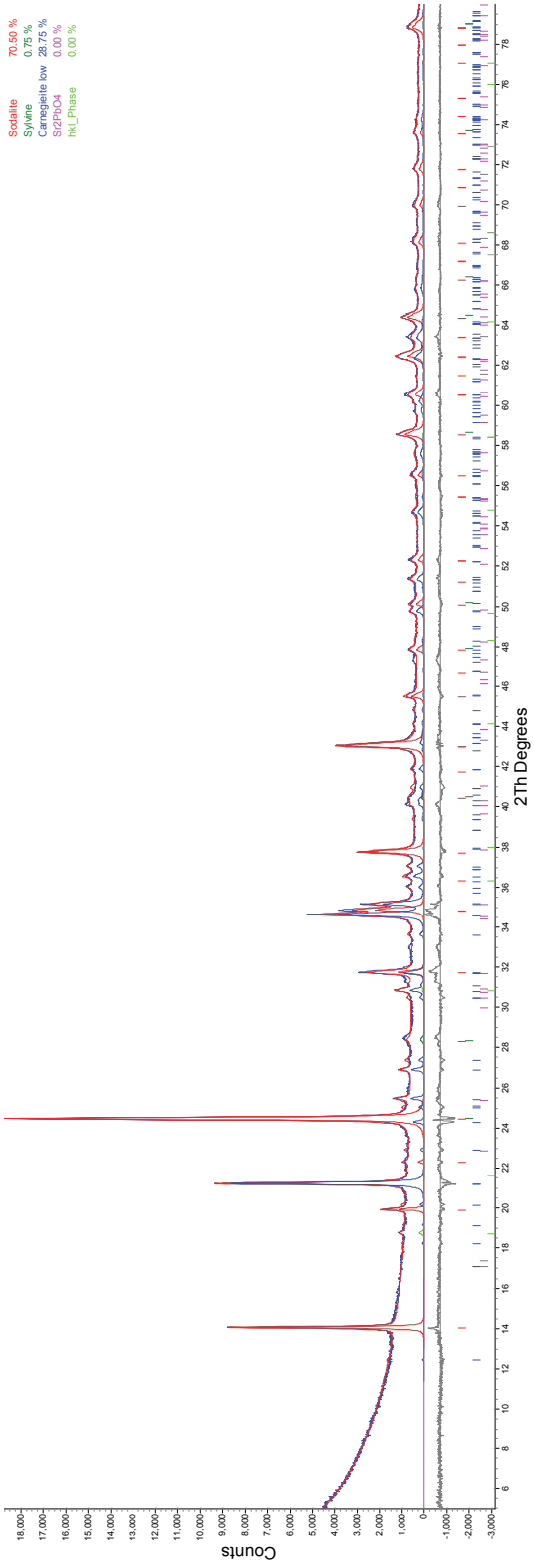

Figure B.48. Rietveld refinement for S5C (TEOS) with 5 mass% TePbO, fired at 850°C for 8 hrs.

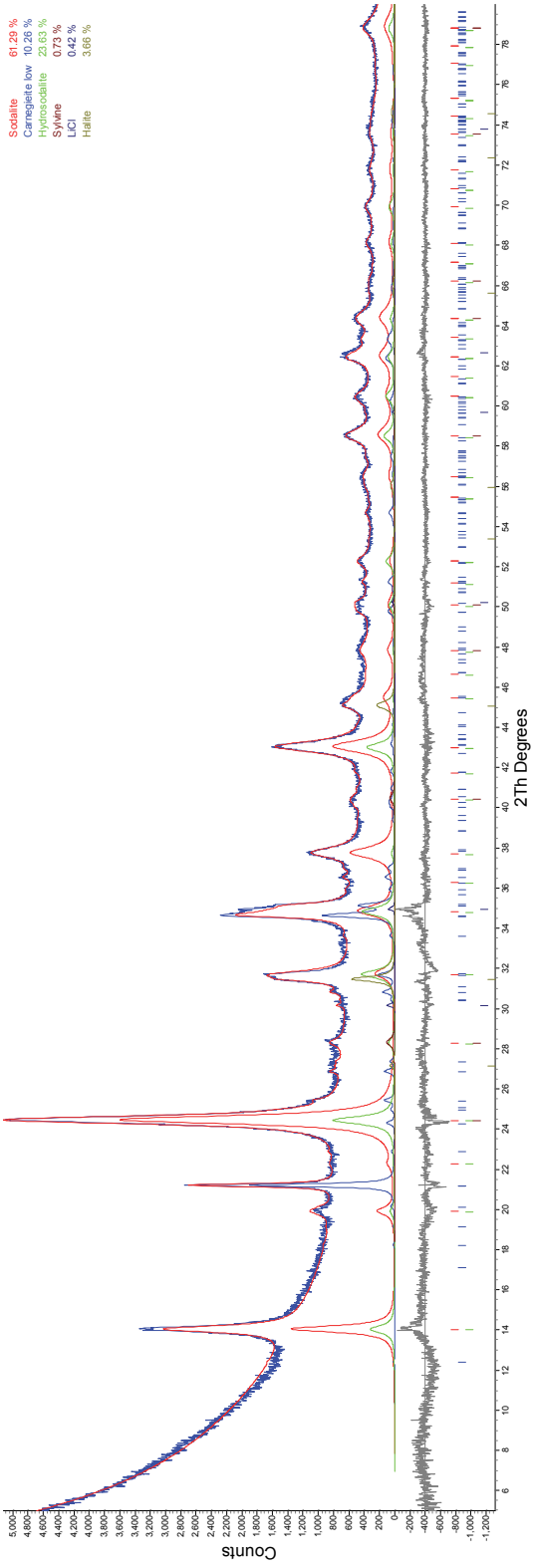

Figure B.49. Rietveld refinement for S5C (TEOS) with 5 mass% NaAlP, fired at 550°C for 8 hrs.

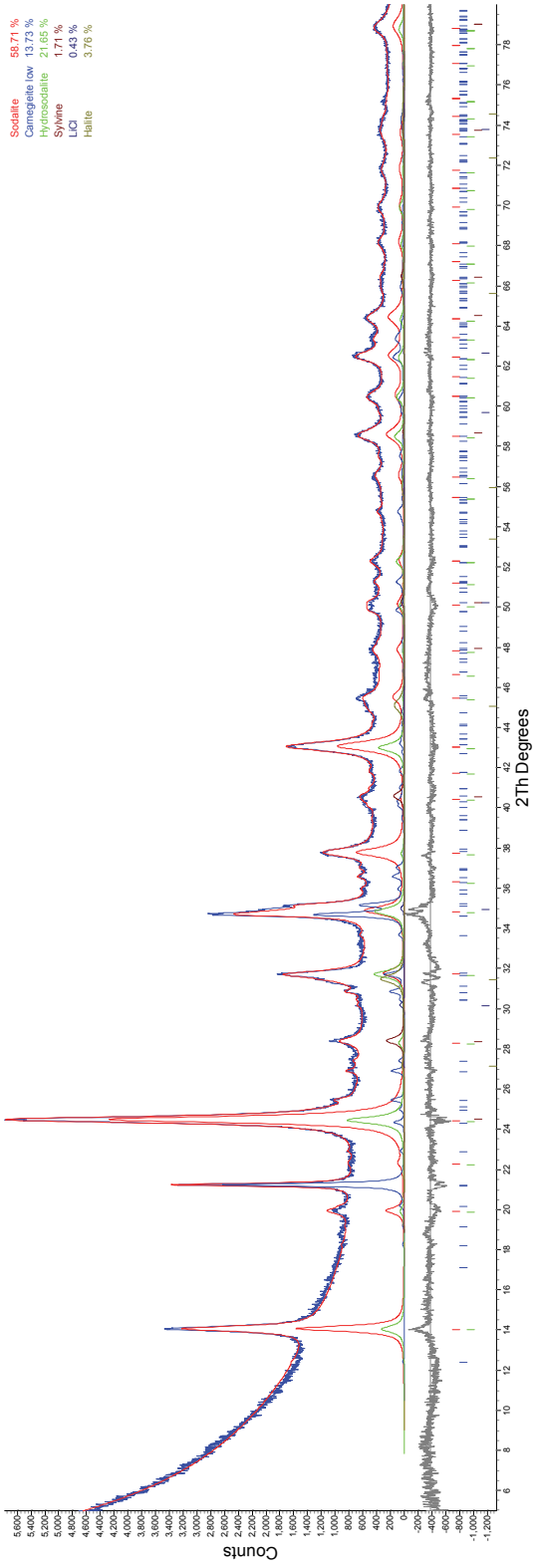

Figure B.50. Rietveld refinement for S5C (TEOS) with 5 mass% NaAlP, fired at 600°C for 8 hrs.

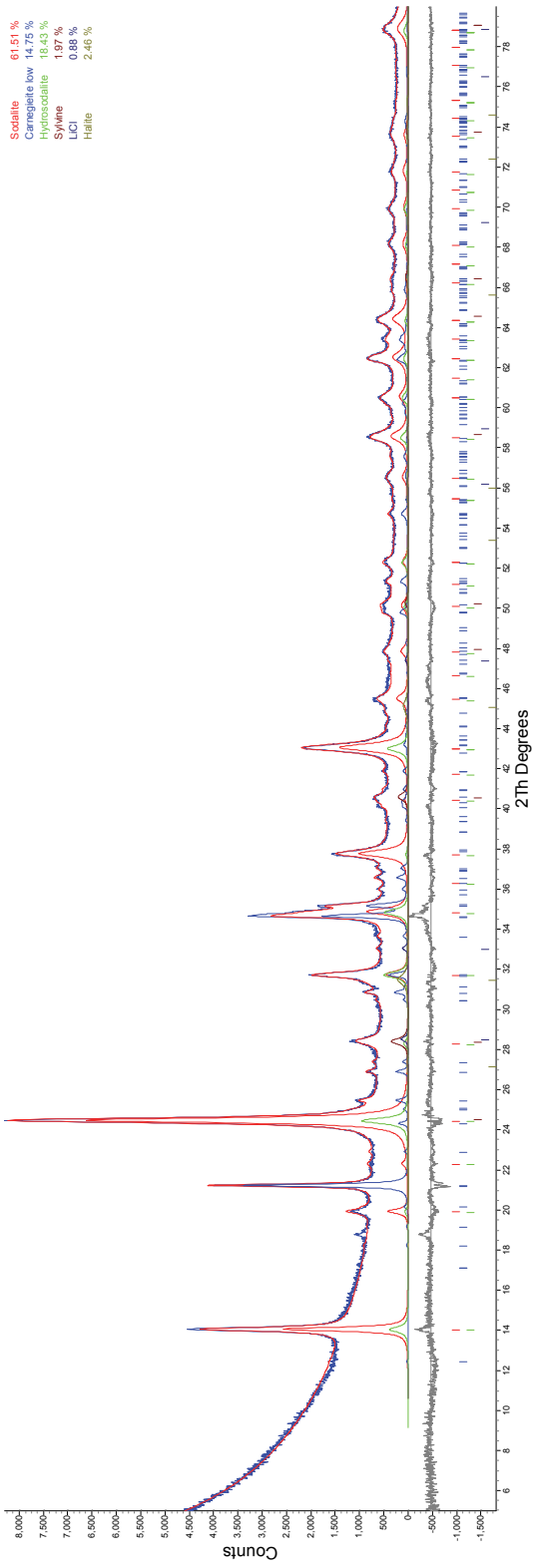

Figure B.51. Rietveld refinement for S5C (TEOS) with 5 mass% NaAlP, fired at 650°C for 8 hrs.

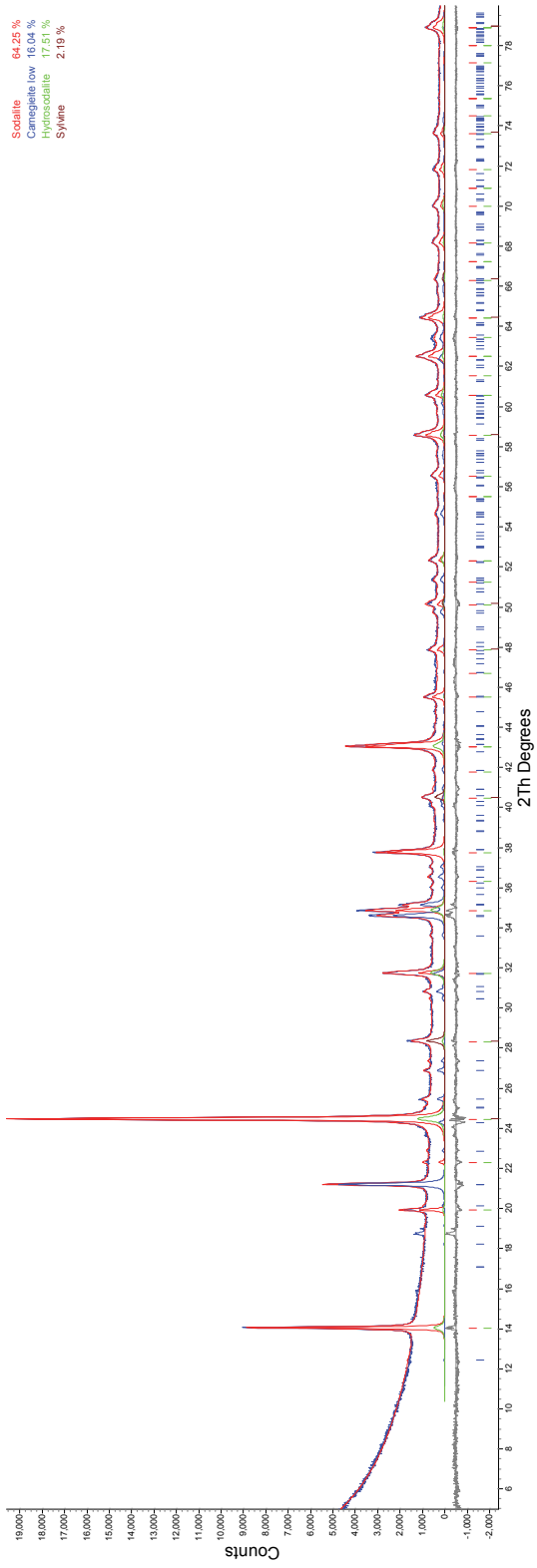

Figure B.52. Rietveld refinement for S5C (TEOS) with 5 mass% NaAlP, fired at 750°C for 8 hrs.

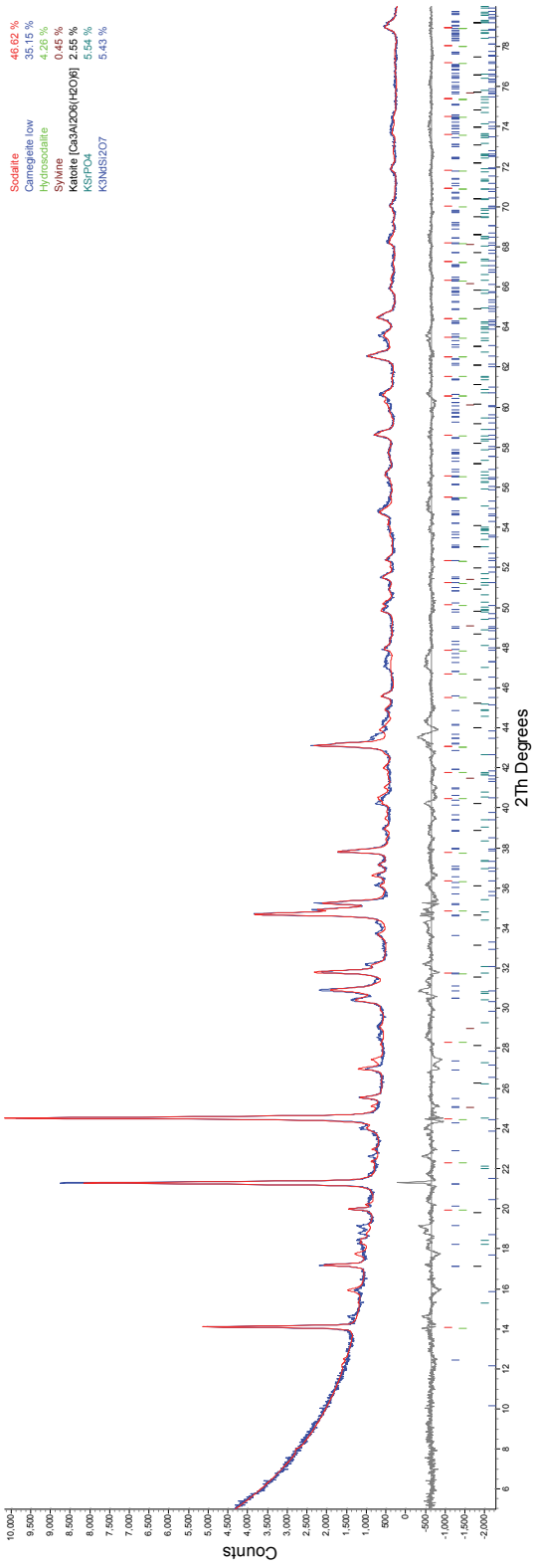

Figure B.53. Rietveld refinement for S5C (TEOS) with 5 mass% NaAlP, fired at 850°C for 8 hrs.

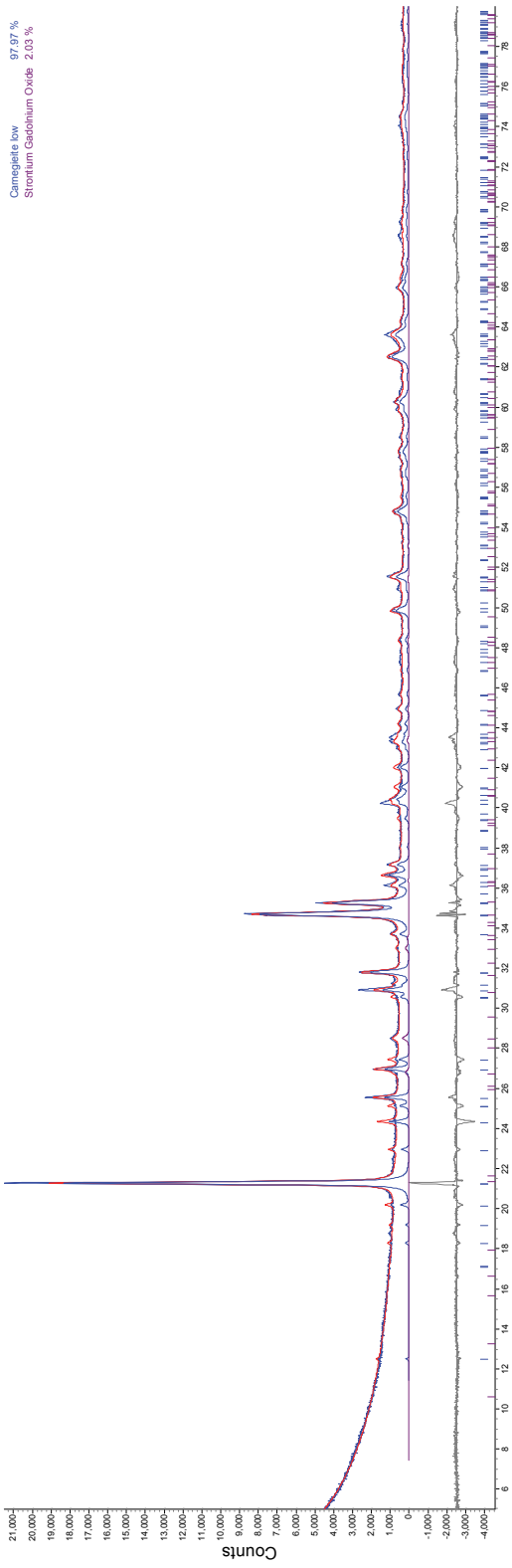

Figure B.54. Rietveld refinement for S5C (TEOS) with 5 mass% NaAlP, fired at 950°C for 8 hrs.

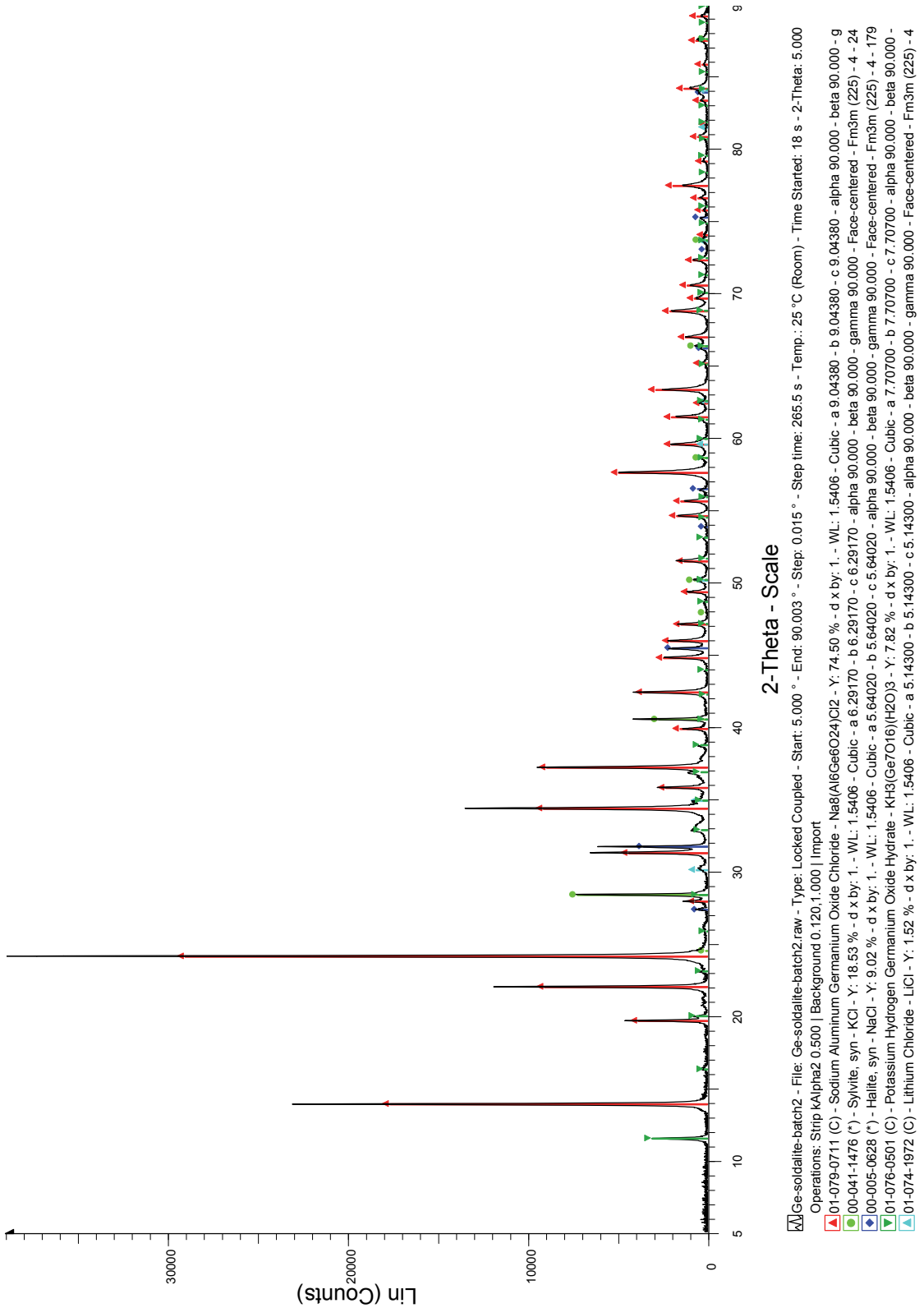

Figure B.55. Peak fitting for S5D (Ge-EtO) batch, unfired.

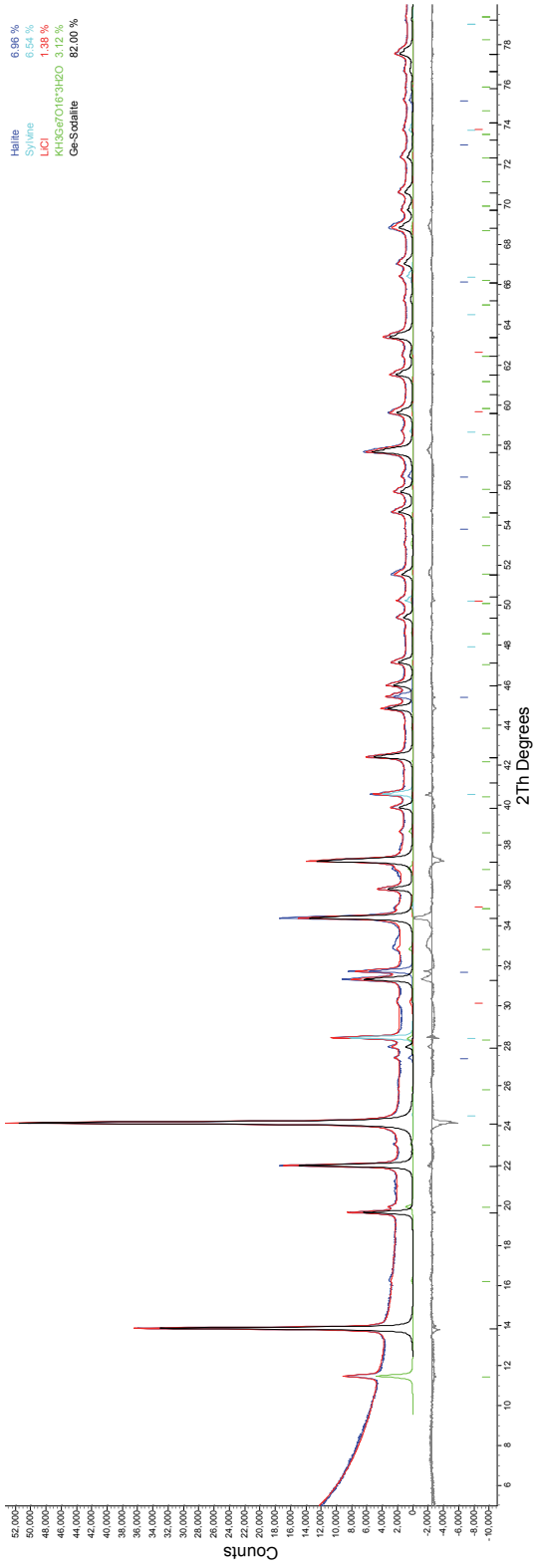

Figure B.56. Rietveld refinement for S5D (Ge-EtO) batch, unfired.